Purdue University
Purdue e-Pubs

Department of Electrical and Computer Engineering Technical Reports

Department of Electrical and Computer Engineering

12-1-1988

Basic Studies of III-V High Efficiency Cell Components

M. S. Lundstrom
Purdue University

M. R. Melloch
Purdue University

R. F. Pierret
Purdue University

M. S. Carpenter
Purdue University

Follow this and additional works at: https://docs.lib.purdue.edu/ecetr

Lundstrom, M. S.; Melloch, M. R.; Pierret, R. F.; and Carpenter, M. S., "Basic Studies of III-V High Efficiency Cell Components" (1988). *Department of Electrical and Computer Engineering Technical Reports.* Paper 634.
https://docs.lib.purdue.edu/ecetr/634

This document has been made available through Purdue e-Pubs, a service of the Purdue University Libraries. Please contact epubs@purdue.edu for additional information.

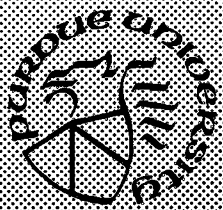

Basic Studies of III-V High Efficiency Cell Components

M.S. Lundstrom, M.R. Melloch, R.F. Pierret, M.S. Carpenter, H. L. Chuang, P.D. DeMoulin, M.E. Klausmeier-Brown, G.B. Lush, D.P. Rancour

TR-EE 88-57
December 1988

School of Electrical Engineering
Purdue University
West Lafayette, Indiana 47907

BASIC STUDIES

of

III-V HIGH EFFICIENCY CELL COMPONENTS

M.S. Lundstrom

M.R. Melloch

R.F. Pierret

H.L. Chuang

P.D. DeMoulin

D.P. Rancour

M.S. Carpenter

M.E. Klausmeier-Brown

School of Electrical Engineering

Technical Report TR-EE 88-57

Purdue University

West Lafayette, Indiana 47907

Annual Progress Report: 8/15/87 - 8/14/88

Subcontract: XL-5-05018-1

NOTICE

This report was prepared as an account of work sponsored by the Solar Energy Research Institute, a Division of Midwest Research Institute, in support of its Contract No. DE-AC02-83-CH10093 with the United States Department of Energy. Neither the Solar Energy Research Institute, the Midwest Research Institute, the United States Government, nor the United States Department of Energy, nor any of their employees, nor any of their contractors, subcontractors, or their employees, makes any warranty, express or implied, or assumes any legal responsibility for the accuracy, completeness or usefulness of any information, apparatus, product, or process disclosed, or represents that its use would not infringe privately owned rights.

PREFACE

The efficiencies of III-V solar cells, especially GaAs-based cells, continue to rise. Because the material quality of such solar cells is now so high, it is time to examine the device design closely in order to ascertain what limits the performance of present, record-efficiency cells. Such work will provide accurate estimates of the realistic efficiency limits of III-V solar cells and will provide a roadmap for reaching ultimate efficiencies.

This project's objective is to improve our understanding of the generation, recombination, and transport of carriers within III-V homo- and heterostructures. The project consists of the fabrication and photovoltaic characterization of the basic building blocks of III-V cells: the pn junction, the pn heterojunction, the isotype (p-p and n-n) heterojunction and graded gap semiconductors. A significant effort is also being directed at analyzing and understanding the performance of high-quality, III-V solar cells fabricated in industrial research laboratories throughout the United States. The project's goal is to use our understanding of the device physics of high-efficiency cell components to maximize cell efficiency. A related goal is the demonstration of new cell structures fabricated by molecular beam epitaxy (MBE). The development of measurement techniques and characterization methodologies is also a project objective. The insight into III-V device physics expected to occur during the course of this work will, we believe, identify paths towards higher efficiency III-V cells.

This report describes our progress during the third year of the project. This year's efforts centered on characterizing heavy doping effects in p^+-GaAs and assessing their impact on GaAs-based solar cells. We have extended last year's work and obtained strong evidence that the high recombination velocities observed at pp^+ barriers is indeed a consequence of bandgap narrowing. We also explored edge effects in GaAs solar cells and diodes and developed a new technique for chemically passivating GaAs surfaces. This work showed that edge effects often dominate the n=2 current component in present-day, heteroface cells. Finally, we characterized a large number of GaAs p/n heteroface cells in order to quantify recombination losses in high-efficiency cells.

Our work has benefitted greatly from interactions with industrial researchers who have generously provided state-of-the art GaAs solar cells to us. Special thanks to Steve Tobin and colleagues at Spire Corporation who provided a whole series of p-n heteroface solar cells for the basic studies which comprise the core of this work. The work described in this report was supported by the Solar Energy Research Institute. Some of the work described in this report benefitted by collaborations. H.L Chuang was supported by the Indiana Corporation for Science and Technology, P.D. DeMoulin by Sandia National Laboratories, and M.E. Klausmeier-Brown by a fellowship from the Eastman Kodak Company.

SUMMARY

Objectives

The objective of the project is to raise the understanding of dark current mechanisms in GaAs-related solar cells to a level comparable to that of silicon cells. Motivation for this work arises from the observation that much of the progress in crystalline silicon cell performance has occurred as a result of a very deep knowledge of the physics controlling the cell's dark current. Based on this knowledge, new cell structures evolved to suppress dominant dark current mechanisms. A comparable level of knowledge of GaAs cell device physics does not yet exist, but will be essential if cell performance near the thermodynamic limit is to be achieved. Moreover, knowledge gained from studies of the AlGaAs/GaAs material system, should help identify the key problems to be addressed in other III-V materials.

Discussion

A broad investigation of minority carrier transport and recombination in GaAs has been initiated. The work includes investigating high-performance cells, in order to characterize performance-limiting factors, and experiments on MBE-grown test structures designed to obtain specific information on various aspects of minority carriers in GaAs. Several of the major thrusts of the projects are briefly described in this section.

Heavy Doping Effects in p^+-GaAs
So-called bandgap narrowing effects have proven to be of fundamental importance to silicon solar cells. In last year's report we described a sequential etch technique to characterize heavy doping effects in p^+ GaAs. During the past year, we have, in collaboration with researchers at Spire Corporation, applied this technique to a variety of solar cells and have mapped out heavy doping effects from $N_A \simeq 10^{17}$ to 10^{19} cm^{-3}. The results show that for the heaviest doping densities, the intrinsic carrier concentration is at least one order of magnitude higher than it is in lightly doped GaAs. Such heavily doped regions often serve as back-surface fields in solar cells, and these results suggest that the interface recombination velocity of such homojunction barriers will be significantly degraded by bandgap narrowing effects. Bandgap narrowing will also increase the dark current associated with the emitter of a p^+/n heteroface solar cell.

A detailed discussion of our basic experimental technique can be found in "Sequential Etch Analysis of Electron Injection in p^+-GaAs," which is one of the publications included in the Appendix. The results of a series of measurements using this technique are described in "Effects of Heavy Impurity Doping on Electron Injection in p^+-n GaAs Diodes," which is also included in the Appendix.

Because of the Moss-Burnstein shift, we expect that bandgap shrinkage will be less significant in n^+-GaAs. Although we have not yet characterized bandgap narrowing in n^+-GaAs, such measurements will be conducted during the coming year.

Properties of Minority Carrier Mirrors for GaAs-Based Solar Cells
In last year's annual report, we described experiments on p–p^+ homojunction back-surface fields. The results showed that such barriers were ineffective in confining minority carrier electrons. The high barrier recombination velocities could be explained by

bandgap narrowing effects, which would lower the barrier height, or by defects located at the junction. An experiment to identify the cause of the high barrier recombination velocity was designed and conducted. A special test diode was fabricated on a film grown by molecular beam epitaxy in our laboratory. The dark I-V characteristics were then monitored as the film was successively etched. The results showed a clear dependence of the barrier recombination velocity on the width of the p^+ barrier, which indicates that the high recombination velocity is due to a bulk effect and not to defects at the interface. By analyzing the results, we deduced the $n_{ie}^2 D_n$ product in the p^+ barrier. The result turned out to be in close agreement with our previous experiments on bandgap narrowing.

Our conclusion is that $p-p^+$ back-surface fields are ineffective minority carrier mirrors because of bandgap narrowing effects. Heterojunction back-surface fields must be used for effective confinement of minority carriers. A detailed description of this experiment is contained in Chapter 2 of this report.

Edge Effects in GaAs Solar Cells

Much of our research has been directed at relating measured current versus voltage characteristics to the material properties of cells. One concern is the influence of recombination of carriers at the exposed perimeter of the cell. Typical cells are quite large - often much larger than $0.5\,\text{cm} \times 0.5\,\text{cm}$, so that perimeter effects might be assumed to be small. We undertook experiments to quantify perimeter effects and found them to be suprisingly important. Two effects were observed. The first was a shunt leakage thought to be associated with conductive oxides at the cell's perimeter. Proper treatment of the edge, such as dipping the cells in hydrochloric acid, often completely removes this shunt leakage. The second effect is on the cell's $n=2$ current component. By examining how the $n=2$ current scales with cell perimeter and with cell area, we established that for 0.5 by 0.5 cm cells, the perimeter completely dominated the $n=2$ current. Even for the much larger 2 by 2 cm and 4 by 4 cm cells, the perimeter can have a surprisingly large effect. This fact is a simple consequence of the extremely high bulk lifetimes being obtained in present-day cells and the high surface recombination velocity associated with bare GaAs surfaces.

The $n=2$ current component can lower the one-sun fill factor of GaAs cells, so careful treatment of the perimeter is essential. Under concentration, however, only the $n=1$ current, which scales with cell area and not with perimeter, is important. Perhaps the most important implications of this work are for the diagnostic evaluations of cells, which frequently employ the $n=2$ current. For example, we have found it to be extremely difficult to correlate deep level transient spectroscopy (DLTS) measurements to the $n=2$ current. The probable reason is that DLTS probes bulk defects, but the $n=2$ current is sensitive to surface defects.

Several experiments which indicated the importance of the perimeter are described in Chapter 3 of this report. The publication, "Influence of Perimeter Recombination on High-Efficiency GaAs p/n Heteroface Solar Cells," describes a series of experiments which clearly establish the importance of the perimeter in present-day, high-efficiency, GaAs solar cells.

Chemical Passivation of GaAs Surfaces

According to recent reports, the treatment of GaAs surfaces with Na_2S is effective in lowering the surface state density. Such treatments could be useful for GaAs-related solar cells; the $n=2$ current associated with perimeter recombination might be eliminated, and the need for AlGaAs window layers might be removed. We have examined

this chemical treatment and found that it lowered the n=2 edge current by a factor of three. Unfortunately, a sizeable shunt leakage was also introduced. We also found that $(NH_4)_2S$ lowers the n=2 edge current by a factor of three, but it has the advantage of introducing virtually no shunt leakage.

If these treatments prove effective and robust, they could be very important for solar cells. Our initial experiments on applying the treatments to solar cells are described in "Effects of Na_2S and $(NH_4)_2S$ Edge Passivation Treatments on the Dark Current-Voltage Characteristics of GaAs pn Diodes," which is contained in the Appendix. Very recent work, including XPS analysis which indicates the virtual absence of oxygen on a treated surface, is the subject of Chapter 4.

Conclusions

The basic studies our group is now engaged in are directed at providing information and understanding essential for attaining cell efficiencies near the thermodynamic limit. The work is motivated by three questions: 1) what are the values of the key physical parameters which control cell performance? 2) what are the dominant recombination loss mechanisms in present-day, high-performance cells? and 3) how should cells be designed to minimize recombination losses? These basic studies, complemented by the sophisticated numerical device simulation capability at Purdue, should provide a road-map for maximizing cell performance. Although the work is specifically directed at GaAs-based solar cells, the methodology being developed for diagnosing cell performance and for the design of new cells should be broadly applicable.

During the past year we advanced our understanding of GaAs-based cells in a number of ways. First, we completed the first study of bandgap narrowing effects in p-type GaAs and showed that such effects have important implications for GaAs-based solar cells. Secondly, we provided a clear understanding of $p-p^+$ GaAs homojunction barriers, demonstrated their ineffectiveness, and explained the result as a consequence of bandgap narrowing. Thirdly, we clearly established the important influence of the mesa perimeter on solar cell performance. And finally, we developed a new chemical treatment for passivating GaAs surfaces and demonstrated one application to solar cells. The various chapters in this report and the reprints in the report's appendix describe the year's activities in detail.

TABLE OF CONTENTS

CHAPTER 1: DEVICE PHYSICS OF CRYSTALLINE SOLAR CELLS 1

CHAPTER 2: EFFECTS OF BANDGAP NARROWING ON PP^+ GaAs BACK-SURFACE-FIELDS 31

CHAPTER 3: EDGE EFFECTS IN MBE-GROWN GaAs DIODES 42

CHAPTER 4: CHEMICAL PASSIVATION OF GaAs SURFACES 58

APPENDIX: PUBLICATIONS 68

CHAPTER 1

DEVICE PHYSICS OF CRYSTALLINE SOLAR CELLS

Preface

This chapter is a written version of a talk presented at the 8th Photovoltaic Advanced Research and Development Project Review Meeting in Denver Colorado on November 16-18, 1987. A shorter version of this paper was published in *Solar Cells* (Vol. 24, pp. 91-102, 1988). This chapter was included because it summarizes the important material and device design issues that confront cell designers and because it includes much that was presented orally but which did not find its way into publication.

1.1. INTRODUCTION

Record high conversion efficiencies are now being reported for both crystalline silicon and gallium arsenide solar cells. High material quality was a prerequisite for achieving these high efficiencies, but cell design was also a crucial factor. The design of a solar cell is based on the properties of the semiconductor, the constraints imposed by the technology, and on an understanding of the cell's internal device physics. The purpose of this paper is to discuss, compare, and contrast the device physics of silicon and gallium arsenide cells. The paper does not attempt a comprehensive review of Si and GaAs cells; its emphasis is on the device physics issues that confront the cell designer. A review of how such high efficiencies were achieved in two quite different semiconductors demonstrates that there is no single, best solar cell design but, rather, that solar cell designs evolve as dominant recombination losses are identified. The paper will also illustrate how physical device simulation is used to identify loss mechanisms and to guide device design.

1.2. CELL DESIGN FUNDAMENTALS

We begin with a brief review of the basic concepts underlying the design of high-efficiency cells. The simple expression,

$$\eta = \frac{J_{SC} V_{OC}\, FF}{P_{inc}/A}, \tag{1.1}$$

shows that high efficiency results by maximizing short-circuit current and open-circuit voltage while maintaining a high fill factor. The selection of a semiconductor is a compromise; to maximize short-circuit current, a small bandgap should be selected, but for high open-circuit voltage, a large bandgap is needed. Figure 1.1 shows a plot of the thermodynamic limit conversion efficiency versus bandgap for one-sun and 500-sun operation [1]. The bandgaps of silicon and GaAs are seen to be nearly optimum. Both semiconductors show a conversion efficiency above 30% at one-sun and above 35% at 500 suns.

The object of cell design is to approach the cell's thermodynamic limit by maximizing the number of optically-generated carriers while minimizing recombination losses. To achieve high efficiencies, 98% of the available photons should be absorbed. Figure 1.2 shows that for GaAs, about 4 μm of semiconductor is adequate, but for silicon, 1500 μm are required. For such thick silicon cells, the electrical performance would be degraded by recombination losses. Much of the recent improvement in silicon performance is due

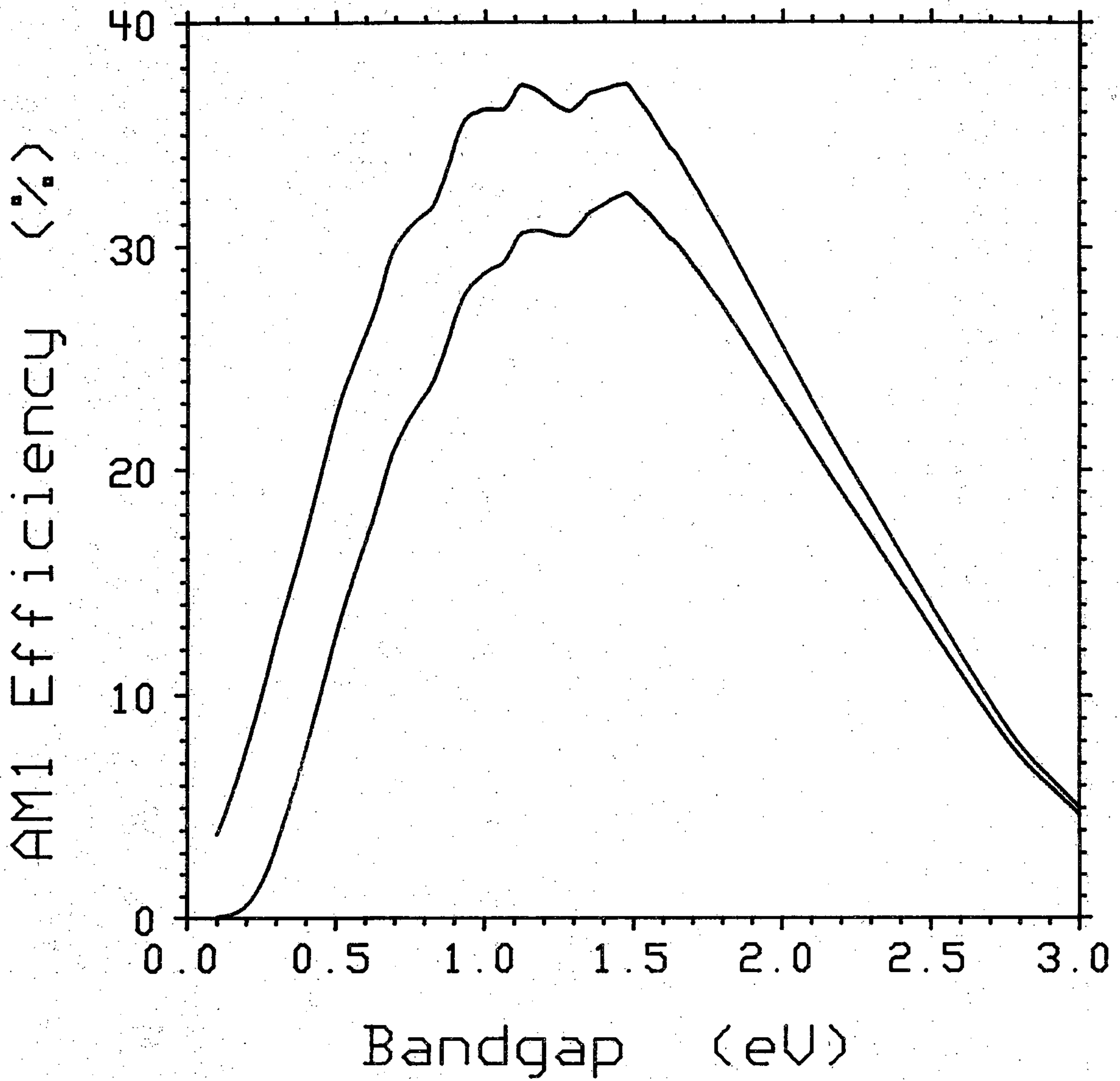

Fig. 1.1 Thermodynamic limit conversion efficiency versus semiconductor bandgap [1]. Curve "a" is for 1-sun operation and curve "b" for 500 suns. An AM1, direct normal solar spectrum is assumed.

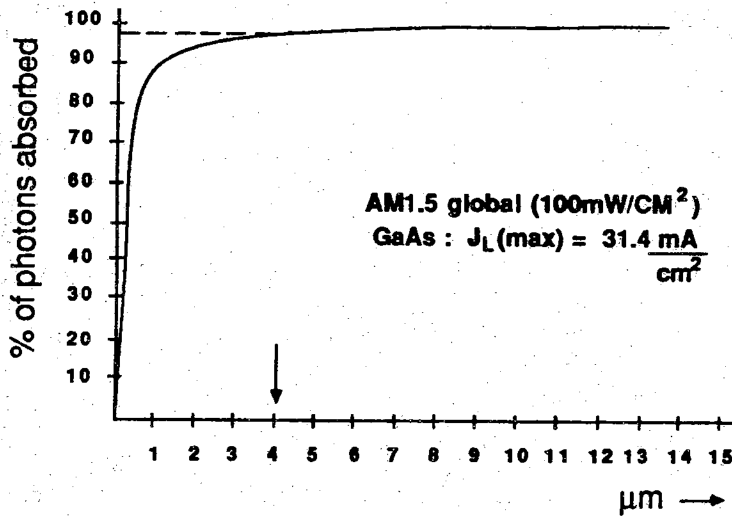

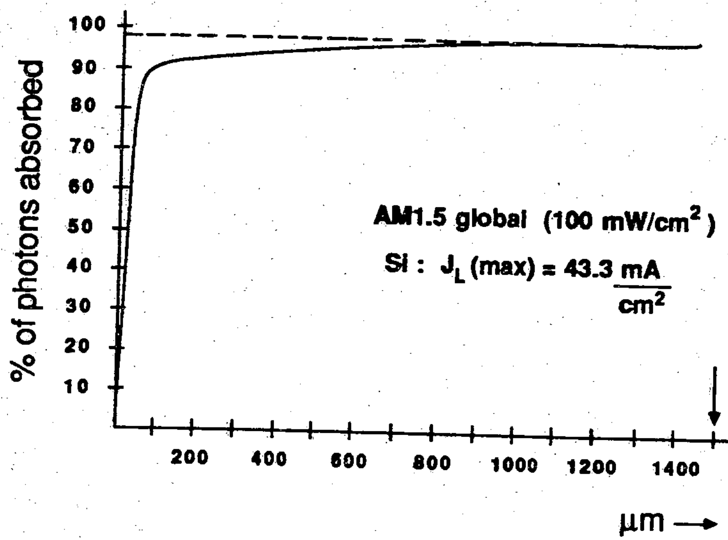

Fig. 1.2 Percent of available photons absorbed versus semiconductor thickness. Curve "a" is for GaAs, curve "b" for silicon. An AM1.5 global spectrum normalized to 100 mW/cm^2 was assumed [21].

to the use of light-trapping techniques which makes the cell appear optically thick yet electrically thin. There has also been much progress in sophisticated anti-reflection coatings, texturizing, and grid design which have resulted in reflection plus shadowing losses below 3%.

The superposition principle,

$$J = J_{SC} - J_{DARK}(V) , \tag{1.2}$$

states that maximizing V_{OC} is equivalent to minimizing the cell's dark current. The dark current is just the total rate at which carriers recombine within the cell,

$$J_{DARK} = \frac{q}{A} \int \int \int R(x,y,z)\, dxdydz , \tag{1.3}$$

where the integration is over the volume of the cell. A "bucket" analogy which illustrates the design process for maximizing V_{OC} is shown in Figure 1.3. The height of the "fluid" represents the excess carrier density, which should be maximized to achieve high V_{OC}. The holes in the bucket represent the various recombination losses. Cell performance increases as the various recombination processes are identified and suppressed. Some processes, such as Shockley-Read-Hall recombination, are directly related to the material quality but others, such as recombination at the metal contacts, can be influenced by the designer. Note that the relative importance of various recombination processes can vary widely with cell design. As dominant recombination processes are suppressed, the fluid level rises and new processes can become important or even dominant.

Successful cell design consists of identifying, quantifying, then suppressing the important recombination mechanisms. The designer needs the ability to examine the cell's internal recombination rate. Unfortunately, electrical measurements tend to reflect the integrated recombination rate and cannot, therefore, identify the importance of specific internal mechanisms. Experiments to isolate and quantify various mechanisms can be performed, but they are difficult and time-consuming. An alternative approach which involves the use of a detailed, physical device model is discussed next.

1.3. PHYSICAL DEVICE SIMULATION

The performance of a cell is described by Poisson's equation and by the electron and hole continuity equations,

$$\nabla \cdot \vec{D} = q\left[p(\vec{r}) - n(\vec{r}) + N_D^{+}(\vec{r}) - N_A^{-}(\vec{r}) + N_T(\vec{r}) \right], \tag{1.4a}$$

$$\nabla \cdot \vec{J_n} = -q\left[G_{op}(\vec{r}) - R(\vec{r}) \right], \tag{1.4b}$$

and

$$\nabla \cdot \vec{J_p} = +q\left[G_{op}(\vec{r}) - R(\vec{r}) \right]. \tag{1.4c}$$

The consititutive relations for the flux and current densities [2],

$$\vec{D} = -\kappa_S(\vec{r})\, \epsilon_0 \nabla \cdot V(\vec{r}) , \tag{1.5a}$$

$$J_n = -nq\mu_n \nabla \cdot [V(\vec{r}) + V_n(\vec{r})] + kT\mu_n \nabla \cdot n(\vec{r}) , \tag{1.5b}$$

and

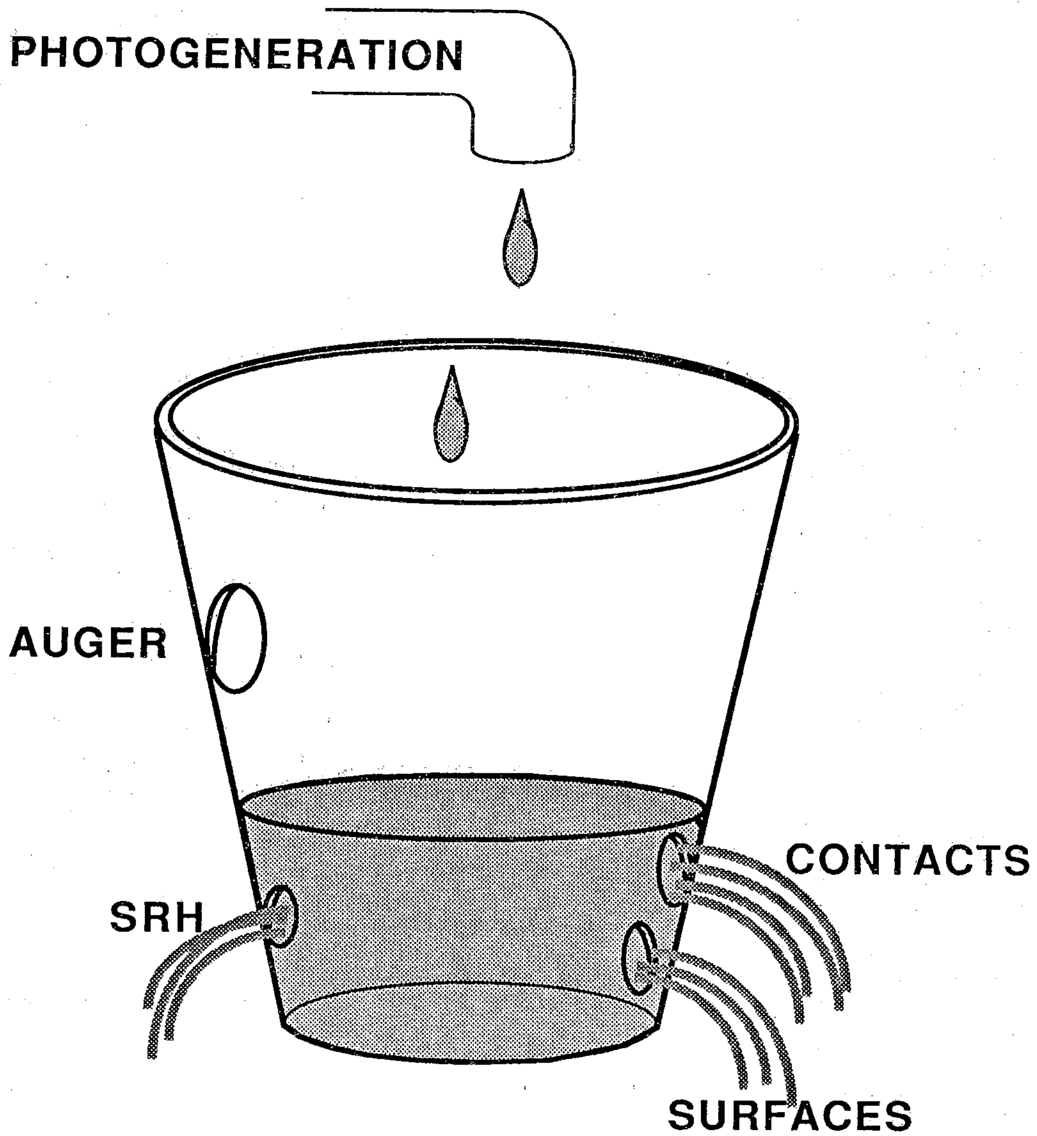

Fig. 1.3 Bucket analogy illustrating how recombination losses influence V_{OC}.

$$J_p = -pq\mu_p \nabla \cdot [V(\vec{r}) - V_p(\vec{r})] - kT\mu_p \nabla \cdot p(\vec{r}) \,, \tag{1.5c}$$

relate the fluxes to the underlying variables, the electrostatic potential, $V(\vec{r})$, and the electron and hole densities, $n(\vec{r})$, and $p(\vec{r})$. The additional terms, V_n, and V_p, in the drift-diffusion equations account for spatial variations in material composition [2]. The carrier recombination rate is the sum of Shockley-Read-Hall, band-to-band Auger, and band-to-band radiative recombination,

$$R(\vec{r}) = \frac{np - n_i^2(\vec{r})}{\tau_n(p + p_1) + \tau_p(n + n_1)} + (A_n n + A_p p + B)[np - n_i^2(\vec{r})] \,. \tag{1.6}$$

These equations, along with boundary conditions for the cell's surfaces and contacts, completely specify the operation of the cell. When the constitutive relations are inserted, (1.4a)-(1.4b) comprise three coupled nonlinear equations in three unknowns, $V(\vec{r})$, $n(\vec{r})$, and $p(\vec{r})$. Under well-known simplifying assumptions (e.g. simple doping profiles, complete ionization of dopants, low-level injection, etc.) the governing equations can be simplified and closed-form solutions obtained, but cells often operate under conditions that invalidate many simplifying assumptions. Moreover, the continued quest for higher efficiencies demands ever more accurate and detailed modeling of the device.

Physical device simulation consists of solving the governing equations, (1.4a)-(1.4c), directly by using a digital computer. The only approximations involved are numerical (e.g. derivatives are approximated by finite differences). The accuracy of the model is limited not by the ability to solve the governing equations, but by knowledge of the physics and the values of various materials parameters. Since the solution is obtained at each point within the device, not simply at its terminals, the internal operation of the device can be probed at will. For crystalline silicon cells, computer codes that solve the governing equations in one and two dimensions are now widely-available. Confidence in the predictive ability of these codes was established by comparing simulations with experiments. The successes and failures of these comparisons deepened the understanding of silicon cell device physics and focussed experimental work on topics of most concern to device design. After a decade of such work, confidence in the codes is high; they now serve as reliable guides for cell design. For GaAs and "newer" materials, confidence in the physical models is not yet as high, but trends can be modeled and the merits of various designs gauged. These models are improving as our knowledge of device physics and parameter values improves.

Figures 1.4a-d illustrate the capabilities of physical device simulation. Figure 1.4a shows the input deck for a SCAP2D [3] simulation of a conventional p on n silicon concentrator cell. The deck consists of English-like statements which specify the cell structure, material parameters, and the type of analysis desired. Figure 1.4b shows the results of the solar cell simulation. While the simulated terminal characteristics agree well with experiment, they give the designer no more information than did the experiment itself. Figure 1.4c shows a plot of the internal recombination rate at open-circuit voltage versus position within the cell. With such a plot, the designer can inspect the internal device physics of the cell at a level that is impossible experimentally. The recombination information is summarized in Fig. 1.4d which clearly identifies the dominant loss mechanisms.

1.4. DEVICE PHYSICS OF SILICON CELLS

In this section, we make use of computer simulation to examine and compare the internal device physics of three different concentrator cells. The first cell considered is similar to the Sandia, p on n cell developed in the early 1980's [4]. After identifying the

```
*TITLE   P ON N SILICON CONCENTRATOR CELL
DEFPRO  TEMP=24 DOPBLK=2.0E16 NXF=36 NYF=55
+       IGEOM=CON TAPE=NO SOLAR=YES
+       YMAX=305.0 XMAX=150.0 NUM2Q=-1 DELTST=1.0E-6

BGN     BGNMOD=SB NCRITPSB=1.0E17 NCRITNSB=1.0E17

TOPBND  XT=150.0 TOP=YES
+       DXT=150.0 PTOP=1
+       XJTOP=1.0
+       DTOP=5.0E19 QSSTOP=1.0E9

BOTBND  X3=14.0 XB=150.0 BOT=YES BOT=NO
+       DXB=150.0 PBOT=1
+       XJBOT=0.4

+       DBOT=-01.5E20 QSSBOT=1.0E9

LEFBND  QSSLEF=0 LEF=NO

RITBND  QSSRIT=0 RIT=NO

XMESH   NX=1 XX=0.01 NX=8 XX=150.0 NX=7 XX=20.0
+       NX=7 XX=150.0

YMESH   NY=1 YY=0.01 NY=1 YY=0.03 NY=1 YY=0.1 NY=1 YY=0.3
+       NY=1 YY=0.5 NY=5 YY=3.0 NY=2 YY=5.0
+       NY=7 YY=302.0 NY=4 YY=303.5
+       NY=5 YY=305.0

PROBLM  TAPE=NO INFO=5 IVGSS=0 NUM2D=3

NEWTON  DELTST=0.0001 NDAMP=1 ITMAX=40 IDVRG=5

RECOMB  TAUP=1000.E-6 TAUN=1000.E-6 NC=7.1E15
+       AP=0.99E-31 AN=2.8E-31

GENRAT  IGEN=AM1P5 CONCEN=180.0 REFL=0.0
+       BSR=0.99

MOBLTY  MODEL=CT-CCS

BC  SPTOP=10.0 SNTOP=10.0 SPBOT=10.0 SNBOT=10.0
+   QSSTOP=1.0E9 QSSBOT=1.0E9 IDEAL=YES

TABLES  XLINE=0.0 XLINE=22.5 VEES=0.0

SC  VSTART=0.0 COMPV=YES
```

Fig. 1.4a Input deck for a SCAP2D simulation [3] of a conventional p on n silicon concentrator cell.

RUN: 3 DATE: 10/01/87 TIME: 23.36.03
AM1P5 GENERATION AT 180.00 SUNS
9.4 PERCENT SHADOWING
0.0 PERCENT REFLECTANCE
INCIDENT POWER = 14.97262 WATTS/CM2
E-H/PHOTON = 0.60805
99. PERCENT EFFICIENT BACK SURFACE REFLECTOR

TEMPERATURE: 24.00 DEG C

*** CELL PARAMETERS:
VOC =0.757332 VOLTS
JSC =0.552175E+01 AMPS/CM^2
VMP =0.626614 VOLTS
JMP =0.525693E+01 AMPS/CM^2
FF =0.787716
EFFICIENCY = 22.001 PERCENT
ACTIVE AREA EFF. = 24.277 PERCENT
COLLECTION EFFICIENCY = 96.048 PERCENT

********** SCAP2D — VERSION 4 **********

APPLIED VOLTAGE (VOLTS)	CURRENT (AMPS/CM^2)
0.00000	0.55218E+01
0.15000	0.55215E+01
0.30000	0.55212E+01
0.45000	0.55206E+01
0.60000	0.54151E+01
0.66000	0.48248E+01
0.69000	0.50504E+01
0.72000	0.27272E+01
0.75000	0.64819E+01
0.78000	-0.23837E+01
0.75696	0.36393E-01
0.61712	0.52566E+01

Fig. 1.4b Simulated terminal characteristics of the conventional p on n silicon concentrator cell.

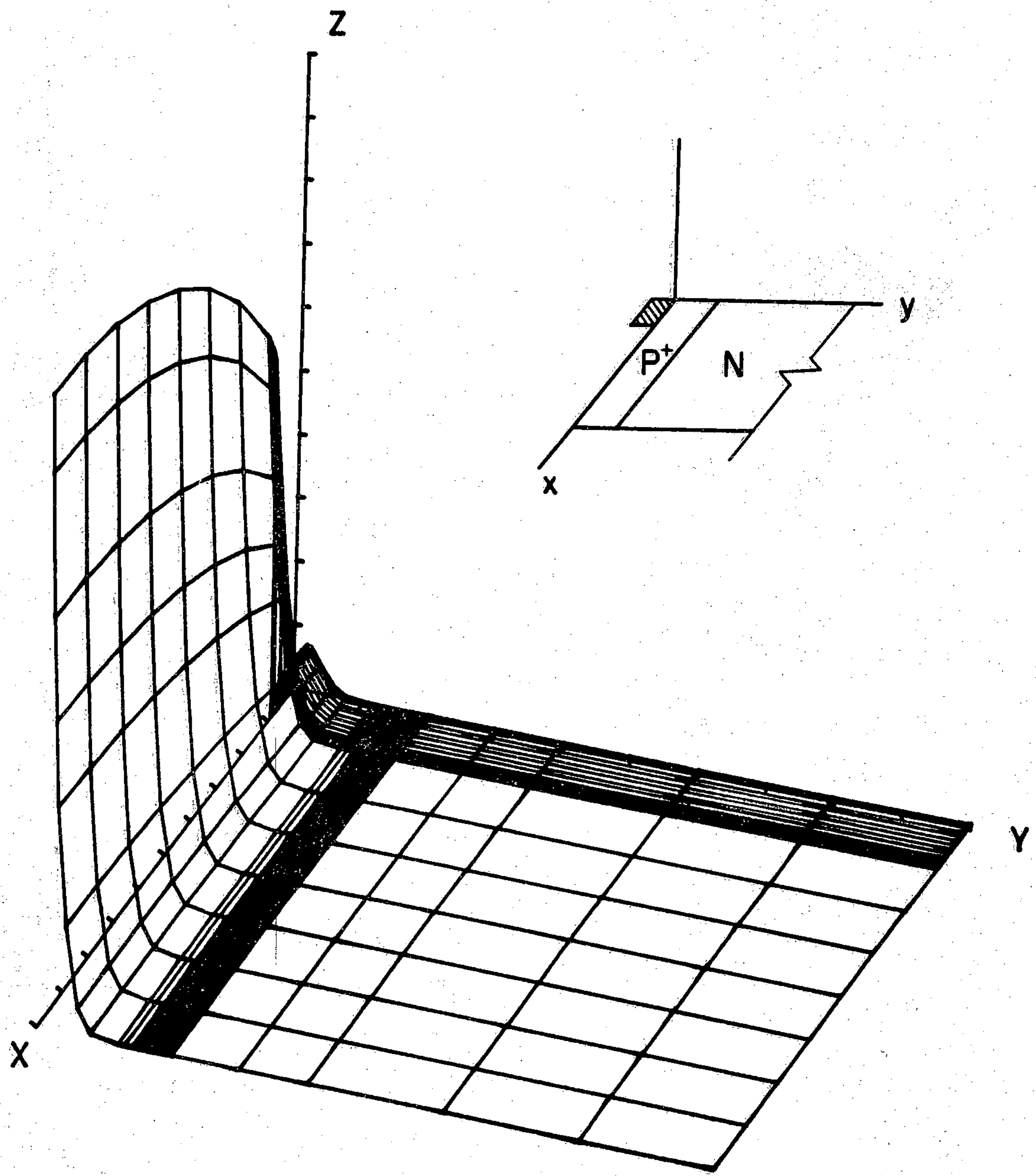

Recombination Rate at V_{oc}

Fig. 1.4c Plot of the internal recombination rate versus position within the p on n concentrator cell at open-circuit voltage.

PERCENT RECOMBINATION IN EACH REGION

							BASE				CONTACTS	
V	J(V)	BOT	TOP	LEFT	RIGHT	SURF	SRH	AUG	P^+	N^+	FRONT	BACK
0.00000	0.55218E+01	0.01	0.00	0.00	0.00	0.01	14.69	0.60	11.69	3.24	0.01	69.76
0.15000	0.55215E+01	0.01	0.00	0.00	0.00	0.01	14.70	0.60	11.69	3.24	0.01	69.75
0.30000	0.55212E+01	0.01	0.00	0.00	0.00	0.01	14.71	0.60	11.70	3.24	0.01	69.73
0.45000	0.55206E+01	0.01	0.00	0.00	0.00	0.01	14.70	0.60	11.77	3.24	0.03	69.65
0.60000	0.54151E+01	0.02	0.00	0.00	0.00	0.02	12.52	0.56	24.91	2.56	4.61	54.82
0.66000	0.48248E+01	0.03	0.00	0.00	0.00	0.03	8.27	0.54	41.51	1.61	13.63	34.41
0.69000	0.40504E+01	0.03	0.00	0.00	0.00	0.03	6.41	0.57	43.77	1.38	18.45	29.39
0.72000	0.27272E+01	0.03	0.00	0.00	0.00	0.03	4.96	0.62	42.97	1.27	23.17	26.98
0.75000	0.64819E+00	0.03	0.00	0.00	0.00	0.03	3.87	0.69	40.72	1.22	27.56	25.91
0.78000	-0.23837E+01	0.03	0.00	0.00	0.00	0.03	3.07	0.76	38.05	1.20	31.40	25.50
→ 0.75696	0.36393E—01	0.03	0.00	0.00	0.00	0.03	3.66	0.70	40.12	1.21	28.51	25.77
0.62712	0.52566E+01	0.03	0.00	0.00	0.00	0.03	10.68	0.53	33.80	2.08	8.40	44.48

Fig. 1.4d Internal recombination summary from the SCAP2D simulation of the conventional p on n concentrator cell.

dominant loss mechanisms for this cell, the design is altered using the New South Wales approach [5]. Finally, we examine the internal device physics of a backside-contact cell similar to the Stanford design [6]. Identical, high-quality material is assumed for each of the three cells in order to assess the role of device design on cell performance.

The Sandia-like p on n cell is displayed in Fig. 1.5; it is fabricated in a 305 μm thick, 0.3 Ω-cm substrate. The p^+ emitter is 0.4 μm thick with a peak concentration of 1.5×10^{20} cm^{-3}, and the back-surface field is a diffused junction 1.0 μm thick with a peak doping of 5.0×10^{19} cm^{-3} (complementary error functions were used for both profiles). The Shockley-Read-Hall lifetimes were modeled by

$$\tau = \frac{\tau_o}{1 + N/N_c} , \tag{1.7}$$

where τ_o, the SRH lifetime in intrinsic material was taken to be 1000 μsec and N_c, which controls how the SRH lifetime degrades with doping, was set to 7.1×10^{15} cm^{-3}. Auger recombination was also modeled and the passivated surfaces were characterized by a surface recombination velocity of 10 cm/sec.

The results of a two-dimensional physical simulation of the p on n cell are summarized in Table 1.1; the simulated conversion efficiency under concentration exceeds 20%. Simulation results show that 80% of the available photons are collected. About one-half of the lost photocurrent is due to reflection and shadowing; the other half of the loss is about equally divided between carrier recombination within the cell ($\sim$ 4%) and transmission of above-bandgap photons through the 300 μm thick cell.

CELL PARAMETER	*VALUE*
V_{OC}	0.757 volts
J_{SC}	5.52 A/cm^2
FF	79%
η	22%
$J_{SC}/J_L(max)$	80%
Internal CE	96%
Shadow + Reflection	9.4%

Table 1.1. Simulated performance of the p on n silicon concentrator cell at T=24°C under 180X AM1.5 direct suns.

Figure 1.6 summarizes the recombination losses at V_{OC} for this cell as revealed by physical simulation. Note the relatively small ($\sim$ 4%) contribution of base recombination to the dark current. The heavy base doping, in contrast to earlier cell designs, effectively suppresses forward biased injection of holes into the base. The dominant V_{oc}-loss mechanism is recombination within the thin, heavily-doped p-type emitter. Since the emitter is well-passivated, this current component is due to injected minority carriers recombining within the volume of the emitter and can be described by

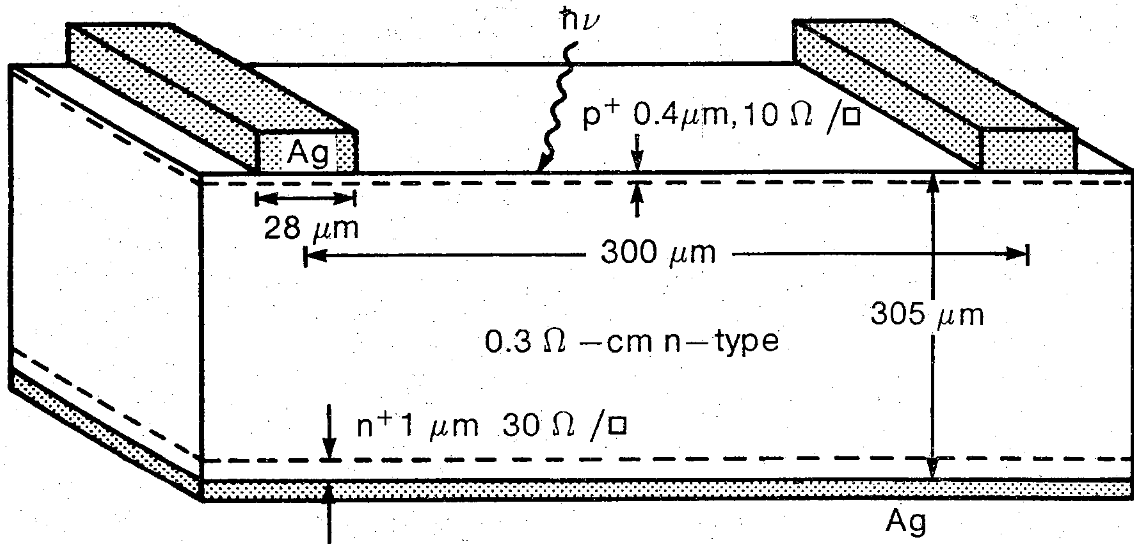

Fig. 1.5 Physical structure of the Sandia-like [4] p on n concentrator cell.

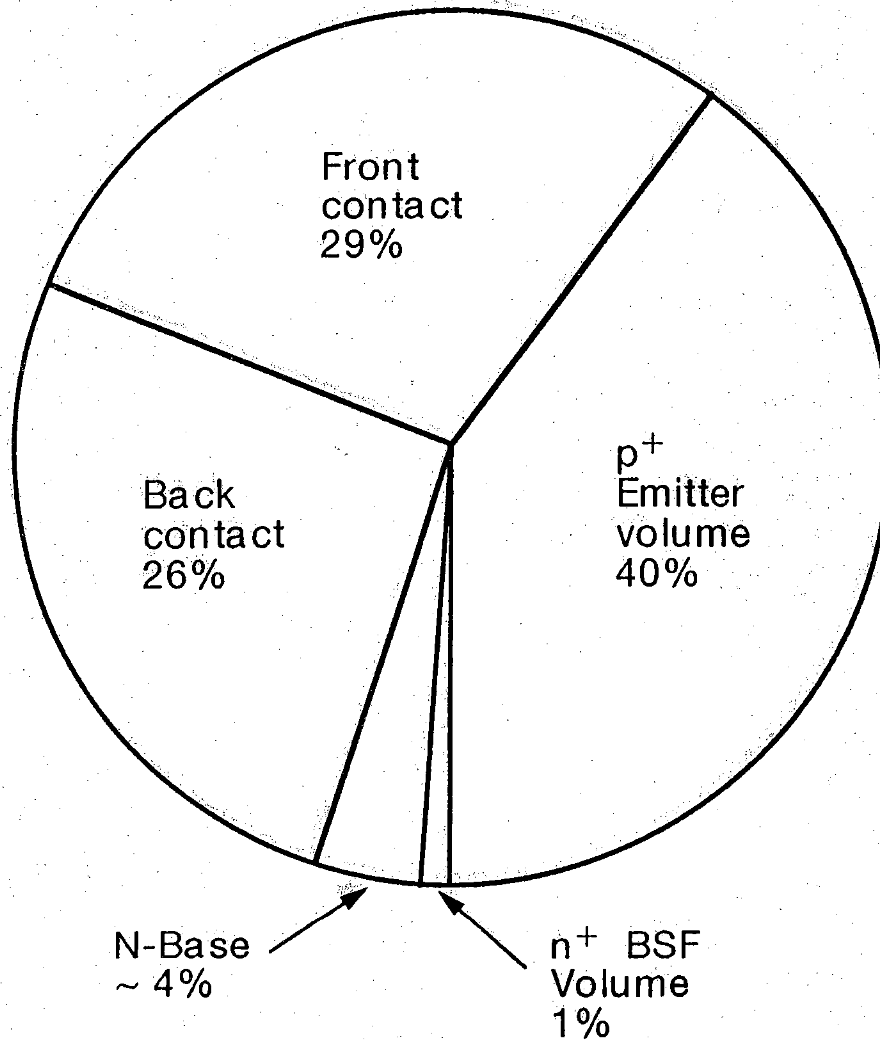

Fig. 1.6 Recombination analysis of Sandia-like p/n silicon concentrator cell at V_{OC}.

$$J_E(p^+bulk) = q\frac{{n_{iE}}^2}{N_A}\frac{W_E}{\tau} , \tag{1.8}$$

where n_{iE} is the intrinsic carrier concentration in the emitter, N_A is the average doping, W_E is the width of the emitter, and τ is the minority carrier lifetime. The emitter component of the dark current dominates for two reasons. First, so-called bandgap narrowing effects effectively shrink the bandgap within the heavily doped emitter, so that n_{iE} may greatly exceed its value in intrinsic silicon, n_{io} [7]. Figure 1.7 shows that in the heavily doped emitter, ${n_{iE}}^2$ may be several times the value in lightly doped silicon. Secondly, the emitter recombination rate is high because of the dominance of Auger recombination in the heavily-doped emitter. The Auger-limited, low injection minority carrier lifetime,

$$\tau = \frac{1}{C_p{N_A}^2} , \tag{1.9}$$

is only one nanosecond in p-type silicon doped to 1×10^{20} cm^{-3}.

Figure 1.6 also shows that more than half of the recombination losses in this cell are due to minority carriers recombining at the metal contacts. These losses are a consequence of "bandgap narrowing" which causes a substantial injection of minority carriers into the heavily doped regions where they can recombine at the metal contacts. The back-surface field does improve the performance of this cell, but it is not a perfect minority carrier mirror; a number of minority carriers reach the back metal contact and recombine there.

We consider next a modification of the cell design based on the New South Wales approach [5]. A microgrooved top surface and low area grid reduces reflection and shadowing losses by a factor of three. In addition, the area of contact between the metal and p^+ emitter is reduced by a factor of 5. Simulation results, summarized in Table 1.2, show an increase in both J_{SC} due to the reduced shadowing and improved light-trapping.

CELL PARAMETER	*VALUE*
V_{OC}	0.768 volts
J_{SC}	6.05 A/cm^2
FF	77%
η	24%
$J_{SC}/J_L(max)$	88%
Internal CE	96%
Shadow + Reflection Losses	3.1%

Table 1.2. Simulated performance of the p on n silicon concentrator cell redesigned according to the New South Wales approach. The temperature is 24°C; the spectrum is 180X AM1.5 direct normal suns.

Figure 1.8 quantifies the various loss mechanisms for this cell. As expected, the losses

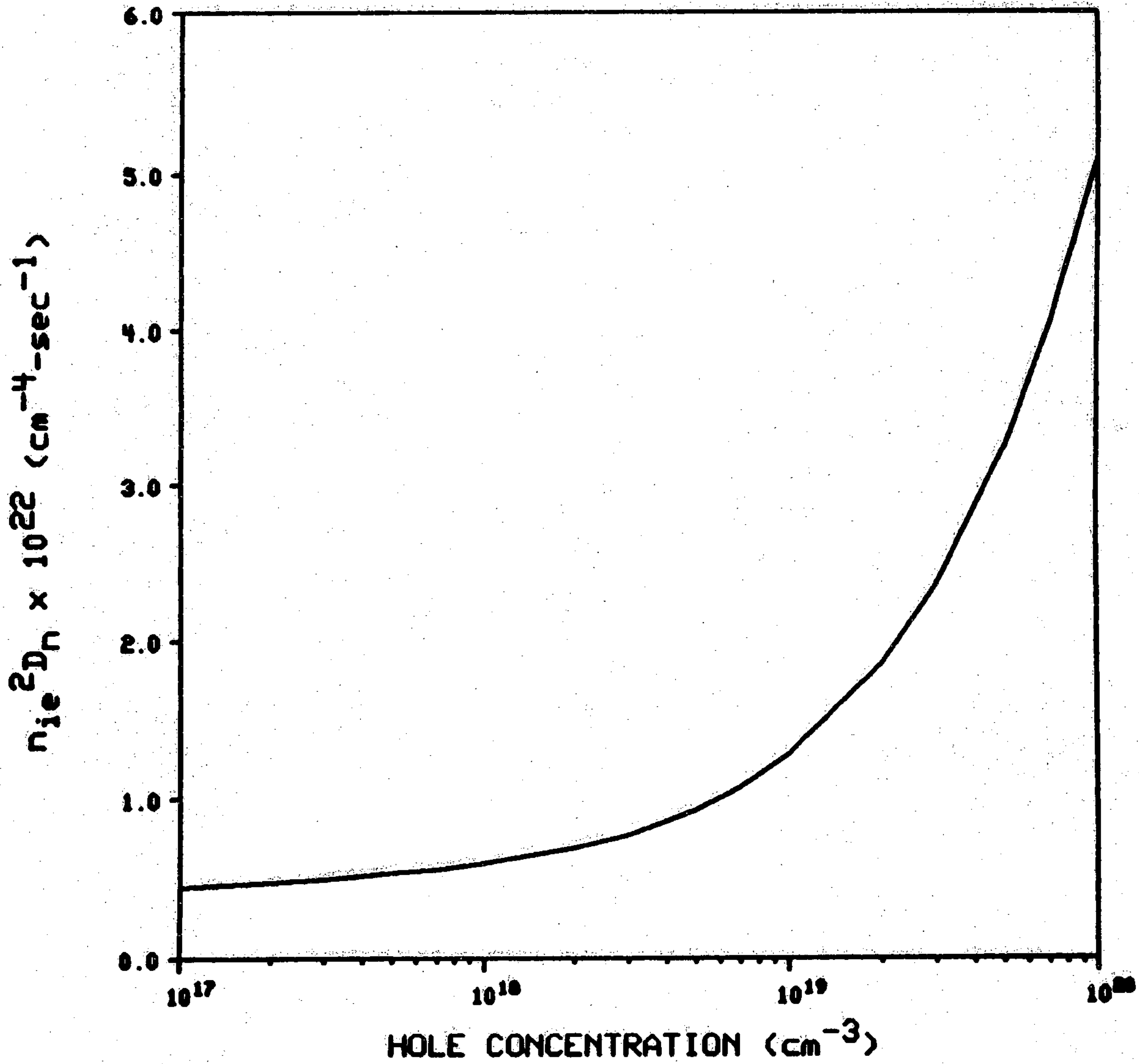

Fig. 1.7 Effective intrinsic carrier concentration squared times the minority carrier diffusion coefficient versus p-type doping. (After Slotboom and DeGraaff [7].) This product, rather than n_{ie}^2 alone is plotted because it is the quantity typically determined by experiments.

Recombination analysis of the p/N silicon concentrator cell redesigned according to the New South Wales approach

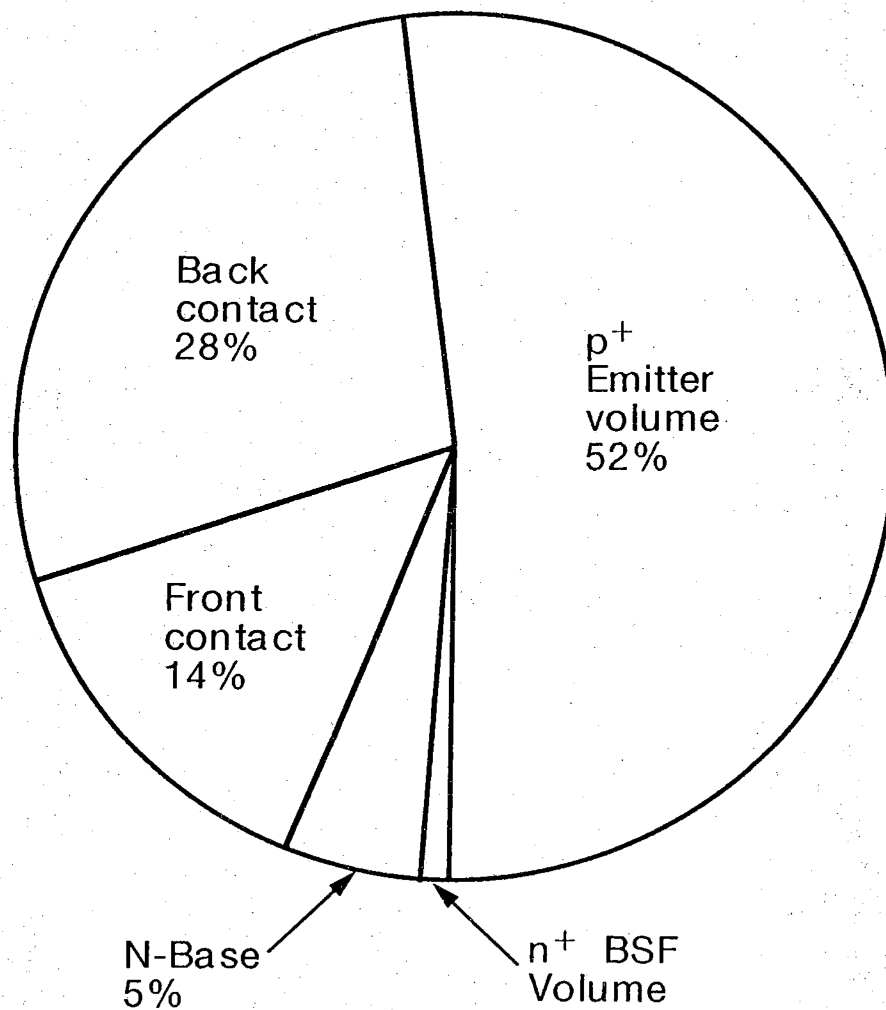

Fig. 1.8 Recombination analysis of the redesigned Sandia-like p on n concentrator cell at V_{OC}.

associated with recombination at the front metal contact have been drastically reduced by the small area contacts. Part of the increase in V_{OC} displayed in Table 1.2 is due to this reduction in recombination losses. As a result of the increase in J_{SC} and V_{OC}, the cell's efficiency has been raised by 2 percentage points. This cell's fill factor is degraded by resistive drops in the thin p-type emitter. The New South Wales cell [5], which is n on p rather than the p on n simulated here, has a lower sheet resistance emitter and a correspondingly better fill factor which enables it to attain a somewhat higher, 25%, conversion efficiency. According to these simulation studies, silicon cell design should be directed at suppressing recombination in the emitter volume and at the rear metal contact. Further increases in J_{SC} are possible if the already low shadowing losses can be eliminated and if the high internal quantum efficiency can be improved. The Stanford backside point contact cell [6] achieves both objectives. Figure 1.9 shows the physical structure of the Stanford cell. Both the p- and n-type diffused junctions are reduced to small dots on the backside of the wafer, so grid shadowing losses are eliminated, and Auger recombination in the volume of the diffused regions is reduced — so is recombination at the metal-semiconductor contacts. The light base doping is used to maximize Shockley-Read-Hall lifetimes; its resistance is low because the base operates in high level injection. To maintain a high internal collection efficiency and open-circuit voltage, the cell must be thin. Light trapping techniques are then essential to make the semiconductor appear optically thick.

Table 1.3 summarizes the electrical performance of the cell under concentration. The very substantial reduction of recombination losses achieved by reducing the volume of the heavily doped regions and the area of the metal-semiconductor contacts is reflected in the especially high open-circuit voltage. The recombination analysis at V_{OC} for this cell, displayed in Fig. 1.10, shows that the p^+ volume, the n^+ volume, and the metal contacts contribute about equally to the recombination losses. Recombination losses associated with the intrinsic cell are so low that parasitic losses associated with recombination at the perimeter of the cell must be considered. For this cell, recombination at the perimeter is about equal to the sum of all the losses displayed in Fig. 1.10. Because perimeter recombination was not simulated and the extrinsic series resistance was assumed to be zero, the simulated efficiency is about 2 percentage points aboved the observed value.

CELL PARAMETER	*VALUE*
V_{OC}	0.826
J_{SC}	6.39
FF	85%
η	30.1%
$J_{SC}/J_L(max)$	93%
Internal CE	99.5%
Shadow + Reflection Loss	0

Table 1.3. Simulated performance of the Stanford backside point contact cell (T=24°C, AM 1.5 direct normal, at 180X).

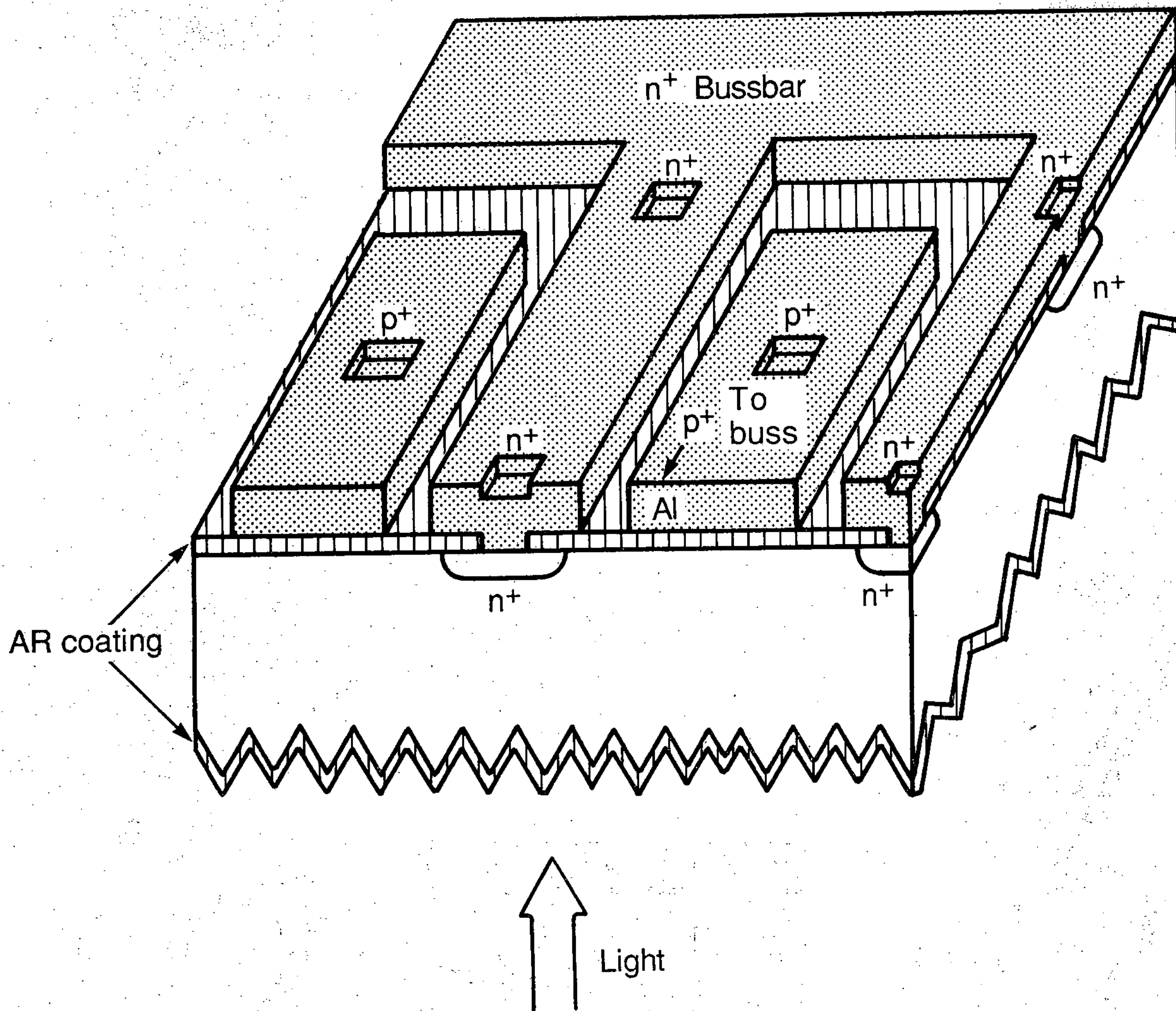

Fig. 1.9 Physical structure of the Stanford-like backside point contact cell [6].

Recombination analysis of the backside point contact cell at V_{oc}

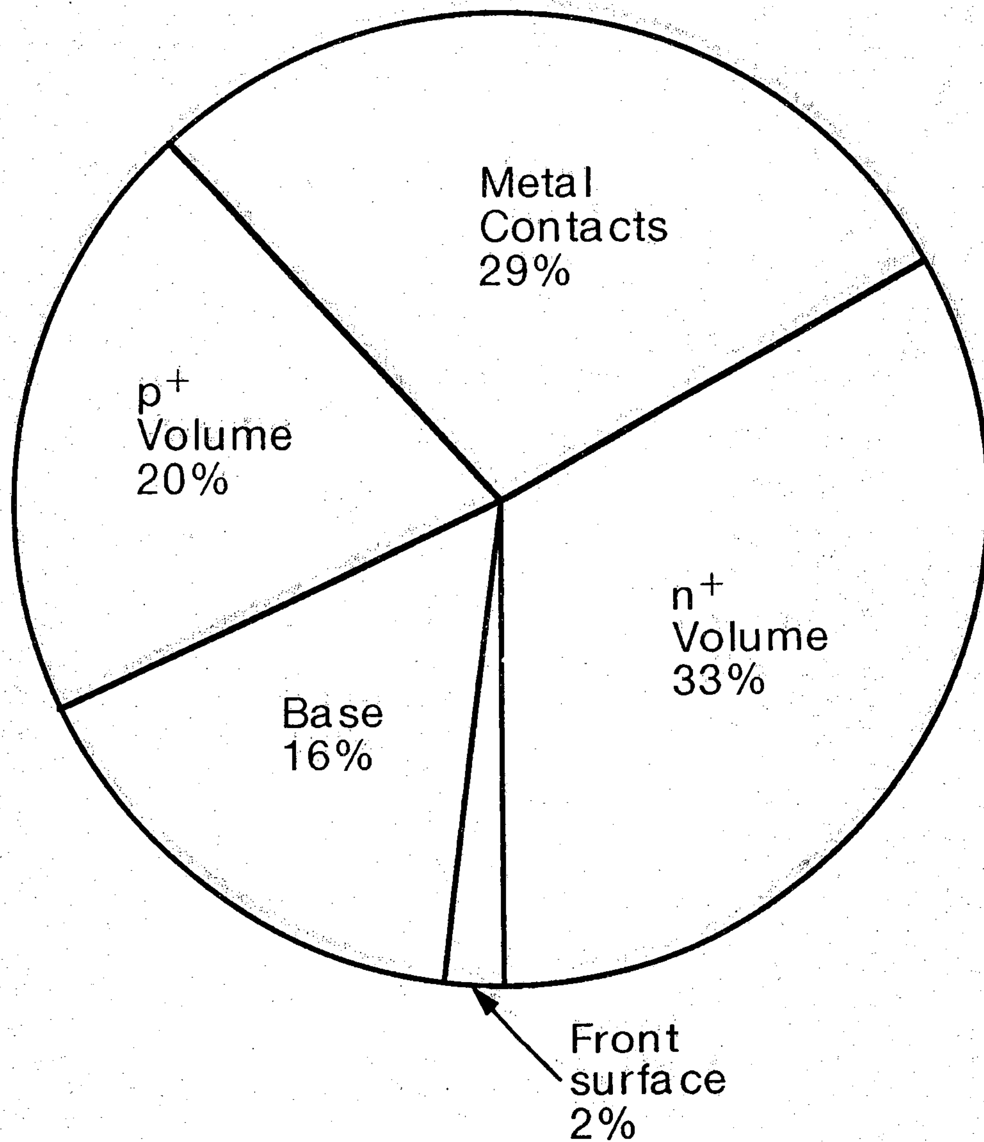

Fig. 1.10 Recombination analysis of the Stanford-like point contact cell at V_{OC}.

These examples illustrate how physical device simulation is used to probe the internal device physics of solar cells. Device design must be guided by such a detailed understanding of the internal device physics. During the late 1970's and early 80's, silicon cell simulation was being developed, tested, and verified. An improved understanding of recombination losses in high-efficiency cells was a by-product of this research and contributed to the efficiency gains during this period. By the early 80's, silicon simulators were considered predictive. At this stage, when the technology might have been viewed as mature, simulation was used to identify new design approaches [8] which ultimately led to the very high efficiencies recently reported [6].

1.5. DEVICE PHYSICS OF GaAs CELLS

Although very high efficiencies have been reported for gallium arsenide solar cells under both one-sun and concentration [9,10], our understanding of their internal device physics is not mature by silicon standards. The most common cell design, the p on n heteroface displayed in Fig. 1.11, has not changed appreciably for several years, but efficiencies have continued to rise as anti-reflection coatings, material quality, and fabrication techniques have improved. Very high conversion efficiencies have recently been reported by Spire for this basic cell design [9]. Experiments to probe the internal device physics have just recently begun (e.g. [11,12]), as has the serious use of physical device simulation. Simulation now describes cell performance reasonably well and can be used to assess the potential of design alternatives. In this section, we examine the device physics of the conventional p on n heteroface cell, identify the dominant loss mechanisms, and assess some design options.

The basic cell structure, displayed in Fig. 1.11, consists of a p^+-emitter and an n-type base. The heavily doped buffer layer serves as a minority carrier mirror, and the wide-bandgap $Al_{0.9}Ga_{0.1}As$ window layer passivates the front surface. The heavily-doped p-type cap layer, which facilitates ohmic contact, is removed between the metal grid lines. Numerical simulations by PUPHS1D [2] demonstrate that the bandgap of the window ($\simeq$ 2 eV) permits a substantial photogeneration of carriers (about 5% of the available photons are absorbed in a 500 Å thick window). A few percent of the available photons are also generated in the n^+ buffer layer. The simulated internal quantum efficiency is compared to a typical measured value [12] in Fig. 1.12. The drop in quantum efficiency at short wavelength is due to absorption in the window layer, but the window layer is not dead. A front surface recombination velocity at the AlGaAs surface of 5×10^6 cm/sec (which is somewhat below the value of $\sim 10^7$ cm/sec typical of a bare GaAs surface) is needed to model the short wavelength quantum efficiency. About one-half of the carriers photo-generated in the window layer are collected. The long wavelength quantum efficiency is quite high; very long base lifetimes are implied (a value of 15 nsec was used in the simulation). The peak quantum efficiency, typically 90-95%, is very high, but it contrasts with the results for silicon in which the quantum efficiency routinely peaks very near 100%. The peak quantum efficiency can be explained by assuming a recombination velocity at the heteroface of several times 10^4 cm/sec to a few times 10^5 cm/sec, which is substantially above the 10^4 cm/sec commonly assumed as an upper limit. But other explanations, such as a parasitic absorption mechanism that does not generate carriers, cannot be ruled out.

Short circuit current losses for this cell are summarized in Fig. 1.13. Reflection and shadowing by the top metal grid are the largest component of optical loss. The sizeable loss contributed by the n^+ buffer layer and substrate indicates that the cell's active layer is not thick enough optically, but increasing its thickness would degrade the open-circuit voltage (in this regard, GaAs cells could benefit from light-trapping techniques like those

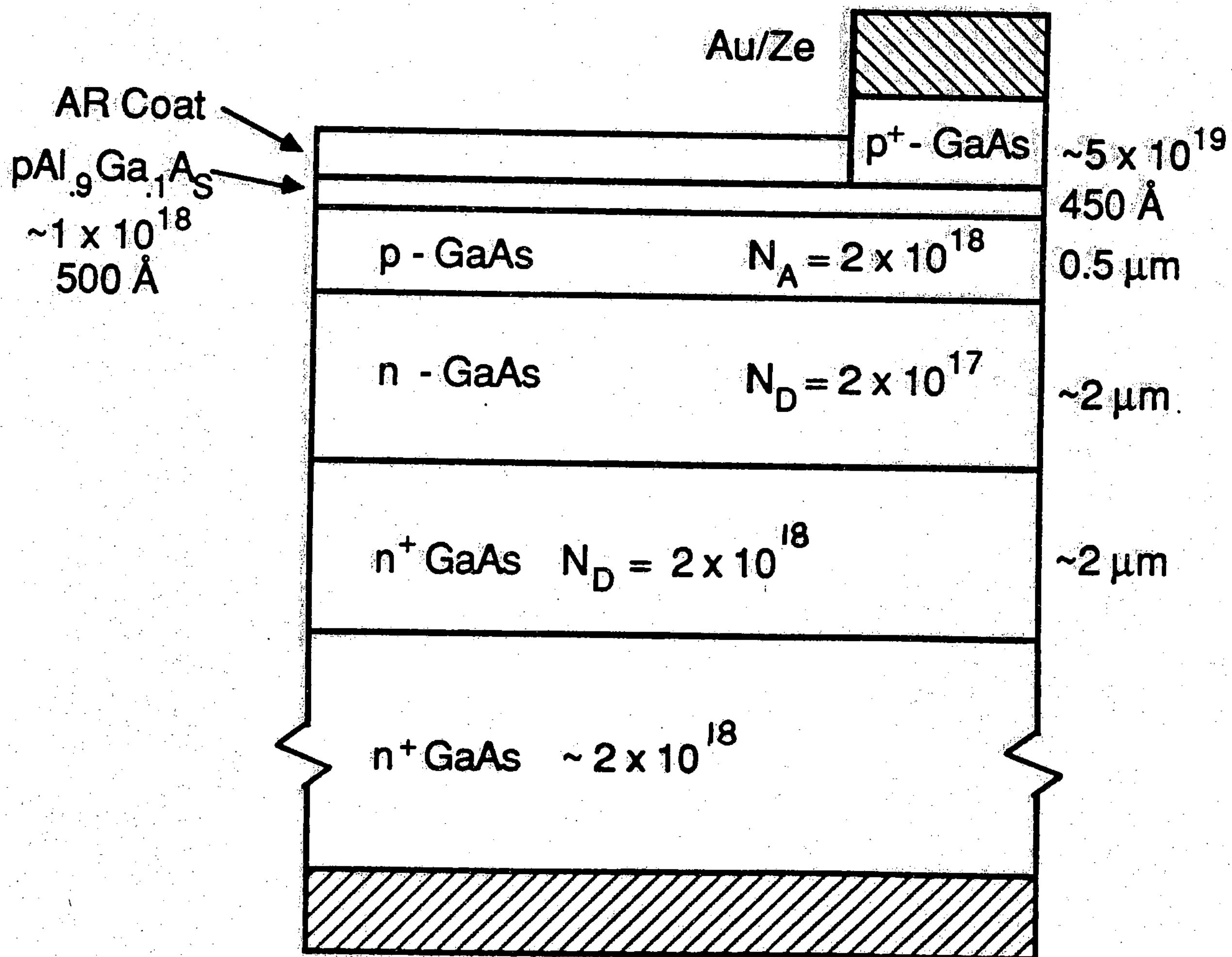

Fig. 1.11 Physical structure of the Spirelike p on n GaAs heteroface cell [9].

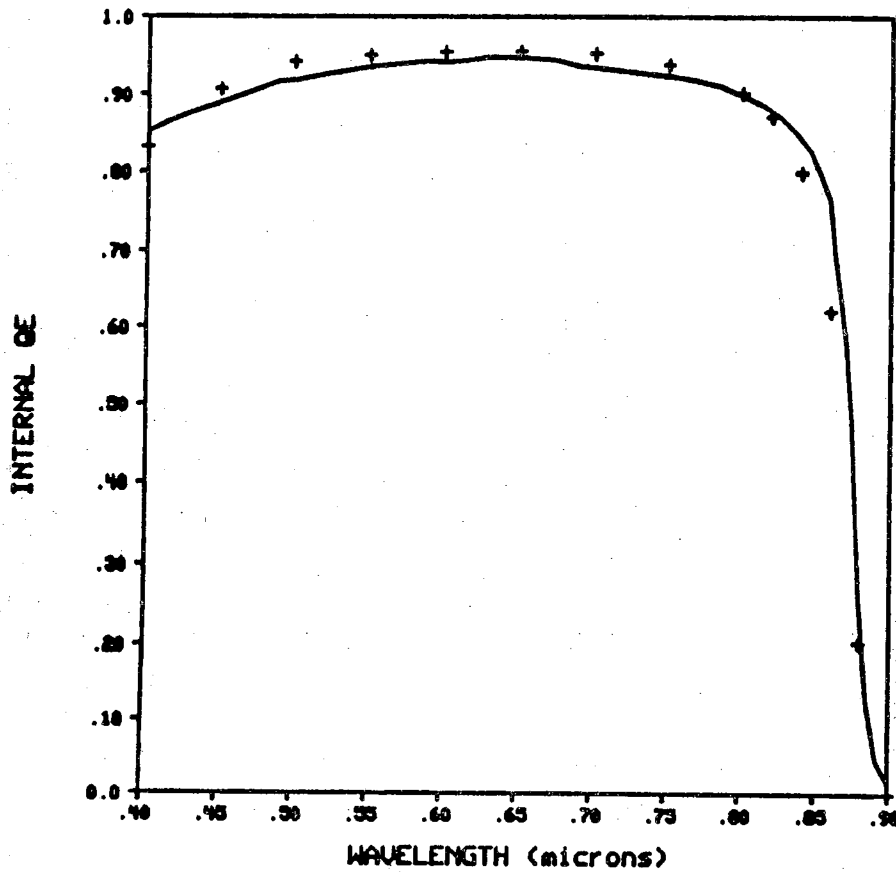

Fig. 1.12 Internal quantum efficiency versus wavelength for a typical p on n heteroface cell. (solid line, PUPHS1D simulation, points are from [12])

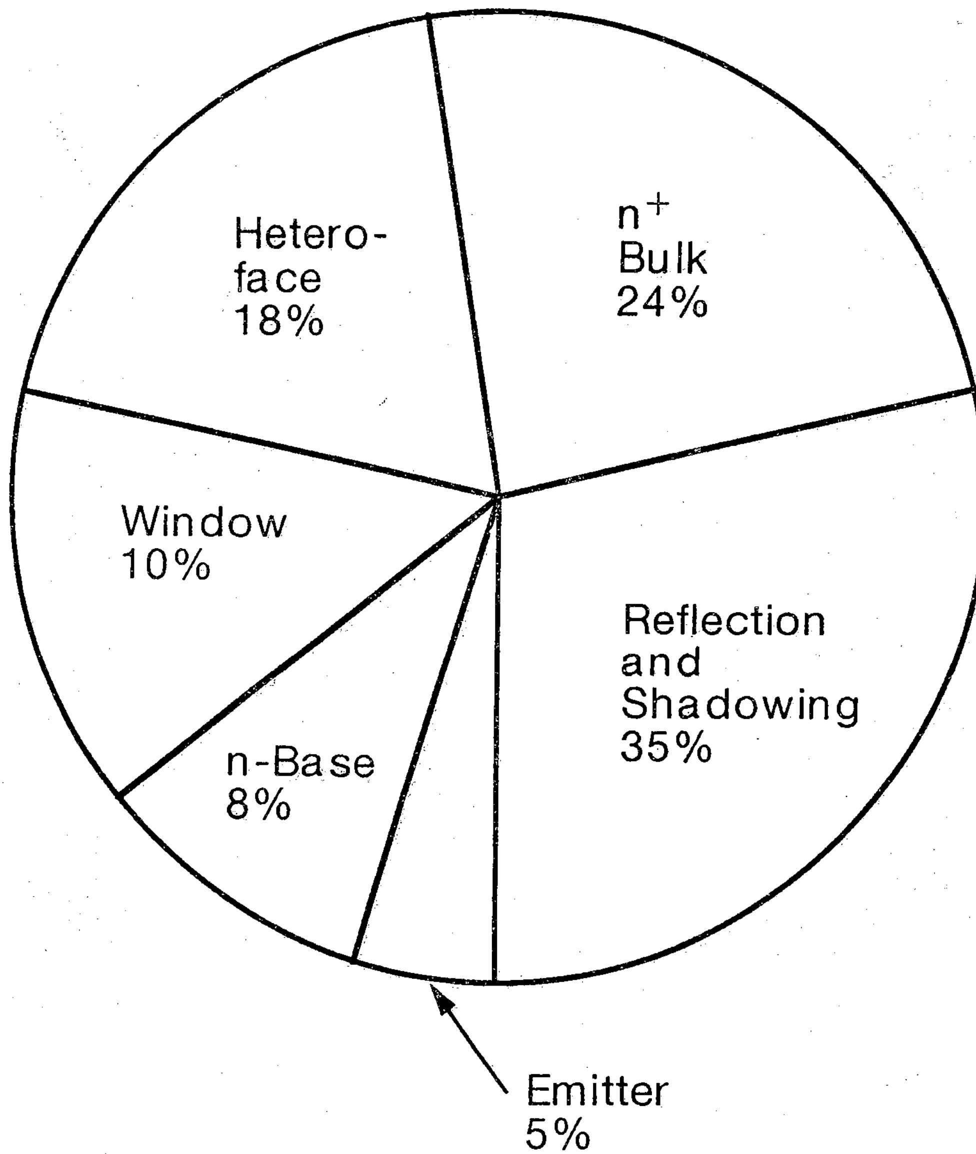

Fig. 1.13 Short-circuit current loss analysis of the p on n GaAs heteroface cell. In the simulated cell, 13% of the available photo-generated carriers are lost. This chart shows where those photons are lost.

employed for Si cells). The loss contributed by the heteroface reflects the high interface recombination velocities implied by the peak internal quantum efficiency.

Recombination losses at open-circuit voltage are summarized in Fig. 1.14. In contrast to the silicon p on n cells, the GaAs cell's dark current is base-dominated. Note that the emitter doping for the GaAs cell is not extremely high, so minority carrier electrons are injected into the emitter. But injection of minority carriers into the emitter does not have the dire consequences that it does for silicon cells because the metal contacts are passivated by the heteroface and the lifetimes in the emitter are relatively long ($\sim$ 2 nsec). The performance of the n^+ back-surface field is not severely compromised because majority carrier degeneracy is strong in n-type GaAs and acts to counter bandgap shrinkage. For n on p cells, however, the performance of p^+ back surface fields should be degraded by bandgap shrinkage, which may explain why heterojunction back-surface fields have proved effective for such cells [14].

The simulations show a sizeable, though not dominant, emitter component to the dark current which is a consequence of the relatively high heteroface recombination velocity used to match the low peak internal quantum efficiency. One might expect that the emitter component could be suppressed by increasing the emitter doping, but the experiments show that the dark current does not vary with emitter doping [12]. Simulations show that the reduction in the emitter dark current associated with heavier doping is offset to some degree by bandgap narrowing and by reductions in lifetime. Strong variations of dark current with emitter design should not be observed until the dominant loss, base recombination, is suppressed.

Figure 1.14 also shows that the dark current at V_{OC} is dominated by the n=1 current component. The one-sun maximum power point, however, occurs at voltages for which there is some n=2 current. Although the n=2 current does not affect the cell's performance under concentration, or even the open-circuit voltage at one-sun, it can lower the one-sun fill factor. Experiments demonstrate that the n=2 current in 0.5 cm by 0.5 cm cells is dominated by recombination in the space-charge region at the cell's perimeter [11].

Table 1.4 summarizes the simulated performance of the Spire-type p on n heteroface cell at one-sun and the performance of a similar cell (with a redesigned grid) under concentration. These results were obtained with a two-dimensional, AlGaAs/GaAs simulator. The table shows that about 87% of the available photons are collected; in the very best silicon cells the corresponding fraction exceeds 95%. The cell's dark current is primarily due to recombination in the n-type base. Under concentration, simulations of a similar cell (with a very conservative metal grid that results in 11% shadowing) show a conversion efficiency of more than 27%.

When we consider optimizing this cell, it is clear that the first objective must be to raise the fraction of available carriers that are collected. The reason for the low peak internal quantum efficiency (low, that is, by silicon standards) must first be identified. As discussed previously, a tentative explanation is that the heteroface recombination velocity exceeds 10^4 cm/sec. When this value is lowered to 10^4 cm/sec, simulations show nearly 100% peak internal quantum efficiency. Modest improvements in cell performance can also be achieved by reducing the dark current. The remedy for silicon, reduction of the p^+ emitter volume and the area of the metal-semiconductor contacts is not expected to benefit GaAs cells. To reduce dark currents, the focus should be on suppressing the base current, which is most easily accomplished by increasing the base doping (if the diffusion length in the base can be maintained). Figure 1.15 shows that no fundamental mechanism limits the hole lifetime in n-GaAs until the doping exceeds 10^{18} cm^{-3}, so base

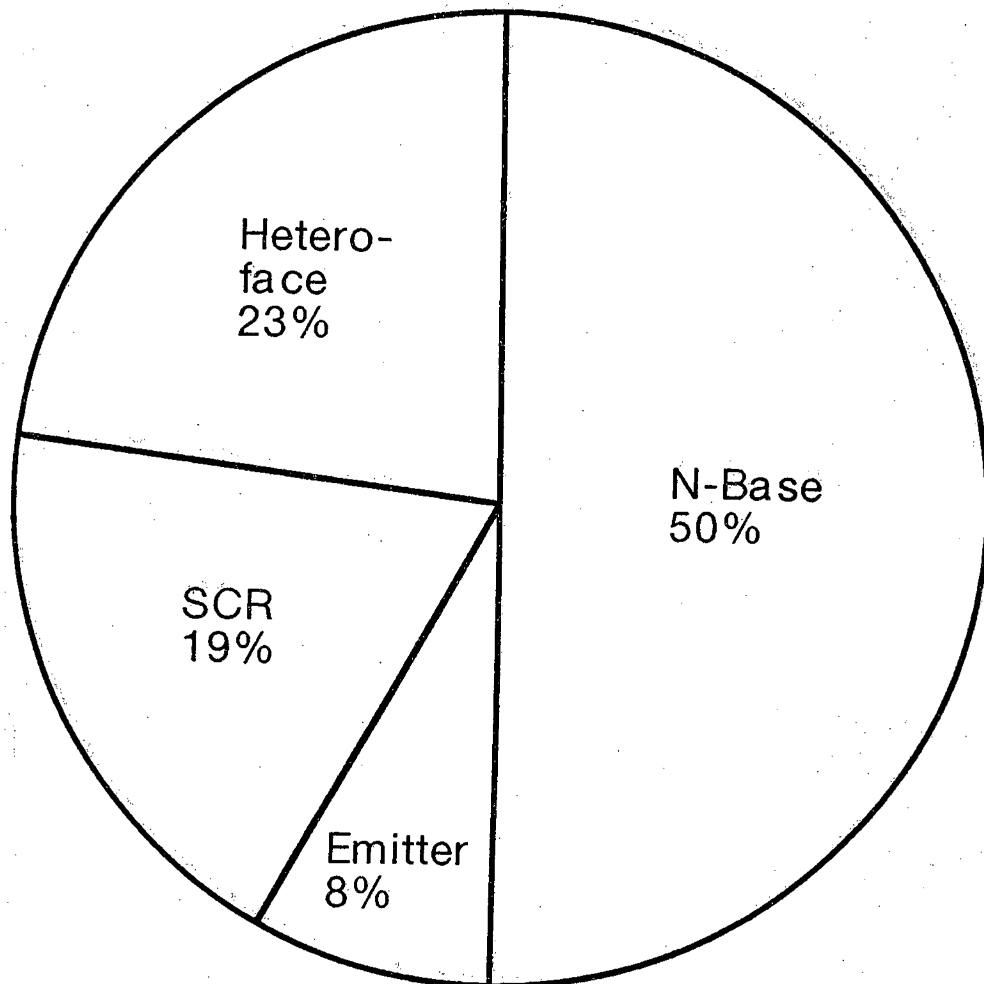

Fig. 1.14 Recombination analysis of the p on n GaAs heteroface cell at the one-sun V_{OC}.

dopings higher than $2 \times 10^{17} cm^{-3}$ could be employed. This approach has been adopted in the Varian p on n heteroface cell [10]. The use of heterojunction back-surface fields to suppress dark current might also be considered, but in this case the base must be thickened to prevent a loss of photocurrent [13]. Since the back-surface field will be located more than a diffusion length beyond the junction, significant benefits are not expected for heterojunction back-surface fields in p on n cells. Finally, note from Fig. 1.15 that 1 nanosecond lifetimes can be maintained in the p-type emitter for doping densities near 10^{19} cm^{-3}. For such lifetimes, the short wavelength internal quantum efficiency does not suffer (recent experiments provide confirmation [12]). The implication is that the emitter doping can be substantially raised to lower the emitter sheet resistance without sacrificing internal quantum efficiency.

Table 4 also shows the simulated performance of an "optimized" cell, which was designed as discussed above. The cell is identical to that displayed in Fig. 1.11 except that the peak internal quantum efficiency has been raised to nearly 100% by lowering the heteroface recombination velocity to 1×10^4 cm/sec, the emitter doping has been raised to 8×10^{18} cm^{-3}, and the base doping has been raised to 5×10^{17} cm^{-3}. The lowered sheet resistance of the p^+ emitter allowed the front grid to be redesigned to lower shadowing losses to 5% without degrading the fill factor. A significant gain in performance is predicted; the cell shows an conversion efficiency of 29%. Even for with this very high conversion efficiency, the short-circuit current represents only 85% of the available photons; for the best silicon cells, the corresponding fraction exceeds 95%. Conversion efficiencies in excess of 30% are achievable if the short-circuit current performance of GaAs cells can be raised.

CELL PARAMETER	*1-SUN*	*500-SUNS (a)*	*500-SUNS (b)*
V_{OC}	1.038 volts	1.19	1.22
J_{SC}	27.4 mA/cm^2	10.9	11.4
FF	86%	87	86
η	24.6%	27.1	29.0
$J_{SC}/J_L(max)$	87%	81	85
Internal CE	90%	89	88
Shadow + Reflection	5%	11	6

Table 1.4. Simulated performance of the p on n heteroface GaAs cell. The first column refers to the cell displayed in Fig. 11 under an AM1.5 global spectrum normalized to 100 mW/cm^2 [21]. The second column refers to a similar cell at 500 AM1.0 direct normal suns (the grid was redesigned for high-current operation which increased shadowing to 11%). The final column refers to an "optimized" cell which the emitter and base doping were increased, the grid redesigned to lower the shadowing losses, and the heteroface recombination velocity lowered to 1.0×10^4 cm/sec. All simulations were performed at 25°C.

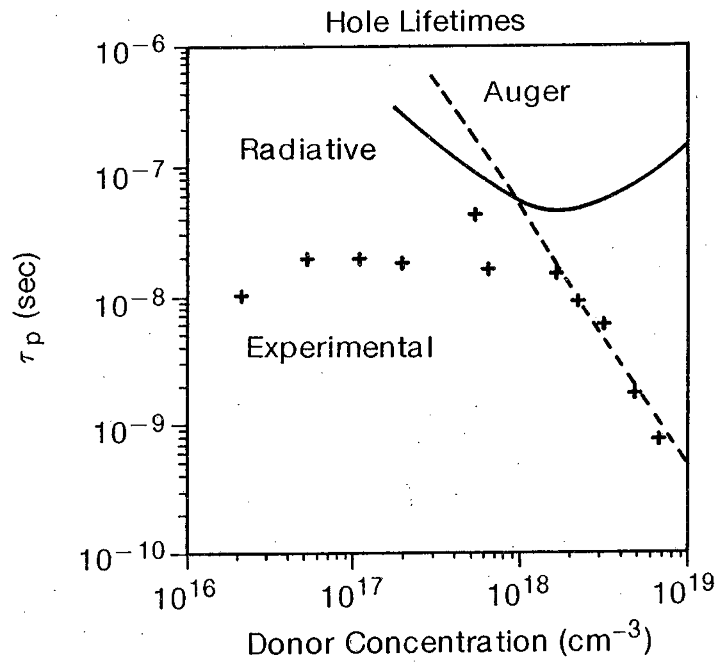

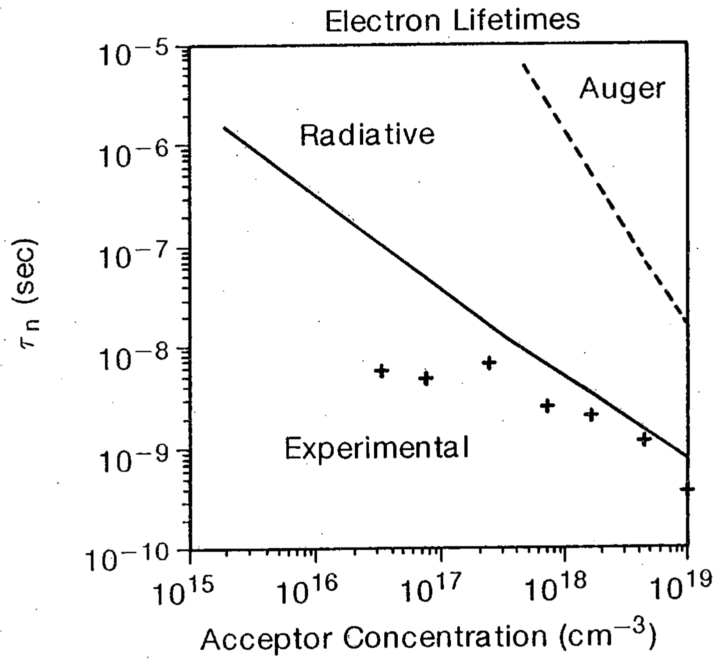

Fig. 1.15 Minority carrier lifetimes versus doping density in n- and p-type GaAs. Data points for electrons are from [15] and for holes from [16]. Band-to-band radiative lifetimes are from [17] for electrons and from [18] for holes. Band-to-band Auger lifetimes are from [19].

1.6. CONCLUSIONS

In this chapter the internal device physics of a number of different solar cell designs in two different crystalline semiconductors has been studied. A unifying theme of the discussion was the role that detailed device simulation plays in guiding solar cell design. Numerical techniques are now highly refined and are capable of solving the governing equations in one-, two-, or even three-dimensional crystalline or amorphous [20] solar cells. Efforts to develop predictive simulators now focus not on numerical techniques but on understanding the physics to be modeled and at measuring the various material parameters that appear in the model. The development of a predictive model is a collaborative effort consisting of theoretical model development and experimental basic studies. Device development benefits from the knowledge gained from this collaborative effort, and a predictive model that can replace many time-consuming experiments eventually results. Even when a technology is not mature, model development has a positive benefit by focusing attention on what is known and what is not and by identifying the key problems to be solved.

Some general conclusions regarding the design of silicon, GaAs, and all crystalline cells can be derived from this discussion. The first is the importance of maximizing short-circuit current; the very best silicon cells make use of long-lifetime material and light-trapping techniques to collect about 96% of the available photocurrent [6]. This appears to be the key area of opportunity for improving the already high efficiency of GaAs cells (the best GaAs cells collect about 88% of the available photocurrent [9]). Bandgap narrowing effects play a dominant role is silicon cell design; because of it, the injected minority carrier concentration is enhanced so that Auger recombination and recombination at the metal contacts dominates. Much of silicon cell design focuses on "designing around" heavy doping effects. The highest efficiencies have been attained by reducing the volume of the heavily doped diffused areas and by reducing the metal-semiconductor contact area. By this approach, one-sun V_{OC}'s that are 61% of the silicon bandgap have been achieved [6]. For GaAs cells, bandgap narrowing may occur (especially in p^+ GaAs), but its consequences are not so dire. Auger recombination does not typically dominate, and metal contacts can be passivated to minority carriers by using heterojunctions. Although GaAs currently out-performs silicon with respect to open-circuit voltage (one sun V_{OC}'s that are 72% of bandgap have been reported [9]), simulations suggest that modest improvements are achievable by suppressing the base current. Both materials display high fill factors (typically just under 80% for Si at one-sun and just over 80% for GaAs). A conversion efficiency of 30% under concentration is achievable for both silicon and GaAs cells.

Acknowledgement- The author is indebted to E.K. Banghart for performing the simulations of silicon cells and to P.D. DeMoulin for the GaAs simulations. He also benefited from extensive discussions with S.P. Tobin of Spire Corporation and J.M. Gee of Sandia National Laboratories. Development of the simulation tools described in this paper was supported by Sandia National Laboratories.

CHAPTER 1 REFERENCES

[1] C.H. Henry, "Limiting Efficiencies of Ideal Single and Multiple Energy Gap Terrestrial Solar Cells," *J. Appl. Phys.,* Vol. 51, pp. 4494-4500, 1980.

[2] M.S. Lundstrom and R.J. Schuelke, "Numerical Analysis of Heterostructure Devices," *IEEE Trans. Electron Dev.,* Vol. ED-30, pp. 1151-1159, 1983.

[3] J.L. Gray and R.J. Schwartz, "Two-Dimensional Computer Simulation of Single Crystal Silicon Concentrator Cells," *Proc. 17th IEEE Photovoltaic Spec. Conf.,* pp. 1297-1302, 1984.

[4] R.D. Nasby, C.M. Garner, F.W. Sexton, J.L. Rodriguez, B.H. Rose, and H.T. Weaver, "High Efficiency p^+—n—n^+ Silicon Concentrator Solar Cells," *Solar Cells,* Vol. 6, pp. 49-58, 1982.

[5] M.A. Green, Z. Jianhua, A.W. Blakers, M. Taouk, and S. Narayanan, "25-Percent Efficient Low-Resistivity Silicon Concentrator Solar Cells," *IEEE Electron Dev. Lett.,* Vol. EDL-7, pp. 583-585, 1986.

[6] R.A. Sinton, Y. Kwark, J.Y. Gan, and R.M. Swanson, "27.5-Percent Efficient Silicon Concentrator Solar Cells," *IEEE Electron Dev. Lett.,* Vol. EDL-7, pp. 567-569, 1986.

[7] J.W. Slotboom and H.C. de Graaff, "Measurements of Bandgap Narrowing in Si Bipolar Transistors," *Solid-State Electron.,* Vol. 19, pp. 857-862, 1976.

[8] J.L. Gray and R.J. Schwartz, "Why Don't We Have a 30% Efficient Silicon Solar Cell," *Proc. 18th IEEE Photovoltaic Specialists Conf.,* pp. 568-572, 1985.

[9] S.P. Tobin, C. Bajgar, S.M. Vernon, L.M. Goeffroy, C.J. Keavney, M.M. Sanfacon, V.E. Haven, M.B. Spitzer, and K.A. Emery, "A 23.7 Percent Efficient One-Sun GaAs Solar Cell," *Proc. 19th IEEE Photovoltaic Spec. Conf.,* pp. 1492, 1493, 1987.

[10] H.C. Hamaker, C.W. Ford, J.G. Werthen, G.F. Virshup, N.R. Kaminar, D.L. King, and J.M. Gee, "26% Efficient Magnesium-Doped AlGaAs/GaAs Solar Concentrator Cells," *Appl. Phys. Lett.,* Vol. 47, pp. 762-764, 1985.

[11] M.S. Lundstrom, M.R. Melloch, R.F. Pierret, P.D. DeMoulin, D.P. Rancour, C.S. Kyono, and M.S. Carpenter, "Basic Studies of III-V High-Efficiency Cell Components," Technical Report, TR-EE 87-33, School of Electrical Engineering, Purdue University, Sept., 1987.

[12] Measurements and data courtesy of S.P. Tobin, Spire Corporation, private communication.

[13] P.D. DeMoulin, M.S. Lundstrom, and R.J. Schwartz, "GaAs Concentrator Cells: Design Options and Constraints," *Proc. 18th IEEE Photovoltaic Spec. Conf.,* pp. 321-326, 1985.

[14] R.P. Gale, John C.C. Fan, G.W. Turner, and R.L. Chapman, *Proc. 17th IEEE Photovoltaic Spec. Conf.,* p. 1422, 1984.

[15] H.C. Casey, Jr. and M.B. Panish, *Heterostructure Lasers,* Academic Press, New York, 1978.

[16] C.J. Hwang, *J. Appl. Phys.,* Vol. 42, pp. 4408-4413, 1971.

[17] R.J. Nelson and R.G. Sobers, *J. Appl. Phys.,* Vol. 49, pp. 6103-6108, 1978.

[18] C.J. Hwang, *Phys. Rev. B,* Vol. 6, pp. 1355-1359, 1972.

[19] A. Huag, *J. Phys. C,* Vol. 16, pp. 4159-4172, 1983.

[20] R.J. Schwartz, J.L. Gray, and G.B. Turner, "P-I-N Thin Film Silicon Hydrogen Alloy Solar Cells: Numerical Model Predictions," *Tech. Digest of the Int. PVSEC-1,* Kobe, Japan, pp. 123-126, 1984.

[21] R. Hulstrom, R. Bird, and C. Riordan, "Spectral Solar Irradiance Data Sets for Selected Terrestrial Conditions," *Solar Cells,* Vol. 15, pp. 365-391, 1985.

CHAPTER 2

EFFECTS OF BANDGAP NARROWING ON MBE-GROWN PP$^+$ BACK-SURFACE FIELDS

Preface

Previous work by our group has demonstrated that the interface recombination velocity at pp$^+$ homojunction back-surface fields is too high for effective minority carrier confinement [2]. The high recombination velocity can be explained in two different ways; it may be a consequence of bandgap narrowing in p$^+$ GaAs which effectively lowers the energy barrier for minority carrier electrons, or it may be the result of defects at the p—p$^+$ homojunction. This chapter describes an experiment conducted with MBE films grown in our laboratory. The results present strong evidence that the cause for the high interface recombination velocities observed in pp$^+$ homojunctions is bandgap narrowing effects in heavily doped p-GaAs.

2.1 INTRODUCTION

Strong heavy doping effects have recently been reported for Zn-doped GaAs grown by metal-organic chemical vapor deposition (MOCVD) [1]. In this chapter we present evidence that comparable effects of similar magnitude also occur in Be-doped GaAs grown by molecular beam epitaxy (MBE). The experiments utilized p—p$^+$ homojunction barriers commonly used to confine minority carriers in GaAs solar cells. Previous work showed that the effective recombination velocity associated with such a barrier was much too high for effective minority carrier confinement [2]. Significantly better performance has been achieved by replacing the isotype homojunction barrier with an isotype heterojunction barrier in n-p GaAs solar cells [3]. The work we report herein suggests that the poor confinement of minority carriers by these homojunction barriers is due to an effective reduction in the bandgap associated with heavy Be-doping.

A successive etch technique [4] was employed to estimate the recombination velocity of a p—p$^+$ homojunction barrier. The barrier recombination velocity was found to be about 6×10^4 cm/sec, and it increased as the width of the p$^+$—barrier layer decreased. Recombination through defects at the p—p$^+$ interface cannot explain these results, but the occurrence of bandgap narrowing effects [5] in p$^+$—GaAs can. The amount of bandgap narrowing deduced from the measurements is consistent with that measured for Zn-doped GaAs grown by MOCVD [1]. These results demonstrate that bandgap narrowing effects significantly influence the electrical performance of devices containing p$^+$—GaAs regions. They underscore the need to characterize such effects for Be-doped GaAs grown by MBE.

2.2 EXPERIMENTAL TECHNIQUE

The epitaxial layer structure for the solar cells used in this study is shown in Fig. 2.1. The films were grown in a Perkin-Elmer PHI-400 MBE system. The starting substrate was cleaved from a (100) oriented, n-type GaAs wafer, and the thicknesses of the epitaxial layers were determined by counting oscillations in the intensity of the reflection high energy electron diffraction pattern. Silicon was used as the n-type dopant and beryllium

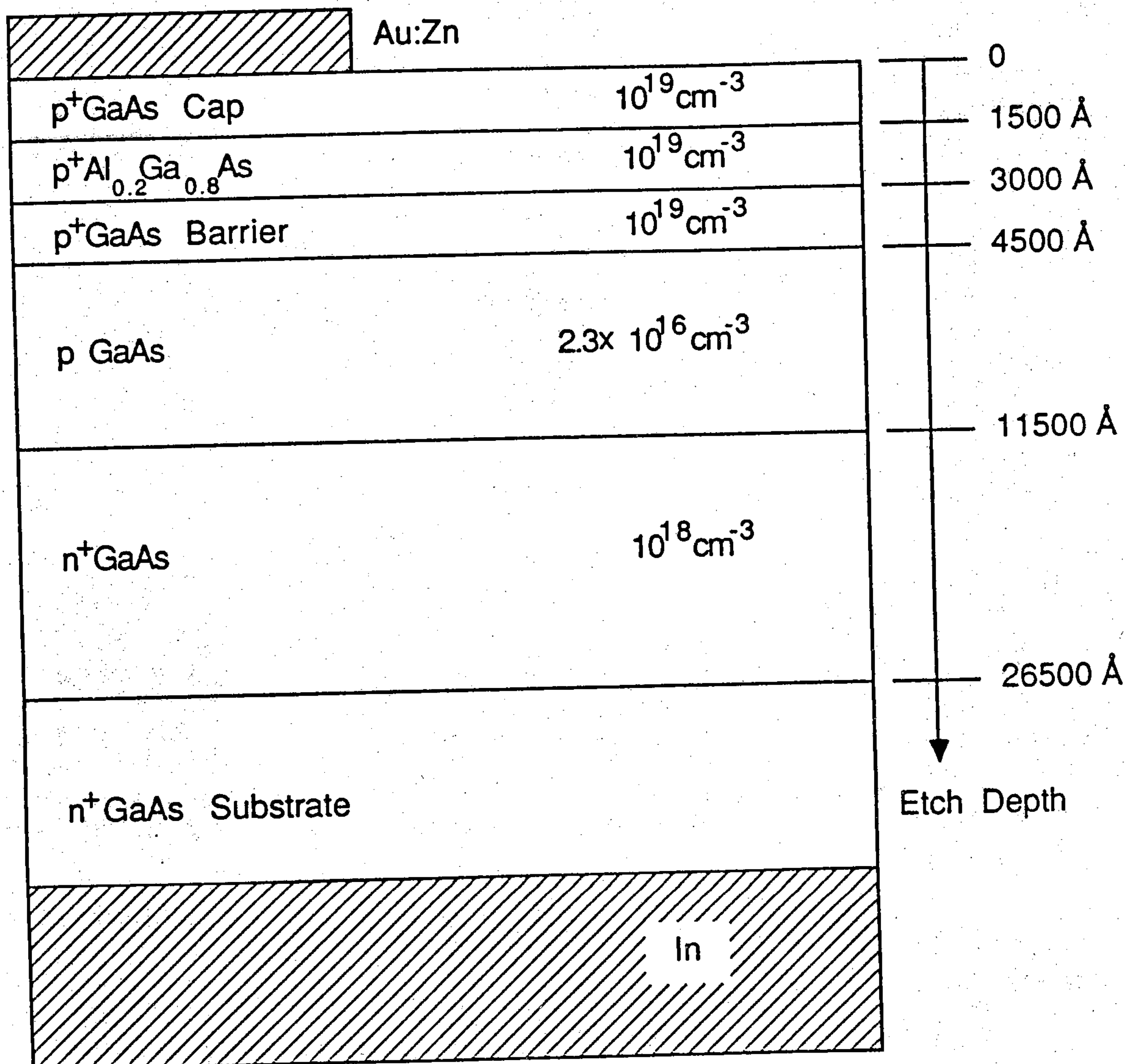

Fig. 2.1 Epitaxial layer structure of the solar cells used in this study.

as the p-type dopant. Solar cells of dimension 0.1 cm by 0.1 cm were defined by photolithography and subsequent wet etching. The p-type contact was a Au:Zn metal finger pattern which covered 18.4% of the cell area and formed a non-alloyed contact to the p^+–GaAs cap layer. The back contact metal was indium. The doping density of the p-layer was measured as 2.3×10^{16} cm^{-3} by capacitance versus voltage profiling. Doping densities of the other layers were estimated from the growth rate of the film and the temperature of the dopant oven.

The completed cells were characterized by current versus voltage (I-V) measurements performed with a Hewlett-Packard 4145A semiconductor parameter analyzer. All I-V measurements were performed in the dark at about 23.3 °C. The measured current density versus applied voltage can be described by

$$J = J_{01} \left(e^{qV/kT} - 1\right) + J_{02} \left(e^{qV/2kT} - 1\right), \tag{2.1}$$

where J_{01} and J_{02} are the saturation current densities associated with carrier recombination in the quasi-neutral and space-charge regions, respectively. The dark I-V characteristics were fitted to Eq. (1) to determine the two saturation current densities.

A successive etch technique was used to characterize the electron injection current [4]. The metal grid pattern was protected with photoresist, and the exposed semiconductor was removed in a series of short etches. Each etch was 20 seconds long in a solution of [$8H_2SO_4$:$4H_2O_2$:$400H_2O$] at 26 °C and removed 375 Å of material as measured by step profiling. After each etch, the forward-biased dark I-V characteristic was measured.

2.3 ANALYSIS AND DISCUSSION

The dark I-V characteristic was measured after each etch step, and the resulting $n=1$ saturation current density, J_{01}, is plotted in Fig. 2.2. J_{01} was roughly constant until the $Al_{0.2}Ga_{0.8}As$ layer was removed; it then increased as the p^+–GaAs barrier layer was thinned. When the p^+–barrier layer was completely removed, J_{01} increased sharply. This result clearly demonstrates that the heterojunction barrier is more effective than the homojunction barrier in minority carrier confinement.

In a p–n^+ GaAs diode, the major component of J_{01} is due to electron injection in the p–GaAs and is given by

$$J_{01e} = \frac{qn_{io}^2}{N_A} \left[\frac{S + (D_n/L_n)\tanh(W_p/L_n)}{1 + S\,(L_n/D_n)\tanh(W_p/L_n)}\right] \tag{2.2}$$

where D_n and L_n are the minority carrier electron diffusion coefficient and length, respectively, n_{io} is the intrinsic carrier concentration of lightly-doped GaAs, W_p is the width and S is the surface recombination velocity of the lightly-doped p-layer. If the p-layer is thin ($W_p \ll L_n$) and the surface is unpassivated ($S \gg W_p/\tau_n$), then Eq. (2.2) can be simplified as

$$J_{01e} = \frac{qn_{io}^2 D_n}{N_A W_p} \frac{S}{S + D_n/W_p} . \tag{2.3}$$

Eq. (2.3) should describe the electron injection current after the p^+–GaAs cap, the p^+–$Al_{0.2}Ga_{0.8}As$, and the p^+–GaAs barrier layers have been removed.

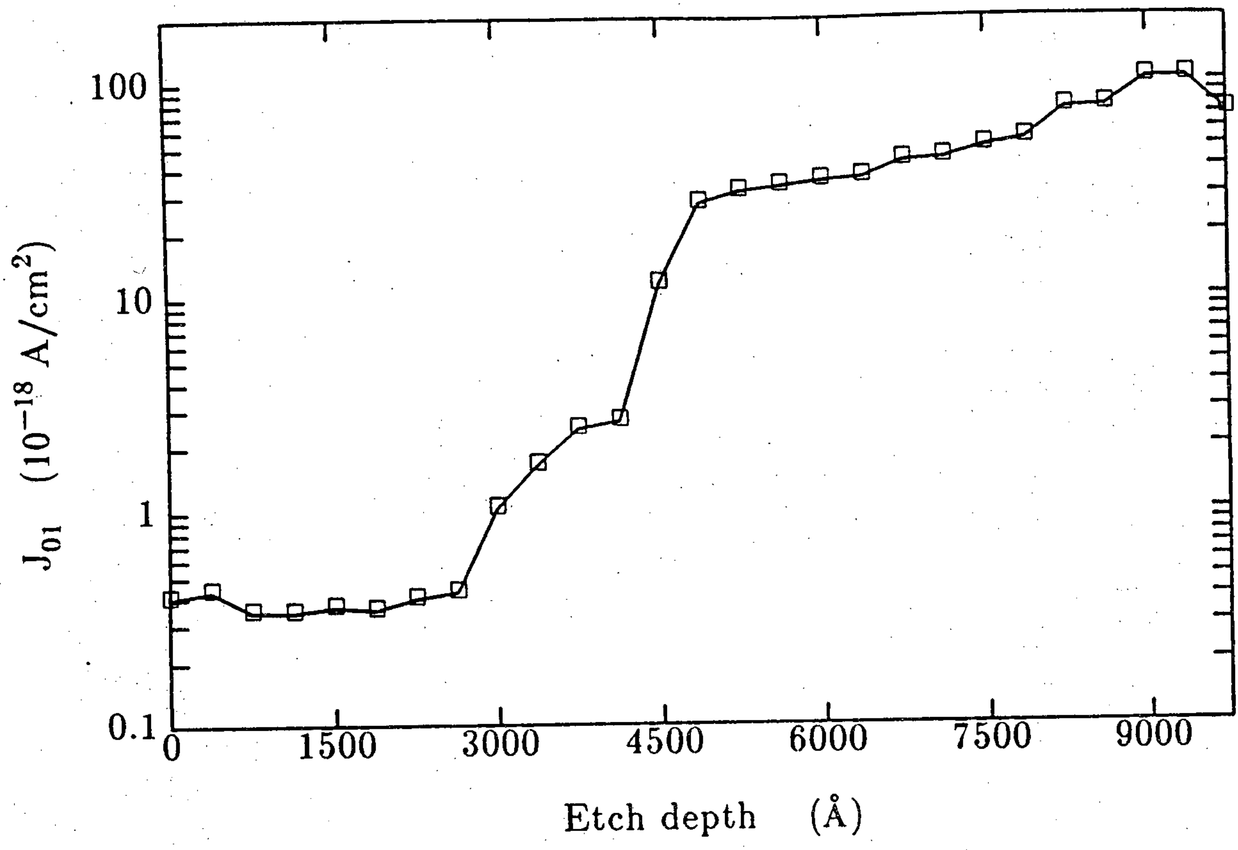

Fig. 2.2 The n=1 saturation current density, J_{01}, extracted rom the measured dark current versus voltage characteristic after each etch.

Since the measured n=1 current component increased by more than a factor of 30 after the top three layers were removed, the measured J_{01} can be equated to Eq. (2.3). The width of the p-GaAs layer varied with time according to $W_p(t) = W_{p0} - Rt$, where W_{p0} is the width of the lightly-doped thin p-layer at $t = 0$, and R is the etch rate. Eq. (2.3) can then be rearranged as

$$J_{01}^{-1} \simeq J_{01e}^{-1} = \left[\frac{N_A W_{p0}}{qn_{io}^2 D_n} + \frac{N_A}{qn_{io}^2 S}\right] - \left[\frac{N_A R}{qn_{io}^2 D_n}\right] t . \quad (2.4)$$

Fig. 3 shows that a plot of J_{01}^{-1} versus etch time was linear with a slope of $N_A R/qn_{io}^2 D_n$, from which the product, $n_{io}^2 D_n$ at 23.3 °C, was determined to be 2.9×10^{14} cm^{-4} sec^{-1}. From the intercept, a surface recombination velocity of 9.4×10^6 cm/sec was deduced.

The measured surface recombination velocity agrees well with the value expected for a bare GaAs surface [6]. From the measured $n_{io}^2 D_n$ product and the data of Blakemore for n_{io} [7], a minority carrier electron diffusion coefficient of $D_n = 123$ cm^2/sec was deduced. This value corresponds to a minority carrier electron mobility of 4760 cm^2/V–sec at 300K and is 25% lower than the mobility of minority carrier electrons in uncompensated GaAs as predicted by Walukiewicz *et al.* [8]. Low minority carrier mobilities have also been reported in p–GaAs doped much heavier than that employed here [9,10].

Consider next the situation when the p^+–GaAs barrier layer was present. A theoretical expression relating the barrier recombination velocity, S_{pp^+}, to the structural parameters of the barrier, valid for both homojunction and heterojunction barriers, has been given by DeMoulin *et al.* [11] as

$$S_{pp^+} = \frac{D_n^+ N_A^-}{L_n^+ N_A^+} \frac{n_{ie}^2}{n_{io}^2} \coth(W_p^+/L_n^+) , \quad (2.5)$$

where the '–' and '+' superscripts refer to the lightly- and heavily-doped sides of the junction, respectively, and n_{ie} is the effective intrinsic carrier concentration of the heavily-doped side that accounts for the effective reduction in bandgap associated with heavy impurity doping and for the influence of Fermi-Dirac statistics. In this case, since the p^+–GaAs barrier layer was only 0.15 μm thick, the assumption $W_p^+ \ll L_n^+$ is valid, so Eq. (2.5) can be simplified as

$$S_{pp^+} = \frac{D_n^+ N_A^-}{W_p^+ N_A^+} \frac{n_{ie}^2}{n_{io}^2} . \quad (2.6)$$

Thus S_{pp^+} is expected to be inversely proportional to W_p^+.

S_{pp^+} can be related to the measured n=1 component of the dark current; since $W_p \ll L_n$ and S_{pp^+} may be comparable to W_p/τ_n, Eq. (2.2) is simplified as

$$J_{01e} = \frac{qn_{io}^2}{N_A} \frac{S_{pp^+} + W_p/\tau_n}{1 + (W_p/D_n) S_{pp^+}} , \quad (2.7)$$

which can be solved for

$$S_{pp^+} = \frac{1 - \dfrac{qn_{io}^2}{N_A J_{01e}} \dfrac{W_p}{\tau_n}}{\dfrac{qn_{io}^2}{N_A J_{01e}} - \dfrac{W_p}{D_n}} . \quad (2.8)$$

Since J_{01e} is very nearly the measured J_{01}, and D_n has been determined as described

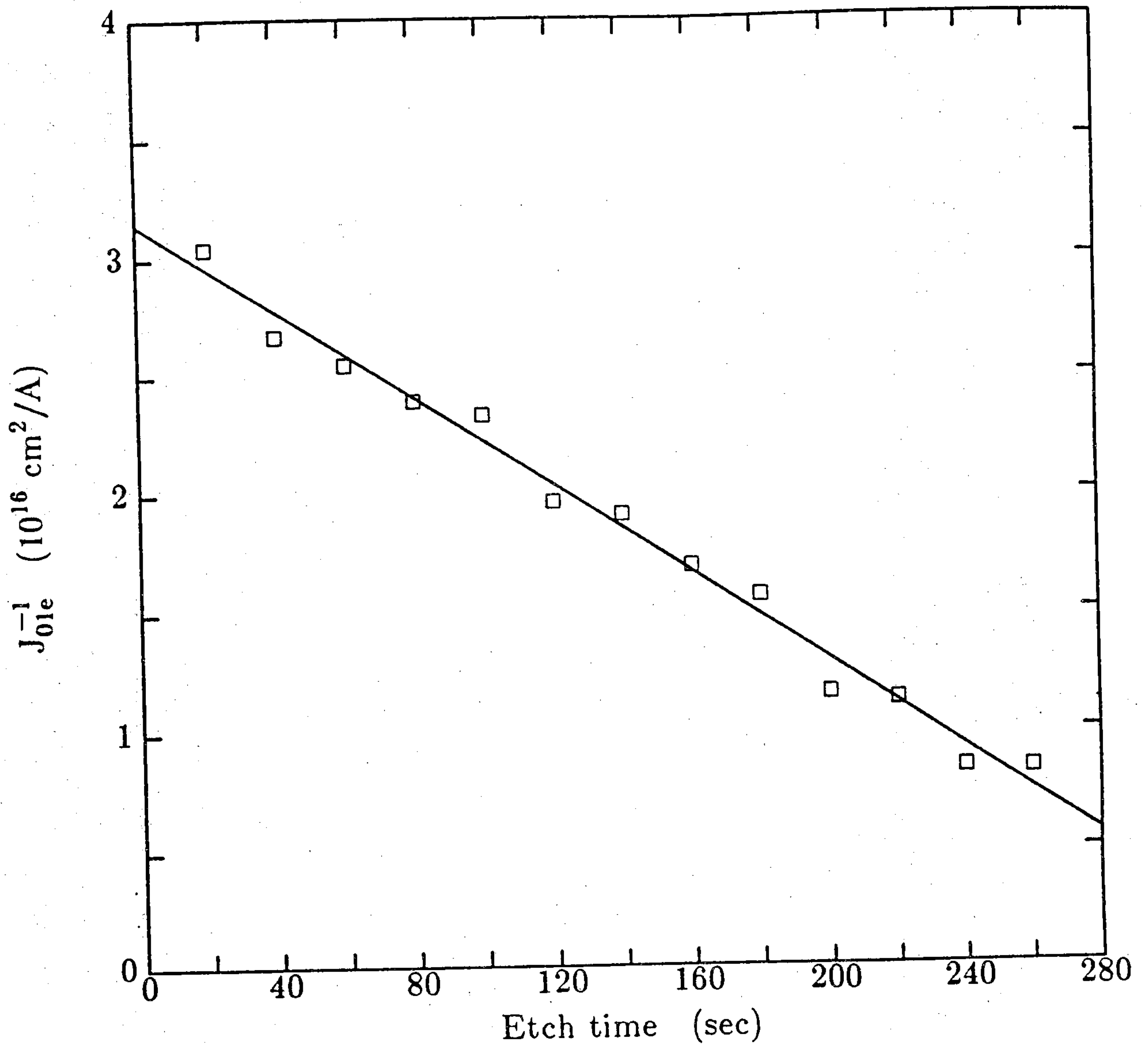

Fig. 2.3 Plot of J_{01e}^{-1} versus etch time. From the slope, $N_A R/qn_{io}^2 D_n$, the minority carrier diffusion coefficient, D_n was deduced.

above, with an appropriate τ_n, Eq. (2.8) can be employed to estimate S_{pp^+}; values of S_{pp^+} versus etch depth were calculated for a few different values of τ_n. By plotting S_{pp^+} versus $1/W_p^+$ (see Fig. 2.4), it is found that the relationship was linear, and that a τ_n of 1.1 nsec caused the straight line to pass through the origin, thus satisfying Eq. (2.6). This implies that a minority carrier electron in our MBE-grown material of doping $N_A=2.3\times10^{16}$ cm^{-3} has a lifetime of 1.1 nsec. Taking the square root of the product $D_n\tau_n$, the minority carrier electron diffusion length, L_n, was determined to be 3.7 μm, thus the assumption $W_p \ll L_n$ used in Eq. (2.3) and Eq. (2.7) is valid. Using Eq. (2.6) and the slope of the straight line that passes through the origin in Fig. 2.4, $n_{ie}^2D_n^+$ was determined to be 1.8×10^{15} cm^{-4} sec^{-1}, which agrees with the data measured by Klausmeier-Brown, *et al.* [1]. They found $n_{ie}^2D_n^+=1.8\times10^{15}$ cm^{-4} sec^{-1} for MOCVD-grown GaAs, Zn-doped at 1×10^{19} cm^{-3}. They reported that the product $n_{ie}^2D_n^+$ was affected by bandgap narrowing through an increase in n_{ie}. This implies that the effective bandgap shrinkage in Be-doped GaAs grown by MBE is comparable to that observed for Zn-doped GaAs grown by MOCVD.

A plot of measured S_{pp^+} versus etch depth is displayed in Fig. 2.5, which shows that S_{pp^+} is about 6×10^4 cm/sec and that it increases as the thickness of the p^+–layer decreases. Since S_{pp^+} was found to depend on the thickness of the p^+–layer, it cannot be controlled by recombination at the doping junction but must be related to the properties of the barrier. Assuming no bandgap narrowing effects, theoretical values of S_{pp^+} were calculated using Eq. (2.6), in which n_{ie} equals n_{io} from Blakemore [7] corrected for hole degeneracy, and using D_n given by Walukiewicz *et al.* for uncompensated p-GaAs [8]. Fig. 2.5 compares the theoretical estimate of S_{pp^+} with the measured value computed from Eq. (2.8). The figure shows that when bandgap narrowing effects were not considered, the theoretical estimate of S_{pp^+} was about 10 times lower than the value deduced from the measurements. The results clearly suggest that the high barrier recombination velocity is the result of an effective narrowing of the bandgap of p^+–GaAs.

Lower values of S_{pp^+} may be achieved by making the p^+–GaAs barrier layer thicker. Suppose the p^+–barrier layer is so thick that W_p^+ is several times greater than L_n^+, then Eq. (2.5) can be simplified as

$$S_{pp^+} = \frac{D_n^+N_A^-}{L_n^+N_A^+}\frac{n_{ie}^2}{n_{io}^2} . \tag{2.9}$$

Using the product $n_{ie}^2D_n^+$ determined above, our doping densities, and n_{io} from Blakemore [7], S_{pp^+} was estimated to be $\lesssim 10^4$ cm/sec provided that L_n^+ is greater than 0.82 μm. But because it is very difficult to determine the value of L_n^+, the possibility of achieving such a low value of S_{pp^+} by increasing the thickness is uncertain.

IV. CONCLUSIONS

In this chapter we employed a successive etch technique to study electron injection currents in GaAs p–n^+ diodes grown by molecular beam epitaxy. The results show that the effective recombination velocity of the p–p^+ homojunction barriers in these diodes is about 6×10^4 cm/sec. Analysis of these results strongly suggests that the high barrier recombination velocity is a consequence of an effective reduction in bandgap caused by heavy Be-doping. These effects appear to be comparable in magnitude to those reported for Zn-doped GaAs grown by metal-organic chemical vapor deposition [1]. The results also show that minority carrier electrons, at 300K, have a mobility of 4760 cm^2/V-sec at a hole concentration of 2.3×10^{16} cm^{-3}, thus confirming that the minority carrier electron mobility in this moderately doped p–GaAs is lower than the majority carrier mobility in

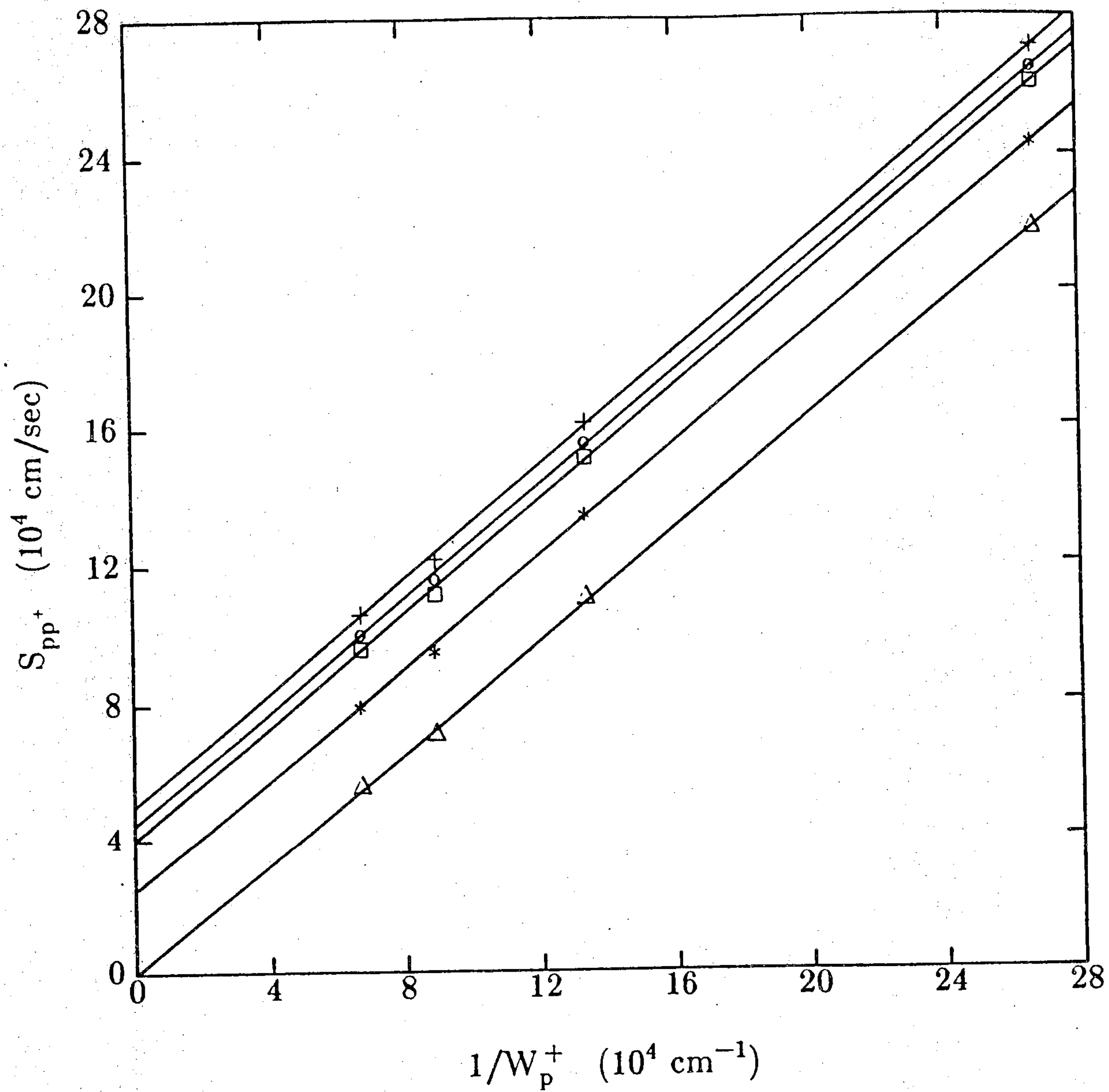

Fig. 2.4 Barrier recombination velocity S_{pp^+} versus thickness of the p^+–GaAs barrier layer plotted, from top to bottom, for minority carrier electron lifetimes of 100 nsec, 10 nsec, 5 nsec, 2 nsec and 1.1 nsec, respectively.

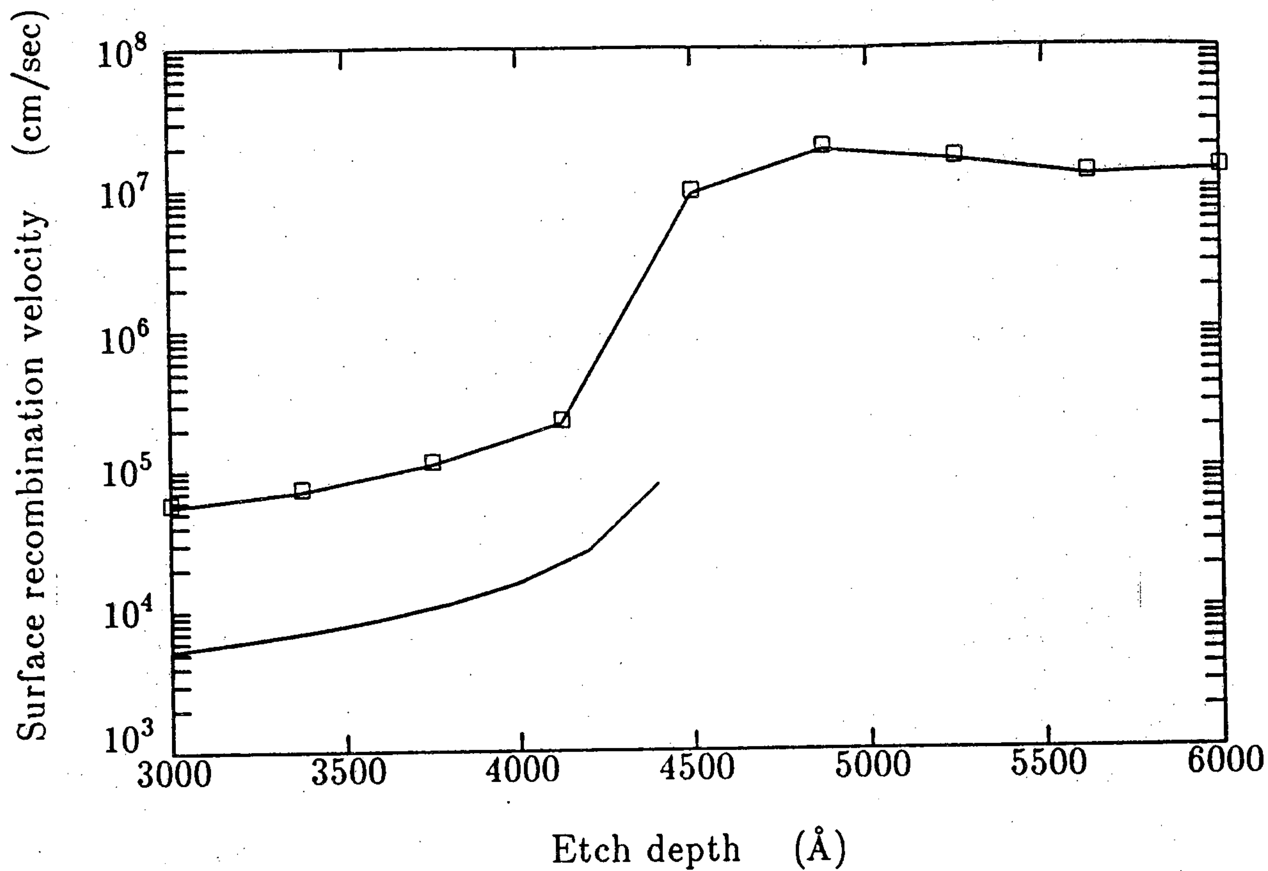

Fig. 2.5 Surface recombination velocity versus etch depth starting from the p^+–GaAs barrier layer. Top curve represents measured data. Bottom curve represents theoretical data without bandgap narrowing effects.

comparably doped, uncompensated n—GaAs.

The results reported in this paper demonstrate that heavy doping effects significantly influence the performance of GaAs bipolar devices. This work helps to explain the substantial increase in solar cell performance that was observed when a homojunction p—p^+ barrier was replaced with an isotype heterojunction barrier.[3] We conclude that heterojunction barriers are essential for maximizing the efficiency of n—p GaAs solar cells.

CHAPTER 2 REFERENCES

[1] M. E. Klausmeier-Brown, M. S. Lundstrom, and M. R. Melloch, to appear in Appl. Phys. Lett. **52,** (1988).

[2] M. E. Klausmeier-Brown, C. S. Kyono, D. P. Rancour, M. S. Carpenter, M. R. Melloch, M. S. Lundstrom, and R. F. Pierret, Conf. Rec. 19th IEEE Photovoltaic Specialists Conference, 1174 (1987).

[3] R. P. Gale, J. C. C. Fan, G. W. Turner, and R. L. Chapman, Conf. Rec. 17th IEEE Photovoltaic Specialists Conference, 1422 (1984).

[4] M. E. Klausmeier-Brown, C. S. Kyono, P. D. DeMoulin, S. P. Tobin, M. S. Lundstrom, and M. R. Melloch, to appear in IEEE Trans. Electron Devices **35,** (1988).

[5] J. Wagner, and J. A. del Alamo, J. Appl. Phys. **63,** 425 (1988).

[6] R. P. Leon, Conf. Rec. 19th IEEE Photovoltaic Specialists Conference, 808 (1987).

[7] J. S. Blakemore, J. Appl. Phys. **53,** R123 (1982).

[8] W. Walukiewicz, J. Lagowski, L. Jastrzebski, and H. C. Gatos, J. Appl. Phys. **50,** 5040 (1979).

[9] R. K. Ahrenkiel, D. J. Dunlavy, D. Greenberg, and J. Schlupmann, Appl. Phys. Lett. **51,** 776 (1987).

[10] M. I. Nathan, W. P. Dumke, K. Wrenner, S. Tiwari, S. L. Wright, and K. A. Jenkins, Appl. Phys. Lett. **52,** 654 (1988).

[11] P. D. DeMoulin, M. S. Lundstrom, and R. J. Schwartz, Solar Cells **20,** 229 (1987).

CHAPTER 3

EDGE EFFECTS IN MBE-GROWN GaAs DIODES

Preface

This chapter is a portion of a Ph.D. thesis by David P. Rancour. The thesis, "Investigation of GaAs Solar Cell Structures Using Deep Level Transient Spectroscopy," is concerned with using DLTS studies to explore recombination mechanisms in GaAs-based solar cells. One result of this work, the development of a DLTS technique tailored for solar cell diagnostics, was described in last year's annual report (see the appendices for a preprint of this work). One of the significant findings was that edge recombination tends to dominate solar cell performance which makes it difficult to correlate DLTS studies with solar cell performance. This chapter describes that work on edge effects in GaAs diodes. The work described herein was the stimulus for the research on perimeter recombination in MOCVD-grown solar cells which is described in the reprints in the appendix. It also motivated our research on chemical passivation of GaAs surfaces which is the subject of the following chapter.

3.1. INTRODUCTION

One can, in principle, separate the perimeter and bulk components of the recombination current by means of a plot of J_{02} versus perimeter-to-area ratio. The total reverse saturation recombination current is described by:

$$I_{02} = I_{02Bulk} + I_{02Surface}$$

$$= \frac{qn_i W_{eff} A}{\tau_{SCR}} + S_{SCR} L_s q n_i P \qquad (3.1)$$

Examining Eq.(3.1), it is obvious that a plot of J_{02} (i.e. I_{02}/A) versus P/A should be linear, with a J_{02} axis intercept that is proportional to W_{eff}/τ_{SCR} and a slope that is proportional to $S_{SCR}L_s$. Devices that are bulk dominated will yield J_{02} versus P/A plots that are essentially horizontal lines, whereas plots for surface dominated devices will rise steeply with increasing P/A. At any rate, the parameters characterizing both SRH and perimeter surface recombination can, in principle, be measured by determining the J_{02} values for a set of diodes that have different perimeter-to-area ratios. This was the motivation behind the experiment to be described in the following paragraphs.

3.2 I-V MEASUREMENTS (P/A VARIABLE)

Growth and Device Information

The starting substrate for the devices to be discussed was n^+ (Si:2×10^{18} cm^{-3}) GaAs. A cross section of the MBE film layers is shown in Figure 3.1. The MBE film structure consisted of a 2.0μm n^+-GaAs buffer layer, a 2.0μm n-GaAs base, a 0.5μm p-GaAs emitter, a 500Å P-$Al_{0.9}Ga_{0.1}As$ window, and a 0.3μm p^+-GaAs cap. (This device structure was identical to the MOCVD GaAs solar cell films fabricated by the SPIRE corporation.) Different size mesa diodes were fabricated and the mesas themselves patterned with metal rectangles/squares of differing sizes. The metalization pattern for diode 4 of the "SPIRE clone" film is shown in Figure 3.2. The 1000μm $\times$ 1000μm mesa diode was patterned into two 150μm $\times$ 940μm, two 75μm $\times$ 940μm, two 40μm $\times$ 940μm,

and two $30\mu m \times 940\mu m$ gold rectangles. The metalization served both as a top contact and as a mask for subsequent etching steps.

Experimental Data

The J-V characteristics for the as-fabricated mesas were measured at room temperature (300.1K-301.6K), and J_{02} was extracted by curve fitting. The representative dark J-V characteristics derived from diode 4 of the SPIRE clone film are shown in Figure 3.3. Figure 3.3 reveals shunt leakage current at low biases, a 2kT current region at moderate biases, and series resistance effects at high biases. Diode 4 had $J_{02} = 5.2 \times 10^{-10}$ (A/cm^2) and P/A = 40 (cm^{-1}).

With the gold metalization serving as a mask, the mesas were next re-etched. The etch used was H_2SO_4:H_2O_2:H_2O 1:8:40, which was identical to that used to form the original mesas. After etching, the shunt leakage current became prominent in all devices. For $\sim$ 80% of the devices the diode ideality factor, n (from $I \propto e^{qV_A/nkT}$), never fell below about 2.5 to 3. For the remaining 20%, J_{02} was extracted by curve fitting. The dark J-V characteristic for the first $150\mu m \times 940\mu m$ mesa of diode 4 is shown in Figure 3.4. Also shown for comparison is the J-V characteristic of Figure 3.3. It is evident that the *leakage* current increased, as did J_{02}. Table 3.1 lists the J_{02} values and perimeter-to-area ratios for the re-etched mesa of diode 4.

Diode #	J_{02} $\times 10^{-10}$ (A/cm^2)	P/A (cm^{-1})	Area $\times 10^{-4}$ (cm^2)
4.4	230.	687.9	2.82
4.3	164.	521.3	3.76
4.7	242.	521.3	3.76
4.2	69.4	287.9	7.05
4.6	117.	287.9	7.05
4.1	30.5	154.6	14.10
4.5	53.9	154.6	14.10

Table 3.1. J_{02} values and P/A ratios for re-etched mesa of diode 4 of the SPIRE clone film.

The J_{02} versus P/A data is plotted in Figure 3.5, and although there is some scatter, J_{02} exhibits a roughly linear dependence on P/A. The implication is that surface recombination is significant for these devices. Note that the J_{02} axis intercept of the least squares line is negative. This may be due to experimental error or to the variation, from diode to diode, of $S_{SCR}L_s$ and/or τ_{SCR}. Diode 4.1 is physically adjacent to diode 4.2, which is in turn adjacent to diode 4.3, etc.. The fact that the data points for diodes 4.1-4.4 appear to fall on one line while the data points for diodes 4.5-4.7 fall on another line seems to indicate that $S_{SCR}L_s$ and/or $1/\tau_{SCR}$ is indeed increasing from diode 4.1 to 4.7.

The J_{02} versus P/A plot revealed that perimeter surface recombination dominated bulk SCR recombination for these devices. J_{02} should therefore be highly sensitive to the

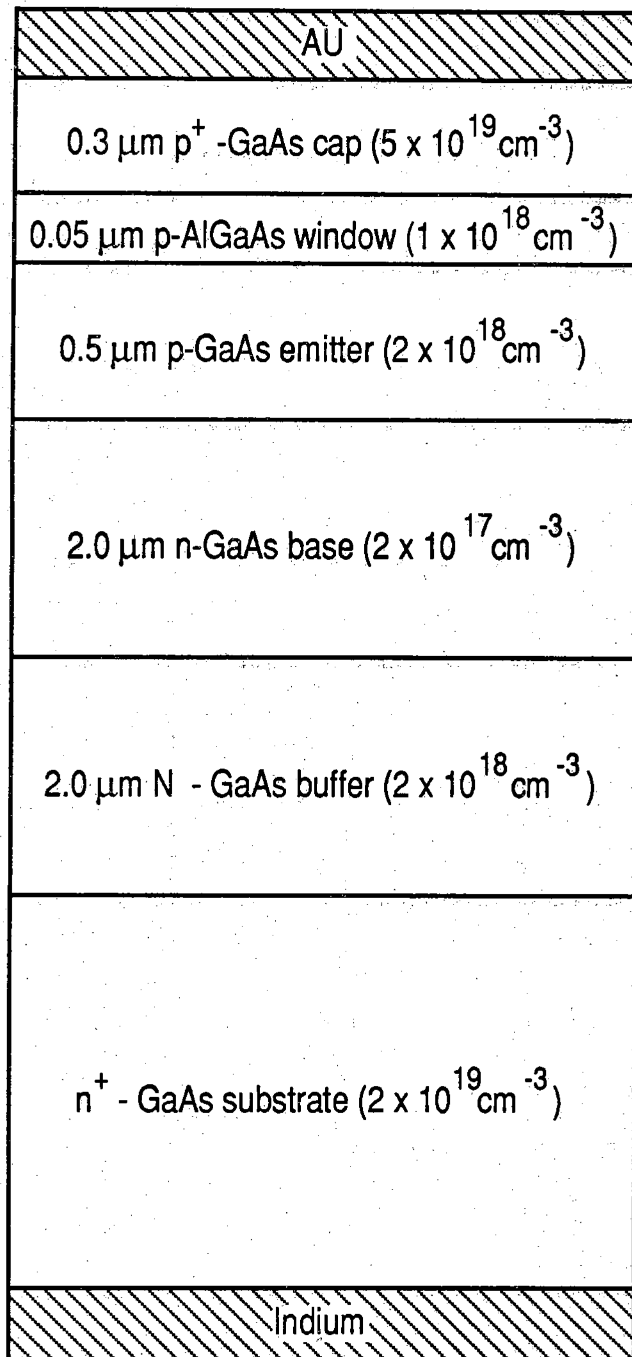

Figure 3.1. A cross section of the MBE layer structure for the "SPIRE clone".

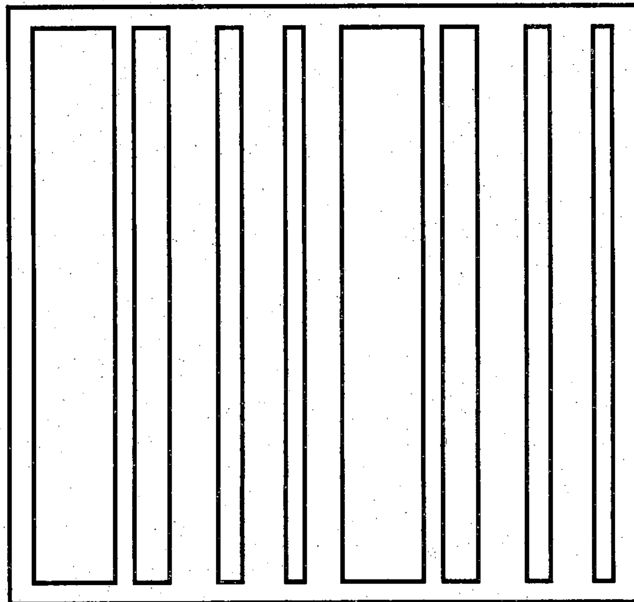

Figure 3.2. Metalization pattern for diode 4 of the "SPIRE clone" film.

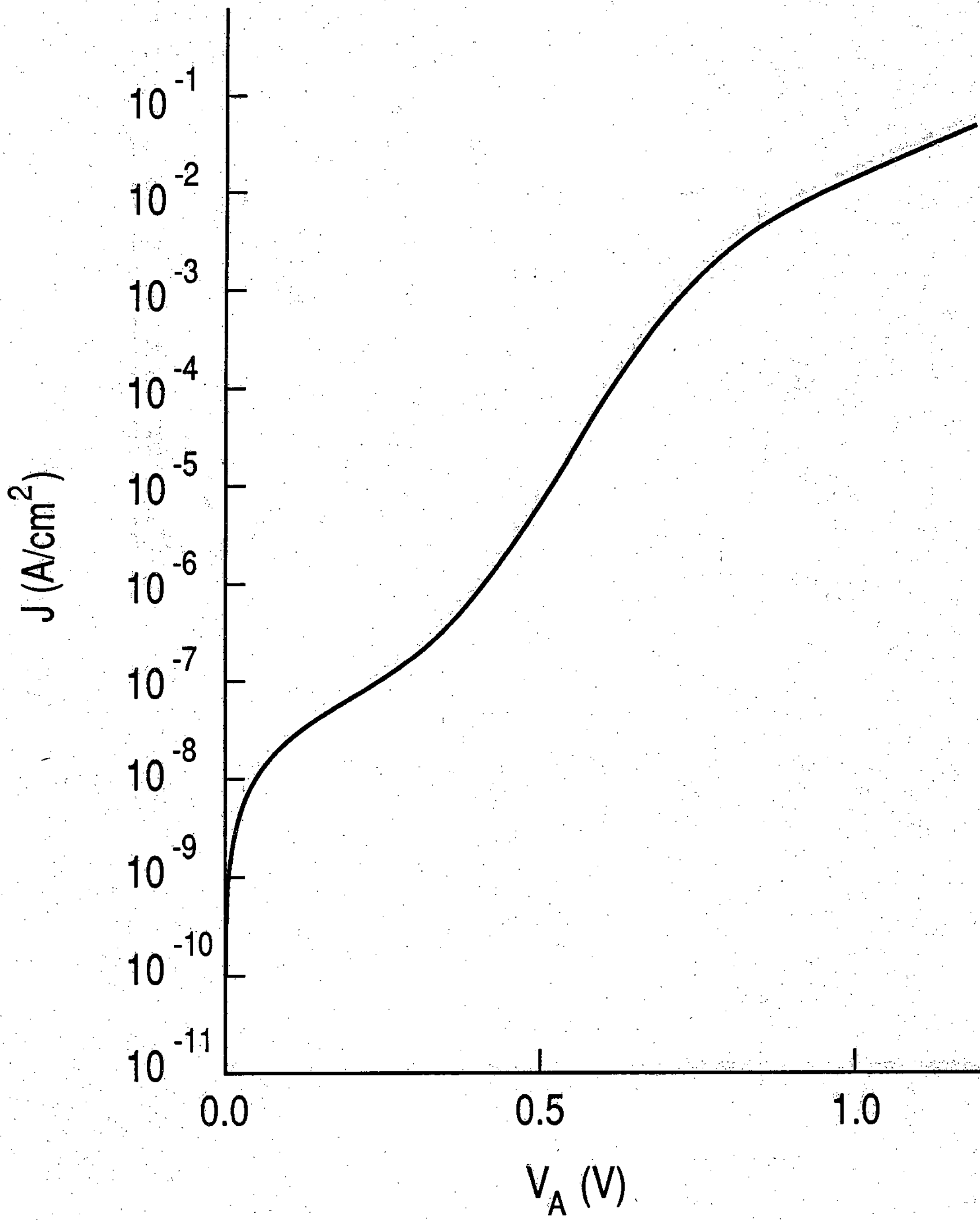

Figure 3.3. Dark J-V characteristics for diode 4 of the SPIRE clone film.

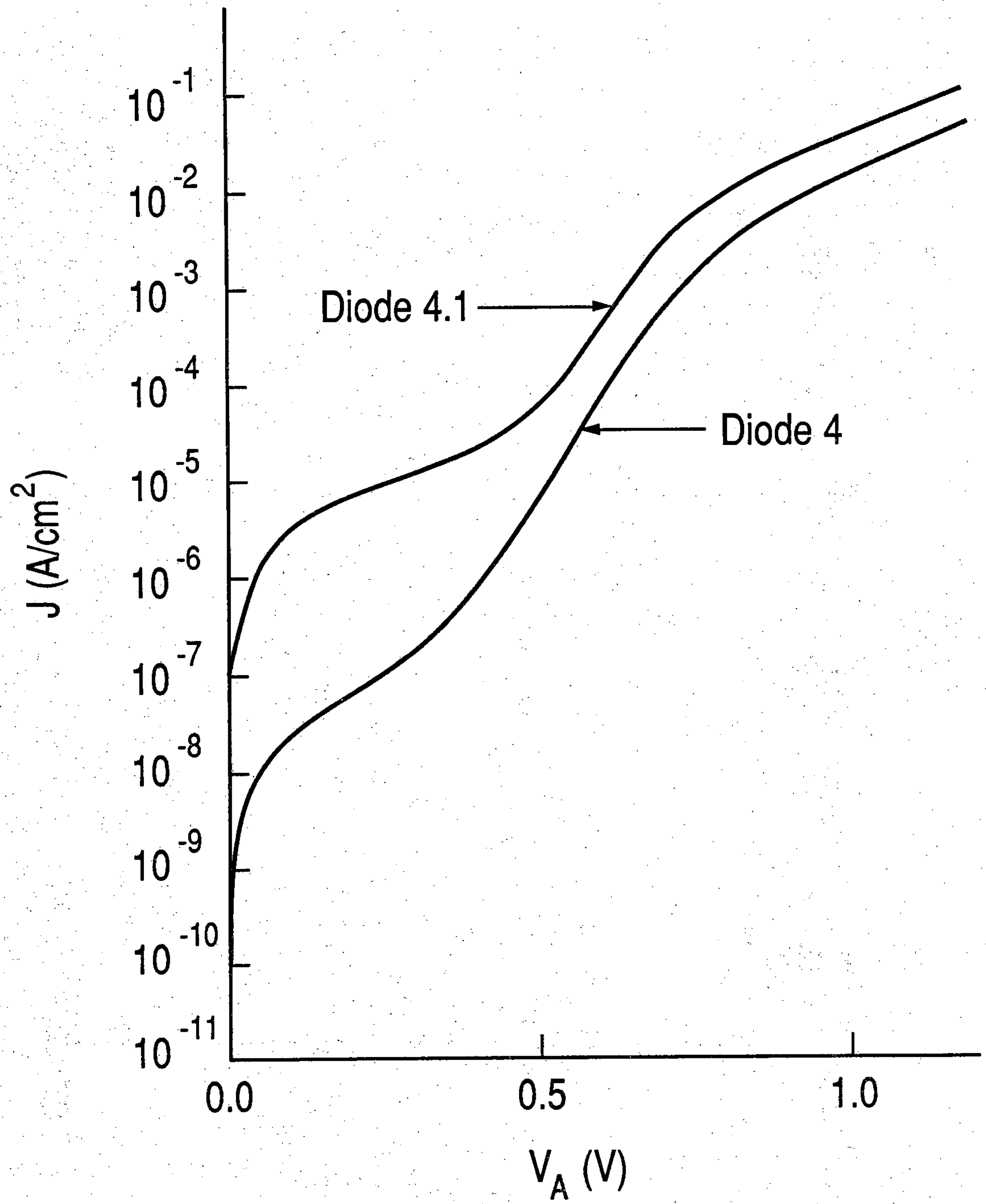

Figure 3.4. Dark J-V characteristics for diode 4.1 of the SPIRE clone film. The dark J-V for the as fabricated mesa are also shown.

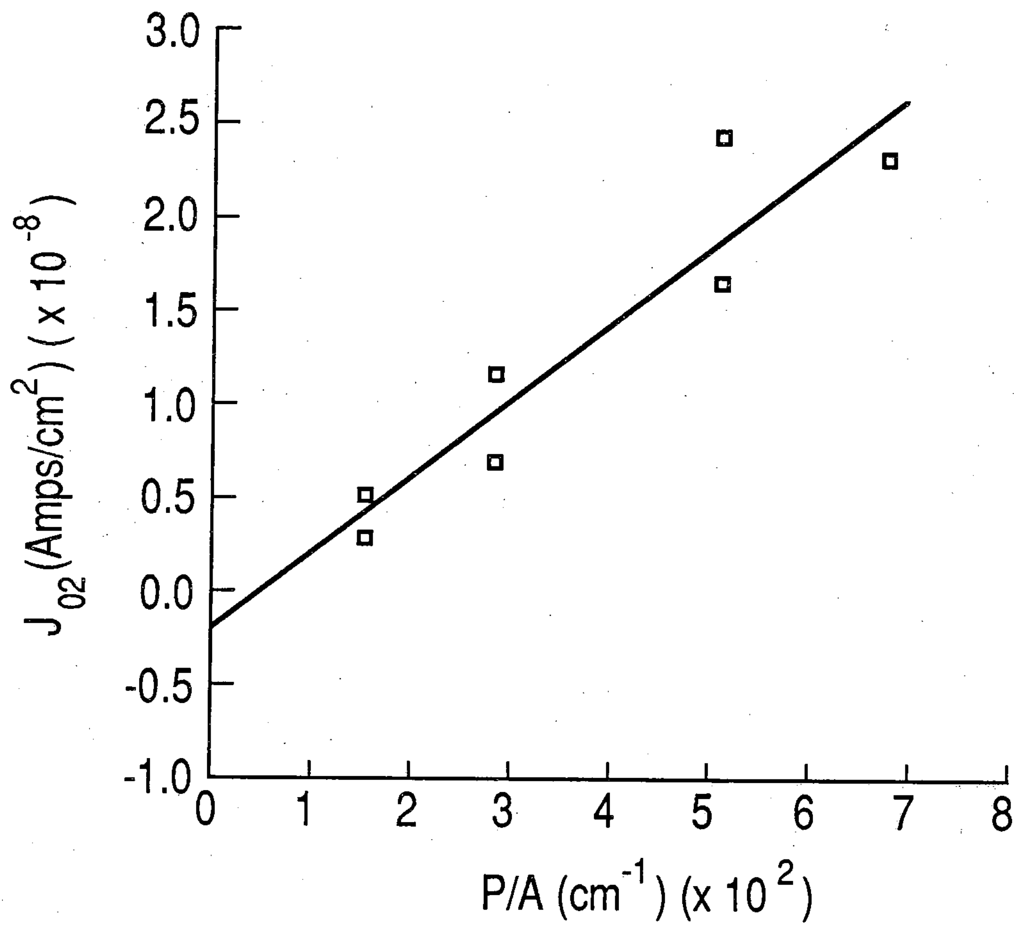

Figure 3.5. J_{02} versus P/A for diodes 4.1-4.7 of the SPIRE clone film.

condition of the surface. With this in mind, an effort was made to perturb the surface: the surface oxides of diode 4 were removed by dipping the diode in concentrated HCl and, after rinsing in deionized water, a new surface oxide was grown by dipping the sample in H_2O_2. The I-V characteristics were then remeasured. The treatment resulted in over an order of magnitude reduction of *shunt leakage* current. However, the *recombination* current increased by 5 to 7 times. The dark J-V characteristic for the first $150\mu m \times 940\mu m$ mesa of diode 4 is shown in Figure 3.6. Also shown for comparison are the J-V characteristics of Figure 3.4. Table 3.2 lists the post dip J_{02} values and perimeter-to-area ratios for diode 4.

Cell #	J_{02} $\times 10^{-10}$ (A/cm^2)	P/A (cm^{-1})	Area $\times 10^{-4}$ (cm^2)
4.4	1,180.	687.9	2.82
4.3	886.	521.3	3.76
4.7	1,050.	521.3	3.76
4.2	409.	287.9	7.05
4.6	480.	287.9	7.05
4.1	207.	154.6	14.10
4.5	246.	154.6	14.10

Table 3.2. J_{02} values and P/A ratios for diode 4 of the SPIRE clone film after treatment with HCl-H_2O_2.

The J_{02} versus P/A data is plotted in Figure 3.7 along with a replot of the pretreatment data from Figure 3.5. The new data is again approximately linear, and rises even more steeply than before, indicating that the perimeter recombination current component has increased. One can only conclude that surface recombination current, occurring around the p-n junction perimeter, totally dominated the 2kT current for the investigated mesa diodes.

3.3 I-V MEASUREMENTS (T VARIABLE)

In the experiments described above, whenever the perimeter *recombination* current was perturbed, the *shunt leakage* current was also affected. This implied that the shunt leakage current was located primarily around the junction perimeter, rather than in the volume of the SCR. In contrast Fischer and coworkers [1], who investigated shunt leakage current by means of I-V measurements taken over a range of different temperatures, concluded that the shunt leakage current was due to a bulk tunneling mechanism. However, in light of the data presented in section 3.2 above, it seems likely that the leakage current observed by Fischer et al. was also an edge effect. To test this hypothesis, their experiment was duplicated (with the addition of an HCl-H_2O_2 treatment step) using a diode that had a relatively large leakage current component. The results of this experiment are reported below.

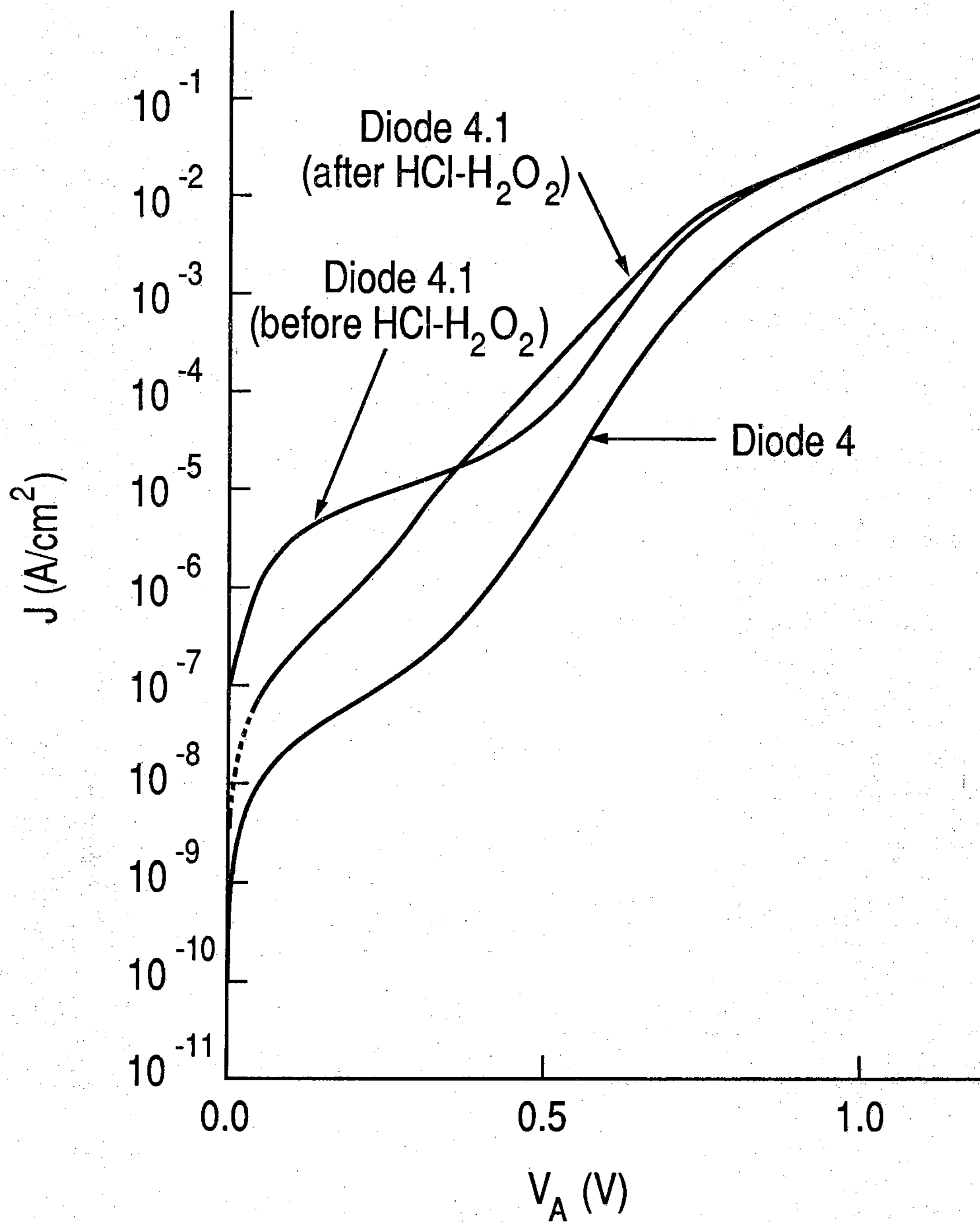

Figure 3.6. Dark J-V characteristics for diode 4.1 of the SPIRE clone film after treatment with HCl-H_2O_2. Also shown are the J-V characteristics for diode 4.1 prior to the treatment, and the J-V characteristics for the original $1000\mu m \times 1000\mu m$ mesa.

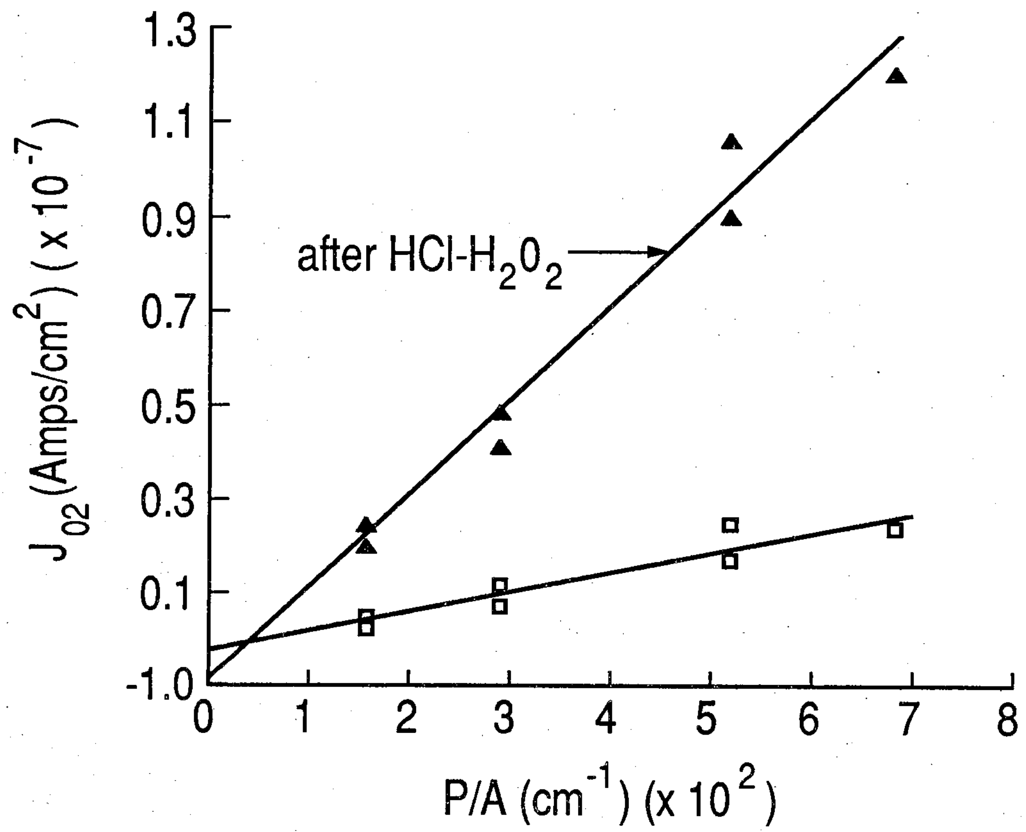

Figure 3.7. J_{02} versus P/A for diodes 4.1-4.7 of the SPIRE clone film after treatment with HCl-H_2O_2. Also shown is the data obtained prior to treatment.

Growth and Device Information

The test structure was constructed on MBE film PU 092486. The starting substrate for film 092486 was Zn doped ($1.5 \times 10^{19} cm^{-3}$) horizontal (100) Bridgeman material with an etch pit density of less than $500 cm^{-2}$. The GaAs layers were grown at a substrate temperature of 605 °C and the AlGaAs layer at a substrate temperature of 625 °C. There was a total of 12μm of material grown in the MBE system prior to the growth of film 092486. A cross section of the MBE film layers is shown in Figure 4.12. The MBE film structure consisted of a 0.69μm P^+-$Al_{0.3}Ga_{0.7}As$ buffer layer, a 0.62μm p-GaAs base, and a 0.69μm n^+-GaAs emitter.

Ohmic contact was made to the n^+ emitter by alloying Au-Ge; In served as the ohmic back contact. Mesa diodes were defined by photolithography and subsequent wet etching in H_2SO_4:H_2O_2:H_2O (1:8:40). The areas of the diodes ranged from $4 \times 10^{-4} cm^2$ to $1.6 \times 10^{-3} cm^2$.

Experimental Data

I-V characteristics were measured at ten different temperatures ranging from 140K to 320K in 20K increments. The I-V curves derived from diode PU-092486-40 are shown in Figure 4.13. For biases between 0.4V and 0.8V, the shunt leakage current was dominant. For biases greater than ~ 0.8V, the I-V characteristics exhibited a brief ~ 2kT region followed by the onset of the series resistance region. The diode ideality factors, n (from $I \propto e^{qV_A/nkT}$), were measured in the low and high bias regions for each curve of Figure 3.9. Also, the logarithmic slope constants, A, (from $I \propto e^{AV_A}$) were measured. The data are presented in Table 3.3.

Purdue Solar Cell 092486 HJ BSF				
	low bias		high bias	
T	n	A	n	A
320.3	5.37	6.74	1.72	21.07
300.3	5.89	6.56	1.81	21.30
280.2	6.33	6.54	1.85	22.32
260.3	6.93	6.43	1.92	23.18
240.2	7.52	6.42	2.07	23.30
220.2	8.43	6.25	2.28	23.09
200.3	8.61	6.73	2.80	20.69
180.2	9.32	6.91	3.19	20.18
160.2	9.43	7.68	4.28	16.92
140.2	10.77	7.68	5.95	13.91

Table 3.3. Diode ideality factors and logarithmic slope constants for the I-V characteristics of Figure 3.9.

Note that, in the low bias region, the logarithmic slope constant showed little variation over a wide range of temperatures. It was this phenomenon that led Fischer et al. [1]. to suspect that the low bias current for their devices was due to bulk tunneling.

If the shunt leakage current is indeed a surface phenomenon, it should be possible to

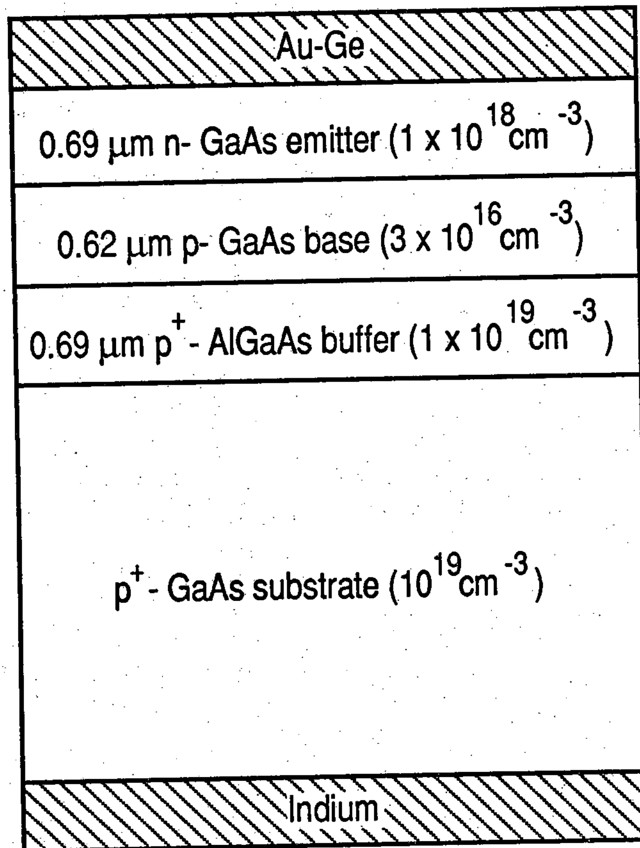

Figure 3.8. A cross section of the MBE film layers for film PU 092486.

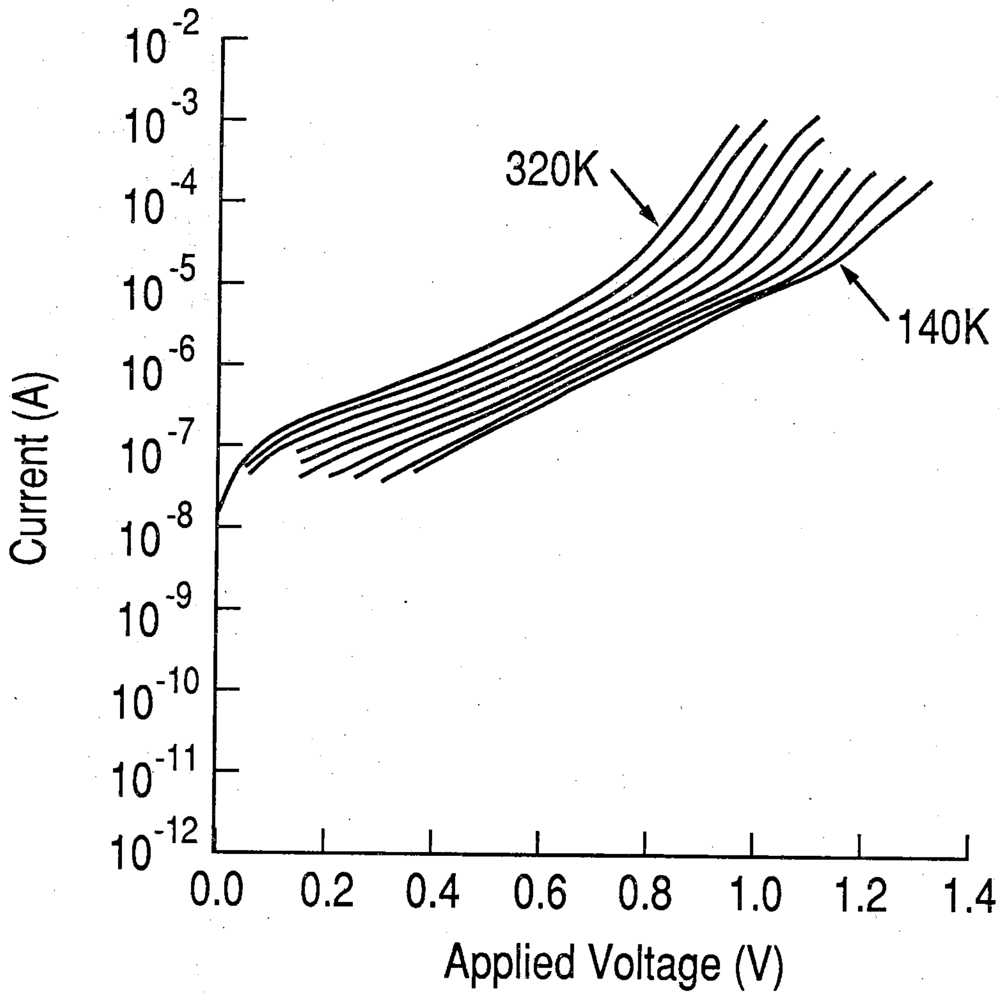

Figure 3.9. I-V characteristics for diode PU-092486-40, 140K-320K.

modify the leakage current by perturbing the surface. Therefore the diode was subjected to the HCl-H_2O_2 treatment, and the I-V characteristics were then remeasured for the same temperatures as before. The data is shown in Figure 3.10. Note that the low bias current was reduced by about two orders of magnitude. This proved conclusively that the low bias current, prior to the treatment, was due to perimeter leakage, since the HCl-H_2O_2 dip affected surfaces only.

3.4 DISCUSSION

The results of sections 3.2 and 3.3 indicate that edge effects all but dominate the I-V characteristics of small area GaAs mesa diodes. For high quality films *perimeter* recombination current appears to be greater in magnitude than *internal* SRH recombination current in the SCR. Moreover, shunt leakage current has also been shown to be a *perimeter* effect.

Expanding on the pioneering work described in sections 3.1 and 3.2, DeMoulin et al. [2], who are fellow members of the MBE GaAs research group at Purdue, have recently shown that perimeter recombination can control the 2kT current in cells as large as 2cm $\times$ 2cm. Moreover, they project that 75% of the 2kT current in 4cm $\times$ 4cm cells will be due to perimeter surface recombination. Carpenter et al. [3], also building upon the original work reported above, have investigated more sophisticated chemical treatments for the passivation of the mesa edges. Carpenter, likewise a member of the MBE GaAs research group at Purdue, has confirmed the fact that the 2kT current can be reduced in magnitude by chemically treating the mesa edges.

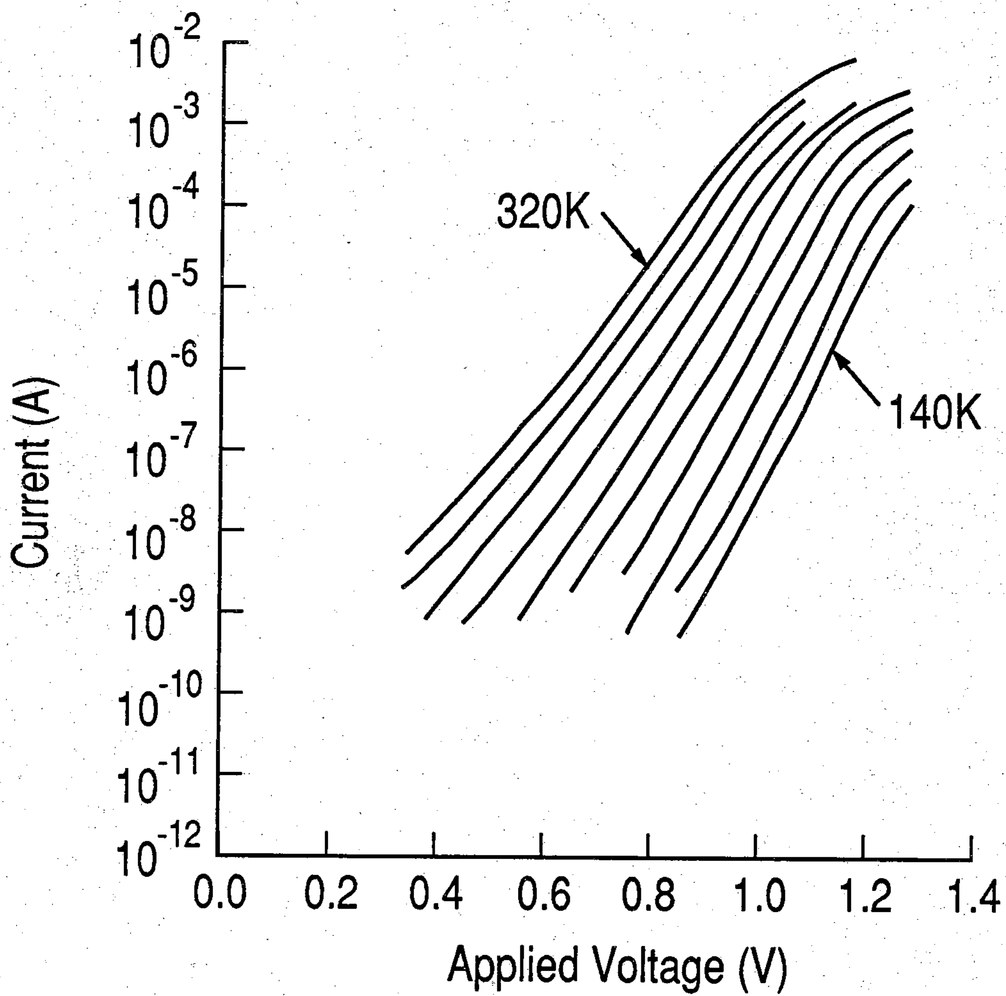

Figure 3.10. I-V characteristics for diode PU-092486-40, 140K-320K, after HCl-H_2O_2 treatment.

CHAPTER 3 REFERENCES

[1] R. Fischer, T. Henderson, J. Klem, N. Chand, and H. Morkoc, "The Effect of Grading in the Electrical Behavior of N_p AlGaAs/GaAs Heterojunction Diodes," *Solid-State Electron.*, Vol. 29, p. 193, 1986.

[2] P.D. DeMoulin, S. P. Tobin, M. S. Lundstrom, M. S. Carpenter, and M. R. Melloch, "Influence of Perimeter Recombination on High-Efficiency GaAs P/N Heteroface Solar Cells," *Electron Device Letters*, Vol. EDL-9, p. 368-370, 1988.

[3] M. S. Carpenter, M. R. Melloch, M. S. Lundstrom, and S. P. Tobin, "Effects of Na_2S and $(NH_4)_2S$ Edge Parrivation Treatments on the Dark Current-Voltage Characteristic of GaAs pn diodes," *Appl. Phys. Lett.*, Vol. 52, pp. 2255-2257, 1988.

CHAPTER 4

X-RAY PHOTOELECTRON SPECTROSCOPY OF THE $(NH_4)_xS_y$ TREATED GaAs (100) SURFACE

4.1. INTRODUCTION

The electrical quality of the GaAs surface has imposed performance constraints upon nearly all GaAs devices[1] and prevented the development of a GaAs-based metal-insulator-semiconductor technology.[2] The surface state density exhibited by a GaAs surface is on the order of 10^{13} $cm^{-2}eV^{-1}$ and the surface recombination velocity is on the order of 10^7 cm/s. Recently, the electrical quality of the GaAs surface has been dramatically improved by various sulfide chemical treatments.[3–8] Sandroff et al. obtained a 60-fold increase in the current gain of a heterojunction bipolar transistor (HBT) by treating the edges of the emitter-base junction with $Na_2S \cdot 9H_2O$.[4] The gain improvement in the HBT was due to a reduction in the perimeter recombination current of the emitter-base junction. Carpenter et al. found similar reductions in the perimeter recombination current of GaAs pn diodes following treatment of the edges with either a $Na_2S \cdot 9H_2O$ or an $(NH_4)_xS_y$ solution.[6] The reduction in perimeter recombination current in the above heterojunction and homojunction pn diodes is due to a reduction in the surface recombination velocities at the edges of the diodes. Yablonovitch et al. found that the improvements in the surface recombination velocity of $Na_2S \cdot 9H_2O$ treated GaAs approaches that of the nearly ideal AlGaAs/GaAs interface.[3]

One limitation of the sulfide treatment is aging; Sandroff et al. found that improvements in the gain of the $Na_2S \cdot 9H_2O$ treated HBT would persist for only a few days.[6] The $(NH_4)_xS_y$ treatment also ages when exposed to air, but appears to be more durable than the $Na_2S \cdot 9H_2O$ treatment.[9] Therefore Carpenter et al. investigated the formation of Schottky barriers on $(NH_4)_xS_y$ treated n- and p-type GaAs,[7] finding an order of magnitude reduction in the surface state density at the $(NH_4)_xS_y$ treated metal-GaAs interface relative to an untreated film. Furthermore, there is no apparent aging of the Schottky diodes after several months of room air exposure.

Because of the dramatic changes in the electrical quality of sulfide treated GaAs surfaces, it is important to determine how the GaAs surface is being altered. This determination may then lead to further improvements in the electrical properties and to ways to prevent aging of the chemically passivated GaAs surface. This would have important implications for GaAs solar cells; we have recently shown that the perimeter recombination can control the 2kT current in GaAs cells as large as 2cm x 2 cm and we project that 75 % of the 2kT current in cells as large as 4 cm x 4 cm will be due to peimeter surface recombination. Therefore we have been performing X-ray photoelectron spectroscopy (XPS) to examine GaAs (100) surfaces following either an acid etch or an etch and $(NH_4)_xS_y$ treatment and present our results in this chapter. The XPS measurements are being performed by Dr. B.A. Cowans and Dr. W.N. Delgass in the School of Chemical Engineering at Purdue University.

4.2. EXPERIMENTAL TECHNIQUE

All samples were cut from MaCom undoped (100) GaAs wafers to roughly 16 mm X 20 mm and etched in 1:1:250 H_2SO_4:H_2O_2:H_2O for 10 seconds followed by a 30 second running deionized water rinse. Sulfide treated samples were then soaked in a saturated

$(NH_4)_xS_y$ solution for 5 minutes, followed by another deionized water rinse and dried under a stream of nitrogen. Samples were stored in dust free containers and exposed to air at room temperature for varying lengths of time before being loaded into the spectrometer.

Spectra were recorded on a Perkin-Elmer PHI 5300 spectrometer. The Mg (1253.6 eV)/Al (1486.6 eV) dual anode was operated at 15 kV and 300 or 400 W, respectively. The spectrometer was calibrated by setting the binding energies of the Au 4f7/2 and Cu 2p3/2 levels to 84.0 and 9332.7 eV, respectively. The full width at half maximum for the Ag 3d5/2 level (368.4 eV) was 0.86 eV at 489 kHz for the pass energy at which sample data was collected. The C 1s binding energy was recorded at 284.3 eV for all GaAs samples. A low energy flood gun, operated at either 2.0 mA emission current with 1.0 eV bias (Mg radiation) or 5.0 mA emission current with 1.5 eV bias (Al radiation), was used to control charging on the undoped samples. Background pressure in the analysis chamber was always less than $1x10^{-9}$ torr. Data accumulation times were roughly 5 hours[9] and data reduction was accomplished using Perkin-Elmer software.

4.3. EXPERIMENTAL RESULTS AND DISCUSSION

Photoelectron spectra of the As 3d core level are shown in Fig. 4.1. The upper spectrum is for an etched sample following a 15 minute air exposure while the lower spectrum is for a sulfide treated sample following a 20 minute air exposure. The absense of the large As oxide peak from the spectrum of the treated sample clearly demonstrates that the As atoms are oxidized much less on the sulfide treated surface.

The XPS spectra observed for the different core levels were fit in the following way. The As 3d level was fit by four peaks which are assigned as follows: As (of bulk GaAs) 3d5/2 and 3d3/2 peaks at 40.6 and 41.3 eV respectively,[10,11] an As-sulfide species at 42.5 eV,[12] and an As oxide at 44.1 eV.[10,11] (Note that the spin-orbit splitting is not resolved for the sulfide and oxide peaks. Also note the sulfide and oxide species are not specifically defined, since at these low coverages, vide infra, a bulk-type stochiometric compound probably does not exist.) The As 2p3/2 level was fit by three peaks also assigned as metal, sulfide, and oxide at 1323.1 eV, 1324.6 eV, and 1326.3 eV respectively. Both Ga 3d and 2p3/2 levels were fit by two peaks, a metal and an oxide. The Ga 3d metal and oxide peaks occurred at 19.0 eV and 20.0 eV respectively while the Ga 2p3/2 metal and oxide peaks occurred at 1117.2 eV and 1118.3 eV respectively. (Due to the smaller binding energy shift of Ga, we cannot resolve the Ga 3d5/2 and 3d3/2 level.)

The binding energies of the sulfur 2s and 2p levels were observed at 226.0 eV and 161.9 eV respectively, suggesting that the sulfur atoms which form this layer are most probably in the sulfide (2^-) state. The position of the S 2p level for most metal sulfides is normally in the range 160.0 eV to 163.0 eV.[13] The binding energies of the sulfide did not shift with time and therefore we believe the chemical nature of the sulfur does not change significantly with exposure to air. The sulfur to total metal ratios obtained are listed in Table I. The magnitude of these ratios shows little change with time, indicating that the sulfur is not lost as the surface becomes oxidized. However, the angular dependence of these ratios is more pronounced initially than after long exposure to air, which indicates that the GaAs may be diffusing through the sulfide as the surface becomes oxidized. Further evidence of this result comes from the strong angular dependence of the ratios of sulfur to oxidized Ga and As.

The fractional coverage of sulfur was calculated from the standard equation relating angular dependence of the sulfur and gallium intensities assuming a uniform layer

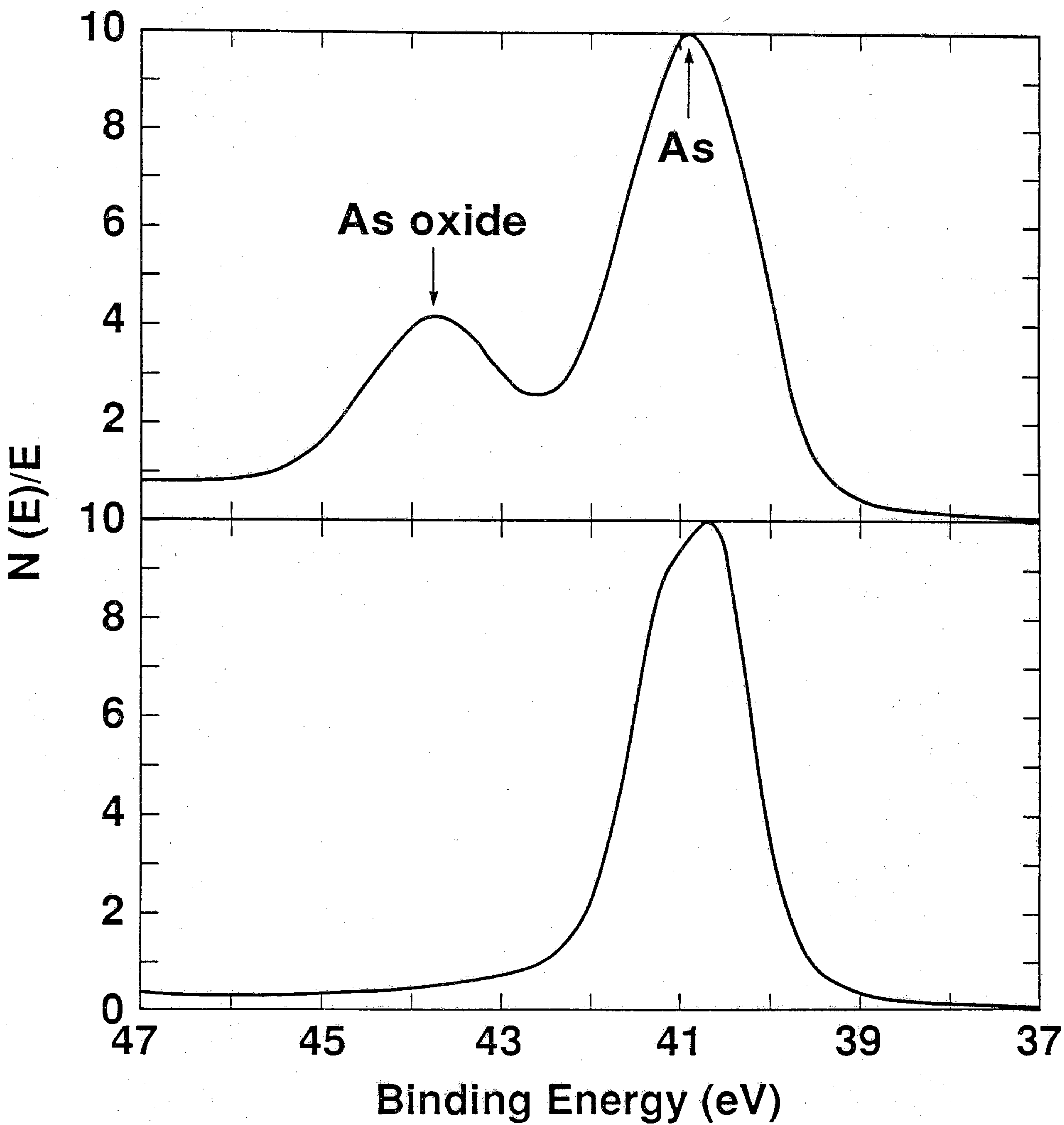

Fig. 4.1 Upper spectrum: etched sample following a 15 minute air exposure. Lower spectrum: $(NH_4)_xS_y$ treated sample following a 20 minute air exposure.

Table I. Relative atomic ratios calculated from O 1s, S 2s, and Ga and As 3d level intensities taking into account only the photoelectron cross section (Mg radiation).

Sample	Angle	S/O	S/Ga_{ox}	S/As_{ox}	$S/(Ga+As)_{total}$
Treated	30	1.08	1.98	4.69	0.10
0.33 hrs.	60	1.04	0.73	7.80	0.05
Treated	30	0.19	0.35	0.75	0.07
116 hrs.	60	0.22	0.40	1.21	0.05
Treated	30	0.17	0.29	0.76	0.06
264 hrs.	60	0.26	0.44	1.74	0.06

Table II. Relative atomic ratios calculated from O 1s and Ga and As 3d level intensities taking into account only the photoelectron cross section (Mg radiation).

Sample	Angle	O/Ga_{total}	O/As_{total}	$O/(Ga + As)_{total}$
Etched	30	1.01	0.51	0.34
0.25 hrs.	60	0.42	0.41	0.21
Treated	30	0.16	0.21	0.09
0.33 hrs.	60	0.07	0.12	0.04

Table III. Relative atomic ratios calculated from Ga and As 3d level intensities corrected for photoelectron cross section (Mg radiation). Calculation of total oxide thickness is described in the text.

Sample		Etched		Treated	
Time (hrs.)		0.25	145	0.33	116
As_{ox}/Ga_{ox}	30	2.52	0.95	0.42	0.47
	60	1.38	0.78	0.09	0.33
As_m/Ga_m	30	1.93	1.21	0.86	0.96
	60	1.00	0.80	0.61	0.67
Total Oxide Thickness (Å)		5.0	8.1	1.4	5.7

model,[14,15]

$$\frac{I_S}{I_{Ga}} = \frac{S_S \sigma_S \eta_S \lambda_S [1-\exp(d/\lambda_s \sin\Theta)]}{S_{GA} \sigma_{Ga} \eta_{Ga} \lambda_{Ga} \exp(d/\lambda_S \sin\Theta)} \tag{1}$$

where I is the intensity, S is the spectrometer transmission function, σ is the photoelectron cross section,[16] η is the atomic density, λ is the photoelectron mean free path, d is the thickness of the sulfide layer, and Θ is the angle between the sample surface and the entrance slit to the analyzer. The energy dependence of the spectrometer transmission function was calculated according to Hanke et al.[17] and electron mean free paths were taken from Kwei and Chen.[18] The sulfur coverage can then be determined from the atomic density of sulfur. Assuming the sulfide layer thickness equals the diameter of the sulfide ion (3.68 Å), the sulfur coverage is roughly 3.6×10^{14} atoms/cm,[2] corresponding to 0.6 monolayer of sulfur on the surface.

The (100) GaAs surface may have many phases with As coverages ranging from roughly 0.2 to 1 monolayer.[19] Massies et al.[20] have shown that the sticking coefficient of H_2S on the (100) GaAs surface is dependent upon the As coverage with the sticking coefficient being greatest on the As depleted surface. They also determined the saturation coverage of H_2S to be between 0.7 and 1 monolayer. Furthermore, Sandroff et al.[3,4] stated from their preliminary Auger analysis that roughly half a monolayer of sulfur remains after washing the Ns_2S9H_2O treated surface. These results are consistent with the 0.6 monolayer of sulfur and the slight Ga enrichment (as discussed below) observed on our sulfide treated surfaces.

The peak intensity ratios of oxygen to total metal that were observed are shown in Table II. In all cases, the oxygen to metal ratio is higher for the etched surface than for the treated surface. These ratios clearly show that the sulfide treatment limits initial oxidation on the GaAs (100) surface. The O/Ga_{total} ratio at 30 degrees is greater than the O/As_{total} ratio for the etched sample and less than the O/As_{total} ratio for the treated sample. In addition, both oxide and metal As/Ga ratios, as shown in Table III, are larger for the etched surface than the treated one. These results suggest that the surface of the etched sample is enriched in As while the surface of the sulfide-treated sample is slightly enriched in Ga. Acid etched surfaces have indeed been found to be As-rich.[11] The effect of a basic sulfide solution on surface composition has not been previously reported. The angular dependence of the As_{ox}/Ga_{ox} ratios in Table III indicates that the surface is enriched in As oxide relative to Ga oxide for both etched and sulfide treated samples. This suggests that oxidized As migrates to the surface as the surface becomes oxidized.[14]

Oxide layer thicknesses were calculated for oxide/metal ratios using the uniform layer model and equation (1) described above. The spectrometer function was assumed to be identical for both oxide and metal peaks. A mean free path of 23.5 Å (Mg radiation) was used for both oxide and metal Ga and As 3d levels.[17] Atomic densities were calculated from the nominal bulk densities for Ga_2O_3, As_2O_3, and GaAs. The total oxide thicknesses listed in Table III were determined from the sum of individual Ga and As oxide thicknesses. Again, we see that the sulfide treatment limits initial oxidation on the GaAs (100) surface. The submonolayer coverage for the initial sulfide treated sample is consistent with the amount of sulfide coverage. The total oxide thicknesses for both etched and treated surfaces after long air exposure are nearly equivalent.

4.4. CONCLUSION

In conclusion, we have obtained the following results from our XPS analysis: (i) The $(NH_4)_xS_y$ treatment produces 60 % of a monolayer of sulfide coverage, which severly restricts the initial oxidation of the GaAs (100) surface and a slight Ga enrichment occurs. (ii) The binding energies of the sulfur 2s and 2p levels, at 225.9 eV and 161.9 eV respectively, suggest that the sulfur atoms which form this layer are probably in the sulfide (2^-) oxidation state and do not change chemical state with long exposure to air. (iii) The sulfide layer is not lost as the GaAs surface becomes oxidized and apparently remains near the oxide interface. This suggests that the GaAs diffuses through the sulfide layer as the surface becomes oxidized. (iv) The ultimate oxide thicknesses for both etched and sulfide treated surfaces are nearly equivalent after long exposure to air. Furthermore, the angular dependence of the As_{ox}/Ga_{ox} ratios indicates that the surface is enriched in As oxide to Ga oxide for both etched and treated samples after long exposure to air.

CHAPTER 4 REFERENCES

[1] D. L. Lile, J. Vac. Sci. Tech B2, 496 (1984).

[2] C. R. Zeisse, L. J. Messich, and D. L. Lile, J. Vac. Sci. Tech. 957 (1977).

[3] E. Yablonovitch, C. J. Sandroff, R. Bhat, and T. Gmitter, Appl. Phys. Lett. 51, 439 (1987).

[4] C. J. Sandroff, R. N. Nottenberg, J.-C. Bischoff, and R. Bhat, Appl. Phys. Lett. 51, 33 (1987).

[5] R. N. Nottenberg, C. J. Sandroff, D. A. Humphrey, T. H. Hollenbeck, and R. Bhat, Appl. Phys. Lett. 52, 218 (1988).

[6] M. S. Carpenter, M. R. Melloch, M. S. Lundstrom, and S. P. Tobin, Appl. Phys. Lett. 52, 2157 (1988).

[7] M. S. Carpenter, M. R. Melloch, T. E. Dungan, Appl. Phys. Lett. 53, 66 (1988).

[8] E. Yablonovitch, H. M. Cox, T. Gmitter, Appl. Phys. Lett., 51, 439 (1988).

[9] R. P. Vasquez, B. F. Lewis, F. J. Grunthaner, Appl. Phys. Lett. 42, 293 (1983).

[10] C. M. Demanet, M.A. Marais, Surface and Interface Analysis, 7, 13 (1985).

[11] J. Massies, J. P. Contour, J. Appl. Phys. 58, 806 (1985).

[12] W. J. Stec, W. E. Morgan, R. G. Albridge, J. R. Van Wazer, Inorg. Chem. 11, 219 (1972).

[13] C. D. Wagner, W. M. Riggs, L. E. Davis, J. F. Moulder, G. E. Muilenberg, *Handbook of X-ray Photoelectron Spectroscopy,* Perkin-Elmer Corp., Eden Prairie, MN, 1979.

[14] W. A. Fraser, J. V. Florio, W. N. Delgass, W. D. Robertson, Surface Science 36, 661 (1973).

[15] C. S. Fadley, Prog. Solid State Chem. 11, 265 (1974).

[16] J. H. Scofield, J. Electron Spectro. Rel. Phen. 8, 129 (1976).

[17] W. Hanke, H. Ebel, M. Ebel, J. Electron Spectro. Rel. Phen. 40, 241 (1986).

[18] C. M. Kwei, L. W. Chen, Surface and Interface Analysis, 60 (1988).

[19] W. Ranke, K. Jacobi, Prog. Surf. Sci. 10, 1 (1981).

[20] J. Massies, F. Dezaly, N. T. Linh, J. Vac. Sci. Tech. B17, 1134 (1980).

APPENDIX: PUBLICATIONS

This appendix contains reprints of the publications which resulted from the work conducted during the past year.

[1] M.S. Lundstrom, "Device Physics of Crystalline Solar Cells," *Solar Cells*, Vol. 24, pp. 91-102, 1988.

[2] M.E. Klausmeier-Brown, C.S. Kyono, P.D. DeMoulin, S.P. Tobin, M.S. Lundstrom, and M.R. Melloch, "Sequential Etch Analysis of Electron Injection in P^+ GaAs," *IEEE Trans. Electron Dev.*, Vol. ED-35, pp. 1159-1161, 1988.

[3] M.E. Klausmeier-Brown, M.S. Lundsrrom, M.R. Melloch, and S.P. Tobin, "Effects of Heavy Impurity Doping on Electron Injection in p^+-n GaAs Diodes," *Applied Phys. Lett.*, Vol. 52, pp. 2255-2257, 1988.

[4] M.S. Carpenter, M.R. Melloch, M.S. Lundstrom, and S.P. Tobin, "Effects of Na_2S and $(NH_4)_2S$ Edge Passivation Treatments on the Dark Current-Voltage Characteristic of GaAs pn Diodes," *Applied Phys. Lett.*, Vol. 52, pp. 2157-2159, 1988.

[5] P.D. DeMoulin, S.P. Tobin, M.S. Lundstrom, M.S. Carpenter, and M.R. Melloch, "Influence of Perimeter Recombination on High-Efficiency GaAs P/N Heteroface Solar Cells," *IEEE Electron Dev. Lett.*, Vol. EDL-9, pp. 368-370, August 1988.

Solar Cells, *24* (1988) 91 - 102

DEVICE PHYSICS OF CRYSTALLINE SOLAR CELLS*

MARK S. LUNDSTROM

School of Electrical Engineering, Purdue University, West Lafayette, IN 47907 (U.S.A.)

(Received November 16, 1987; accepted December 22, 1987)

Summary

High material quality is a prerequisite for achieving high conversion efficiencies, but cells must be carefully designed to maximize performance. Very high conversion efficiencies are now being achieved in two quite different semiconductors, silicon and GaAs. The internal device physics of crystalline silicon and GaAs cells are compared and contrasted in this paper. The paper illustrates how detailed device simulation is used to examine the internal performance of cells, identify loss mechanisms and assess design options.

1. Introduction

Record high conversion efficiencies are now being reported for both crystalline silicon and gallium arsenide solar cells. High material quality was a prerequisite for achieving these high efficiencies, but cell design was also a crucial factor. The design of a solar cell is based on the properties of the semiconductor, the constraints imposed by the technology, and on an understanding of the cell's internal device physics. The purpose of this paper is to discuss, compare and contrast the device physics of silicon and gallium arsenide cells. The paper does not attempt a comprehensive review of silicon and GaAs cells; its emphasis is on the device physics that confronts the cell designer. A review of how such high efficiencies were achieved in two quite different semiconductors demonstrates that there is no single, best solar cell design but, rather, that solar cell designs evolve as dominant recombination losses are identified. The paper will also illustrate how physical device simulation is used to identify loss mechanisms and to guide device design.

2. Cell design fundamentals

We begin with a brief review of the basic concepts underlying the design of high-efficiency cells. The simple expression

*Paper presented at the 8th Photovoltaic Advanced Research and Development Project Review Meeting, Denver, CO, U.S.A., November 15 - 18, 1987.

0379-6787/88/$3.50 © Elsevier Sequoia/Printed in The Netherlands

$$\eta = \frac{J_{SC} V_{OC} \mathrm{FF}}{P_{inc}/A} \tag{1}$$

shows that high efficiency results by maximizing short-circuit current J_{SC} and open-circuit voltage V_{OC} while maintaining a high fill factor (FF). The selection of a semiconductor is a compromise; to maximize short-circuit current, a small band gap should be selected, but for high open-circuit voltage, a large band gap is needed. The band gaps of silicon and GaAs are nearly optimum for the solar spectrum; both cells show limit conversion efficiencies above 30% at one sun and above 35% at 500 suns [1].

The object of cell design is to approach the cell's thermodynamic limit by maximizing the number of optically-generated carriers while minimizing recombination losses. To achieve high efficiencies, 98% of the available photons should be absorbed. For GaAs, a layer of semiconductor about 4 μm thick is adequate, but for silicon, a layer 1500 μm thick is required. For such thick silicon cells, the electrical performance would be degraded by recombination losses. Much of the recent improvement in silicon performance is due to the use of light-trapping techniques which makes the cell appear optically thick yet electrically thin. There has also been much progress in sophisticated antireflection coatings, texturizing and grid design which have resulted in reflection plus shadowing losses below 3%. Successful cell design consists of identifying, quantifying, then suppressing the important recombination mechanisms. The designer needs the ability to examine the cell's internal recombination rate. Unfortunately, electrical measurements tend to reflect the integrated recombination rate and cannot therefore identify the importance of specific internal mechanisms. Experiments to isolate and quantify various mechanisms can be performed, but they are difficult and time-consuming. An alternative approach which involves the use of a detailed, physical device model is discussed next.

3. Physical device simulation

The performance of a cell is described by Poisson's equation and by the electron and hole continuity equations which comprise three coupled non-linear equations in three unknowns (electrostatic potential, electron concentration and hole concentration). Under well-known simplifying assumptions (*e.g.* simple doping profiles, complete ionization of dopants, low-level injection etc.) the governing equations can be simplified and closed-form solutions obtained, but cells often operate under conditions that invalidate many simplifying assumptions. Moreover, the continued quest for higher efficiencies demands more accurate and detailed modeling of the device.

Physical device simulation consists of solving the governing equations directly by using a digital computer [2, 3]. The only approximations involved are numerical (*e.g.* derivatives are approximated by finite differences). The

accuracy of the model is limited not by the ability to solve the governing equations, but by knowledge of the physics and the values of various materials parameters. Since the solution is obtained at each point within the device, not simply at its terminals, the internal operation of the device can be probed at will. For crystalline silicon cells, computer codes that solve the governing equations in one and two dimensions are now widely available. Confidence in the predictive ability of these codes was established by comparing simulations with experiments. The successes and failures of these comparisons deepened the understanding of silicon cell device physics and focused experimental work on topics of most concern to device design. After a decade of such work, confidence in the codes is high; they now serve as reliable guides for cell design. For GaAs and "newer" materials, confidence in the physical models is not yet as high, but trends can be modeled and the merits of various designs gauged. These models are improving as knowledge of device physics and parameter values improves.

4. Device physics of silicon cells

In this section, we make use of computer simulation to examine and compare the internal device physics of two different concentrator cells. The first cell considered is similar to the Sandia, p on n cell developed in the early 1980s [4]. Next, we examine the internal device physics of a backside-contact cell similar to the Stanford design [5]. Identical, high-quality material is assumed for both of the cells to assess the role of device design on cell performance.

The Sandia-like p on n cell is displayed in Fig. 1; it is fabricated in a 0.3 Ω cm substrate 305 μm thick. The p^+ emitter is 0.4 μm thick with a peak concentration of 1.5×10^{20} cm^{-3}, and the back-surface field is a diffused junction 1.0 μm thick with a peak doping of 5.0×10^{19} cm^{-3} (complementary error functions were used for both profiles). The Shockley–Read–Hall (SRH) lifetimes were modeled by

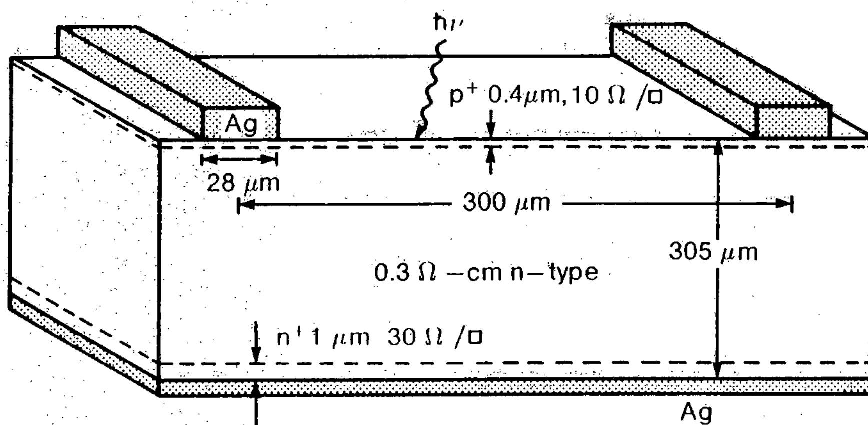

Fig. 1. Physical structure of the Sandia-like [4] p on n concentrator cell.

$$\tau = \frac{\tau_o}{1 + N/N_c} \tag{2}$$

where τ_o, the SRH lifetime in intrinsic material, was taken to be 1000 μs and N_c, which controls how the SRH lifetime degrades with doping, was set to 7.1×10^{15} cm^{-3}. Auger recombination was also modeled and the passivated surfaces were characterized by a surface recombination velocity of 10 cm s^{-1}.

The results of a two-dimensional physical simulation of the p on n cell are summarized in Table 1; the simulated conversion efficiency under concentration exceeds 20%. Simulation results show that 80% of the available photons are collected. About half of the lost photocurrent is caused by reflection and shadowing; the other half of the loss is about equally divided between carrier recombination within the cell (about 4%) and transmission of above-band-gap photons through the 300 μm thick cell.

Figure 2 summarizes the recombination losses at V_{OC} for this cell as revealed by physical simulation. The relatively small (about 4%) contribution of base recombination to the dark current should be noted. The heavy base doping, in contrast with earlier cell designs, effectively suppresses forward-biased injection of holes into the base. The dominant V_{OC}-loss mechanism is recombination within the thin, heavily doped p-type emitter. Since the emitter is well passivated, this current component is due to injected minority carriers recombining within the volume of the emitter and can be described by

$$J_E(p^+ \text{ bulk}) = q\frac{n_{iE}^2}{N_A}\frac{W_E}{\tau} \tag{3}$$

where n_{iE} is the intrinsic carrier concentration in the emitter, N_A is the average doping, W_E is the width of the emitter and τ is the minority carrier lifetime. The emitter component of the dark current dominates for two reasons. Firstly, so-called band-gap narrowing effects effectively shrink the band gap within the heavily doped emitter, so that n_{iE} may greatly exceed its value in intrinsic silicon n_{io} [6]. In the heavily doped emitter, n_{iE}^2 may

TABLE 1

Simulated performance of the p on n silicon concentrator cell at T = 24 °C under 180X air mass (AM) 1.5 direct suns

Cell parameter	*Value*
V_{OC} (V)	0.757
J_{SC} (A cm^{-2})	5.52
FF (%)	79
η (%)	22
J_{SC}/J_L (max) (%)	80
Internal conversion efficiency (%)	96
Shadow plus reflection (%)	9.4

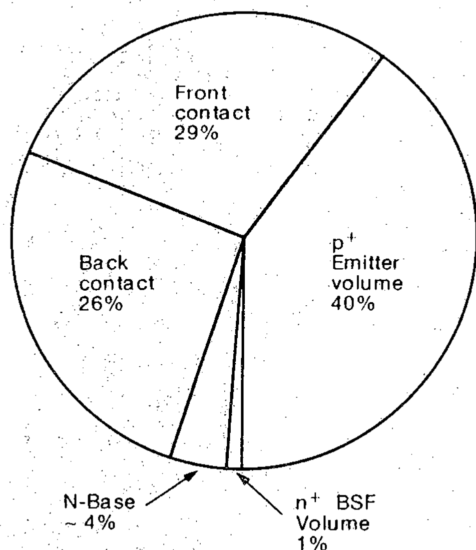

Fig. 2. Recombination analysis of Sandia-like p on n silicon concentrator cell at V_{OC}.

be several times the value in lightly doped silicon. Secondly, the emitter recombination rate is high because of the dominance of Auger recombination in the heavily doped emitter. The Auger-limited, low injection minority carrier lifetime

$$\tau = \frac{1}{C_p N_A^2} \tag{4}$$

is only 1 ns in p-type silicon doped to 1×10^{20} cm^{-3}.

Figure 2 also shows that more than half of the recombination losses in this cell arise from minority carriers recombining at the metal contacts. These losses are a consequence of band-gap narrowing which causes a substantial injection of minority carriers into the heavily doped regions where they can recombine at the metal contacts. The back-surface field does improve the performance of this cell, but it is not a perfect minority carrier mirror; a number of minority carriers reach the back metal contact and recombine there.

According to these simulation studies, silicon cell design should be directed at suppressing recombination in the emitter volume and at the metal contacts. Further increases in J_{SC} are possible if the already low shadowing losses can be eliminated and if the high internal quantum efficiency can be improved. The Stanford backside point contact cell [5] achieves both objectives. In the Stanford cell, both the p- and n-type diffused junctions are reduced to small dots on the backside of the wafer, so grid shadowing losses are eliminated, and Auger recombination in the volume of the diffused regions is reduced, as is recombination at the metal–semiconductor contacts. The light base doping is used to maximize Shockley–Read–Hall lifetimes; its resistance is low because the base operates in high level injection. To maintain a high internal collection efficiency and open-circuit voltage, the cell must be thin. Light-trapping techniques are then essential to make the semiconductor appear optically thick.

TABLE 2

Simulated performance of the Stanford backside point contact cell (T = 24 °C, AM 1.5 direct normal, at 180×)

Cell parameter	*Value*
V_{OC} (V)	0.826
J_{SC} (A cm^{-2})	6.39
FF (%)	85
η (%)	30.1
J_{SC}/J_L (max) (%)	93
Internal conversion efficiency (%)	99.5
Shadow plus reflection loss (%)	0

Table 2 summarizes the electrical performance of the backside point contact cell under concentration. The very substantial reduction of recombination losses achieved by reducing the volume of the heavily doped regions and the area of the metal-semiconductor contacts is reflected in the especially high open-circuit voltage. The recombination analysis at V_{OC} for this cell, displayed in Fig. 3, shows that the p^+ volume, the n^+ volume and the metal contacts contribute about equally to the recombination losses. Recombination losses associated with the intrinsic cell are so low that parasitic losses associated with recombination at the perimeter of the cell should be considered. Because perimeter recombination was not simulated and the extrinsic series resistance was assumed to be zero, the simulated efficiency is about two percentage points above the observed value.

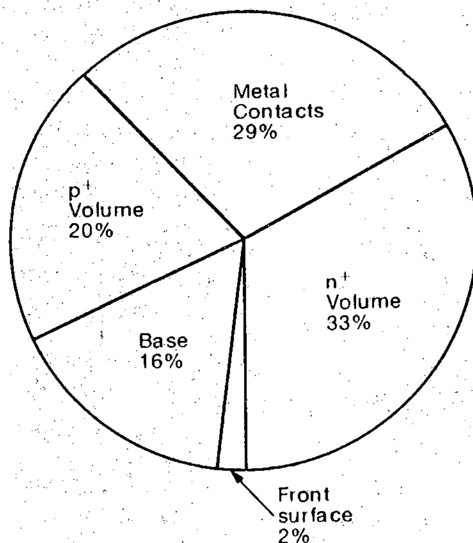

Fig. 3. Recombination analysis of the Stanford-like point contact cell at V_{OC}.

5. Device physics of GaAs cells

Although very high efficiencies have been reported for gallium arsenide solar cells under both one sun and concentration [7, 8], our understanding

of their internal device physics is not mature by silicon standards. The most common cell design, the p on n heteroface displayed in Fig. 4, has not changed appreciably for several years, but efficiencies have continued to rise as antireflection coatings, material quality and fabrication techniques have improved [7]. Experiments to probe the internal device physics have recently begun (*e.g.* refs. 9 and 10), as has the serious use of physical device simulation. Simulation now describes cell performance reasonably well and can be used to assess the potential of design alternatives.

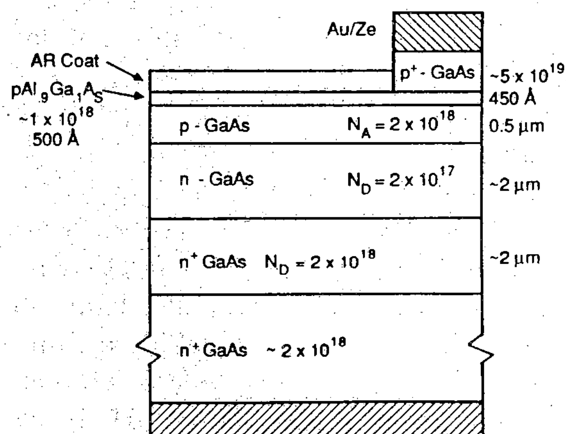

Fig. 4. Physical structure of the Spire-like p on n GaAs heteroface cell [9].

The basic cell structure, displayed in Fig. 4, consists of a p^+ emitter and an n-type base. The heavily doped buffer layer serves as a minority carrier mirror, and the wide band gap $Al_{0.9}Ga_{0.1}As$ window layer passivates the front surface. Numerical simulations by PUPHS [2] demonstrate that the band gap of the window (about 2 eV) permits a substantial photogeneration of carriers (about 5% of the available photons are absorbed in a window 500 Å thick). A few per cent of the available photons are also generated in the n^+ buffer layer. The simulated internal quantum efficiency is compared with a typical measured value [10] in Fig. 5. The drop in quantum efficiency at short wavelength is due to absorption in the window layer, but the window layer is not dead. A front surface recombination velocity at the AlGaAs surface of 5×10^6 cm s^{-1} (which is somewhat below the value of about 10^7 cm s^{-1} typical of a bare GaAs surface) is needed to model the short wavelength quantum efficiency. About one-half of the carriers photogenerated in the window layer are collected. The long wavelength quantum efficiency is quite high; very long base lifetimes are implied (a value of 15 ns was used in the simulation). The peak quantum efficiency, typically 90% - 95%, is very high, but contrasts with the results for silicon in which the quantum efficiency routinely peaks very near 100%. The peak quantum efficiency can be explained by assuming a recombination velocity at the heteroface of several times 10^4 cm s^{-1} to a few times 10^5 cm s^{-1}, which is substantially above the 10^4 cm s^{-1} commonly assumed as an upper limit. But other explanations, such as a parasitic absorption mechanism that does not generate carriers, cannot be ruled out.

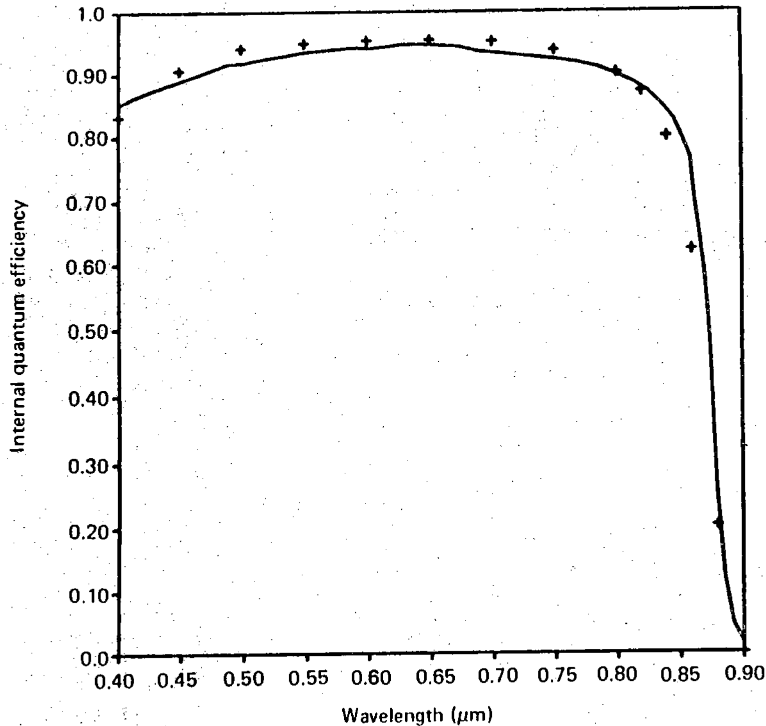

Fig. 5. Internal quantum efficiency *vs.* wavelength for a typical p on n heteroface cell (——, PUPHS simulation; + + +, from ref. 11).

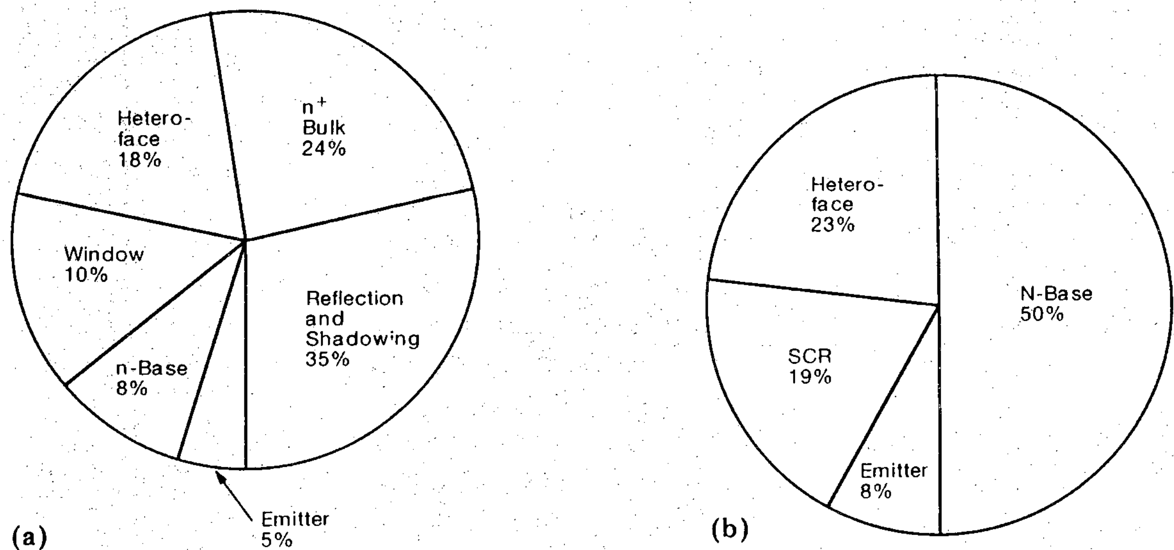

Fig. 6. (a) Short-circuit current loss analysis of the p on n GaAs heteroface cell. In the simulated cell, 13% of the available photogenerated carriers are lost. This chart shows where those photons are lost; (b) recombination analysis of the p on n GaAs heteroface cell at the one-sun V_{OC}.

Short-circuit current losses for this cell are summarized in Fig. 6(a). Reflection and shadowing by the top metal grid are the largest component of optical loss. The sizable loss contributed by the n^+ buffer layer and substrate indicates that the cell's active layer is not thick enough optically, but

increasing its thickness would degrade the open-circuit voltage (in this regard, GaAs cells could benefit from light-trapping techniques like those employed for silicon cells). The loss contributed by the heteroface reflects the high interface recombination velocities implied by the peak internal quantum efficiency.

Recombination losses at open-circuit voltage are summarized in Fig. 6(b). In contrast to the silicon p on n cells, the GaAs cell's dark current is base-dominated. The emitter doping for the GaAs cell is not extremely high, so minority carrier electrons are injected into the emitter. But injection of minority carriers into the emitter does not have the dire consequences that it does for silicon cells because the metal contacts are passivated by the heteroface and the lifetimes in the emitter are relatively long (about 2 ns). The performance of the n^+ back-surface field is not severely compromised because majority carrier degeneracy is strong in n-type GaAs and acts to counter band-gap shrinkage. For n–p cells, however, the performance of p^+ back-surface fields should be degraded by band gap shrinkage, which may explain why heterojunction back-surface fields have proved effective for such cells [12]. The simulations show a sizable, though not dominant, emitter component to the dark current which is a consequence of the relatively high heteroface recombination velocity used to match the low peak internal quantum efficiency. Strong variations of dark current with emitter design should not be observed until the dominant loss, base recombination, is suppressed.

Table 3 summarizes the simulated performance of the Spire-type p on n heteroface cell at one sun and the performance of a similar cell (with a redesigned grid) under concentration. These results were obtained with a two-dimensional, AlGaAs–GaAs simulator. The table shows that about 87% of the available photons are collected; in the very best silicon cells the corresponding fraction exceeds 95%. The cell's dark current is primarily caused by recombination in the n-type base. Under concentration, simulations of a similar cell (with a very conservative metal grid that results in 11% shadowing) show a conversion efficiency of more than 27%.

When we consider optimizing this cell, it is clear that the first objective must be to raise the fraction of available carriers that are collected. The reason for the low peak internal quantum efficiency (low, that is, by silicon standards) must first be identified. As discussed previously, a tentative explanation is that the heteroface recombination velocity exceeds 10^4 cm s^{-1}. When this value is lowered to 10^4 cm s^{-1}, simulations show nearly 100% peak internal quantum efficiency. Modest improvements in cell performance can also be achieved by reducing the dark current. To reduce dark currents, the focus should be on suppressing the base current, which is most easily accomplished by increasing the base doping (if the diffusion length in the base can be maintained). No fundamental mechanism limits the hole lifetime in n-GaAs until the doping exceeds 10^{18} cm^{-3} [14 - 16], so base dopings higher than 2×10^{17} cm^{-3} could be employed. This approach has been adopted in the Varian p on n heteroface cell [8]. The use of heterojunction back-surface fields to suppress dark current might also be considered, but in

TABLE 3

Simulated performance of the p on n heteroface GaAs cell

Cell parameter	*1 sun*[a]	*500 suns*[b]	*500 suns*[c]
V_{OC} (V)	1.038	1.19	1.22
J_{SC} (mA cm^{-2})	27.4	10.9	11.4
FF (%)	86	87	86
η (%)	24.6	27.1	39.0
J_{SC}/J_L (max) (%)	87	81	85
Internal CE (%)	90	89	88
Shadow plus reflection (%)	5	11	6

All simulations were performed at 25 °C.

[a]Refers to the cell displayed in Fig. 4 under an AM 1.5 global spectrum normalized to 100 mW cm^{-2} [13].

[b]Refers to a similar cell at 500 AM 1.0 direct normal suns.

[c]Refers to an optimized cell as described in the text.

this case the base must be thickened to prevent a loss of photocurrent [11]. Since the back-surface field will be located more than a diffusion length beyond the junction, significant benefits are not expected for heterojunction back-surface fields in p on n cells. Finally, we note that 1 ns lifetimes can be maintained in the p-type emitter for doping densities near 10^{19} cm^{-3} [14, 17, 18]. For such lifetimes, the short wavelength internal quantum efficiency does not suffer (recent experiments provide confirmation [10]). The implication is that the emitter doping can be substantially raised to lower the emitter sheet resistance without sacrificing internal quantum efficiency.

Table 3 also shows the simulated performance of an optimized cell, which was designed as discussed above. The cell is identical to that displayed in Fig. 4 except that the peak internal quantum efficiency has been raised to nearly 100% by lowering the heteroface recombination velocity to 1×10^4 cm s^{-1}, the emitter doping has been raised to 8×10^{18} cm^{-3} and the base doping has been raised to 5×10^{17} cm^{-3}. The lowered sheet resistance of the p^+ emitter allowed the front grid to be redesigned to lower shadowing losses to 6% without degrading the fill factor. A significant gain in performance is predicted; the cell shows a conversion efficiency of 29%. Even with this very high conversion efficiency, the short-circuit current represents only 85% of the available photons. Conversion efficiencies in excess of 30% are achievable if the short-circuit current performance of GaAs cells can be raised.

6. Conclusions

In this paper the internal device physics of a number of different solar cell designs in two different crystalline semiconductors has been studied. A unifying theme of the discussion was the role that detailed device simulation plays in guiding solar cell design. Some general conclusions regarding the

design of silicon, GaAs and all crystalline cells can be derived from this discussion. The first is the importance of maximizing short-circuit current; the very best silicon cells make use of long-lifetime material and light-trapping techniques to collect about 96% of the available photocurrent [5]. This appears to be the key area of opportunity for improving the already high efficiency of GaAs cells (the best GaAs cells collect about 88% of the available photocurrent [7]). Band-gap narrowing effects play a dominant role in silicon cell design; they enhance the injected minority carrier concentration so that Auger recombination and recombination at the metal contacts dominates. Much of silicon cell design focuses on designing around heavy doping effects. For GaAs cells, band-gap narrowing may occur (especially in p^+ GaAs), but its consequences are not so dire. Both materials display high fill factors (typically just under 80% for silicon at one sun and somewhat over 80% for GaAs). A conversion efficiency of 30% under concentration appears to be an achievable goal for both silicon and GaAs cells.

Acknowledgments

The author is indebted to E.K. Banghart for performing the simulations of silicon cells and to P.D. DeMoulin for the GaAs simulations. He also benefited from extensive discussions with S.P. Tobin of Spire Corporation and J.M. Gee of Sandia National Laboratories. Development of the simulation tools described in this paper was supported by Sandia National Laboratories; experimental studies to verify the GaAs models were supported by the Solar Energy Research Institute.

References

1 C. H. Henry, Limiting efficiencies of ideal single and multiple energy gap terrestrial solar cells, *J. Appl. Phys., 51* (1980) 4494 - 4500.

2 M. S. Lundstrom and R. J. Schuelke, Numerical analysis of heterostructure devices, *IEEE Trans. Electron Devices, 30* (1983) 1151 - 1159.

3 J. L. Gray and R. J. Schwartz, Two-dimensional computer simulation of single crystal silicon concentrator cells, *Proc. 17th IEEE Photovoltaic Specialists' Conf., Kissimmee, FL, 1984*, IEEE, New York, 1984, pp. 1297 - 1302.

4 R. D. Nasby, C. M. Garner, F. W. Sexton, J. L. Rodriguez, B. H. Rose and H. T. Weaver, High efficiency p^+–n–n^+ silicon concentrator solar cells, *Sol. Cells, 6* (1982) 49 - 58.

5 R. A. Sinton, Y. Kwark, J. Y. Gan and R. M. Swanson, 27.5-Percent efficient silicon concentrator solar cells, *IEEE Electron Dev. Lett.*, 7 (1986) 567 - 569.

6 J. W. Slotboom and H. C. de Graaff, Measurements of bandgap narrowing in Si bipolar transistors, *Solid-State Electron., 19* (1976) 857 - 862.

7 S. P. Tobin, C. Bajgar, S. M. Vernon, L. M. Goeffroy, C. J. Keavney, M. M. Sanfacon, V. E. Haven, M. B. Spitzer and K. A. Emery, A 23.7 percent efficient one-sun GaAs solar cell, *Proc. 19th IEEE Photovoltaic Specialists' Conf., New Orleans, LA, May 4 - 8, 1987*, IEEE, New York, 1987, pp. 1492, 1493.

8 H. C. Hamaker, C. W. Ford, J. G. Werthen, G. F. Virshup, N. R. Kaminar, D. L. King and J. M. Gee, 25% Efficient magnesium-doped AlGaAs/GaAs solar concentrator cells, *Appl. Phys. Lett.*, *47* (1985) 762 - 764.

9 M. S. Lundstrom, M. R. Melloch, R. F. Pierret, P. D. DeMoulin, D. P. Rancour, C. S. Kyono and M. S. Carpenter, Basic studies of III–V high-efficiency cell components, *Technical Report TR-EE 87-33*, School of Electrical Engineering, Purdue University, West Lafayette, IN, September, 1987.

10 S. P. Tobin, Spire Corporation, private communication.

11 P. D. DeMoulin, M. S. Lundstrom and R. J. Schwartz, GaAs concentrator cells: design options and constraints, *Proc. 18th IEEE Photovoltaic Specialists' Conf., Las Vegas, NV, 1985*, IEEE, New York, 1985, pp. 321 - 326.

12 R. P. Gale, John C. C. Fan, G. W. Turner and R. L. Chapman, *Proc. 17th IEEE Photovoltaic Specialists' Conf., Kissimmee, FL, 1984*, IEEE, New York, 1984, p. 1422.

13 R. Hulstrom, R. Bird and C. Riordan, Spectral solar irradiance data sets for selected terrestrial conditions, *Sol. Cells, 15* (1985) 365 - 391.

14 C. J. Hwang, *J. Appl. Phys.*, *42* (1971) 4408 - 4413.

15 C. J. Hwang, *Phys. Rev. B, 6* (1972) 1355 - 1359.

16 A. Huag, *J. Phys. C, 16* (1983) 4159 - 4172.

17 H. C. Casey, Jr., and M. B. Panish, *Heterostructure Lasers,* Academic Press, New York, 1978.

18 R. J. Nelson and R. G. Sobers, *J. Appl. Phys.*, *49* (1978) 6103 - 6108.

Effects of heavy impurity doping on electron injection in p^+-n GaAs diodes

M. E. Klausmeier-Brown, M. S. Lundstrom, and M. R. Melloch
School of Electrical Engineering, Purdue University, West Lafayette, Indiana 47907
S. P. Tobin
Spire Corporation, Patriots Park, Bedford, Massachusetts 01730

(Received 11 February 1988; accepted for publication 25 April 1988)

Measurements of electron injection currents in p^+-n diodes are presented for a range of p-type dopant concentrations. A successive etch technique was used to characterize the electron injection current in terms of the product $(n_o D_n)$. Measurements are presented for Zn-doped GaAs solar cells with p-layer hole concentrations in the range $6.3\times10^{17}-1.3\times10^{19}\ \mathrm{cm}^{-3}$. The results demonstrate that so-called band-gap narrowing effects substantially increase the injected electron current in heavily doped p-type GaAs. These heavy doping effects must be accounted for in the modeling and design of GaAs solar cells and heterostructure bipolar transistors.

The efficiency of silicon solar cells and the gain of silicon bipolar transistors are profoundly influenced by changes in the energy-band structure associated with heavy impurity doping.[1] The measurements of Slotboom and DeGraaff showed that heavy doping effects greatly enhance electron injection currents in silicon p^+-n junctions,[2] but corresponding measurements for p^+-n GaAs have not yet been reported. In this letter we characterize electron injection currents in p^+-GaAs doped from 6.3×10^{17} to $1.3\times10^{19}\ \mathrm{cm}^{-3}$. The results show heavy doping effects in p^+-GaAs that are analogous to those observed in p^+-Si and comparable in magnitude. This work demonstrates that heavy doping effects must be treated in order to accurately model GaAs bipolar devices.

The current density versus applied voltage for a forward-biased p-n diode can be represented by

$$J = J_{01}[\exp(qV_A/k_BT) - 1] + J_{02}[\exp(qV_A/2k_BT) - 1], \quad (1)$$

where J_{01} and J_{02} are the saturation current densities associated with carrier recombination in the quasi-neutral and space-charge regions, respectively. All diodes studied in this work were found to be well described by (1). For a diode with a thin, unpassivated p-layer, the saturation current component due to electron injection in the quasi-neutral p-region can be written

$$J_{01e} = \frac{q(n_o D_n)}{W_p} \frac{S}{S + (D_n/W_p)}, \quad (2)$$

where n_o is the equilibrium minority-carrier concentration, D_n is the minority-carrier electron diffusion coefficient, S is the recombination velocity at the surface of the p-type layer, and W_p is the width of the quasi-neutral p-type layer. An effective intrinsic carrier concentration, n_{ie}^2, is often introduced to relate n_o to the ionized dopant density by

$$n_o \equiv n_{ie}^2/p_o, \quad (3)$$

where p_o is the hole concentration in the p-layer. Measurements have shown that n_{ie} in heavily doped silicon substantially exceeds n_{io}, the intrinsic carrier concentration in lightly doped silicon. For device modeling purposes, this effect is often described by relating n_{ie} to n_{io} with a nonphysical, apparent band-gap shrinkage.[1]

In this letter we make use of a recently described successive etch technique to quantify the electron saturation current density, J_{01e}, as a function of the p-layer hole concentration, p_o.[3] The results are reported in terms of the parameter most directly obtained from the measurement, the $(n_o D_n)$ product. Translation of these results into the form of apparent band-gap shrinkage data for use in numerical simulations is briefly discussed.

A cross section of the GaAs solar cells used for these experiments is displayed in Fig. 1. All cells were grown by metalorganic chemical vapor deposition (MOCVD) in a commercial, five-wafer reactor (Spire Corporation model MO-450). Four percent of each cell's top surface was covered by a metal grid pattern which formed an ohmic contact to the p^+-GaAs cap layer. The layer of interest in this study is the Zn-doped, p-type GaAs layer which lies just below the passivating p-$(Al_{0.9}Ga_{0.1})As$ heteroface layer. Five cells, nominally identical except for the p-layer doping density, were studied. Details of the film growth and cell processing have been described by Tobin *et al.*[4]

The cells were first characterized by fitting the mea-

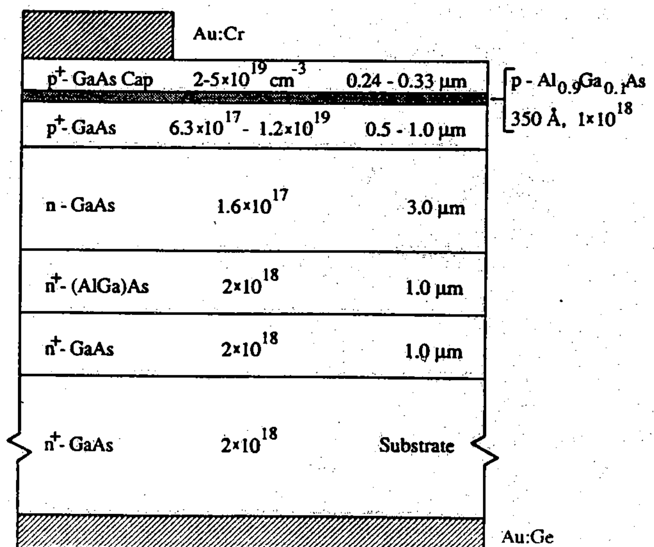

FIG. 1. Cross section of the solar cells used in this study (before etching).

 0003-6951/88/262255-03$01.00 © 1988 American Institute of Physics

sured dark current-voltage (I-V) characteristics to (1). The resulting J_{01} values were independent of the emitter doping density, which suggests that the initial $n = 1$ dark current component was dominated by hole injection into the quasi-neutral n-region. After removing the p-GaAs cap and the p-$(Al_{0.9}Ga_{0.1})As$ heteroface layers by chemical etching, J_{01} was observed to increase. The magnitude of the increase, from a factor of 3 for cells with the most heavily doped emitters to a factor of 22 for cells with the most lightly doped emitters, demonstrates that the $n = 1$ dark current of unpassivated cells was controlled by electron injection into the quasi-neutral p-layer. A successive etch technique was then used to characterize the electron injection current.[3] In brief, the technique consists of successive 20 s etches of the p-layer in a solution of $(2H_2SO_4{:}1H_2O_2{:}96H_2O)$ at 25 °C, followed by measurement of the forward-biased, dark I-V characteristic and extraction of J_{01}. During the etching process, J_{01} was observed to increase as the p-layer was thinned. The electron injection component, J_{01e}, was deduced as a function of emitter thickness, W_p, by subtracting J_{01} of the passivated cell (which was thought to be dominated by hole injection into the n-region) from the value of J_{01} measured after each etch. Because J_{01} was so low in the passivated cells, this subtraction had a minor influence on the value of J_{01e} deduced.

The current associated with electron injection into the quasi-neutral p-layer is described by (2) if the minority-carrier diffusion length exceeds the width of the p-region, W_p (0.5 μm in all but sample No. 3, for which $W_p = 1.0\,\mu$m). From a detailed analysis of the internal quantum efficiency and dark current of similar cells grown in the same reactor with an emitter doping of 2×10^{18} cm^{-3}, an electron diffusion length of $\approx$3–5 μm was deduced.[4] Because all cells used for this study had comparable internal quantum efficiencies and dark currents, we conclude that (2) should accurately describe J_{01e}. Equation (2) may be rearranged to show how the electron injection current varies with etch time t during the experiment:

$$J_{01e}^{-1} = \left(\frac{W_{p0}}{q(n_oD_n)} + \frac{1}{qn_oS}\right) - \left(\frac{R}{q(n_oD_n)}\right)t, \qquad (4)$$

where R is the etch rate. According to (4), a plot of J_{01e}^{-1} versus etch time should be linear; the experimental results confirm this prediction. From the slope of the line, $R/q(n_oD_n)$, the product (n_oD_n) was deduced. The result is independent of the surface recombination velocity, S.

Because the objective of this study was to determine the product, (n_oD_n), as a function of doping density, it was important to thoroughly characterize the doping of the p-ty[pe] layer. First, carrier concentration (from Hall effect m[ea]surements, assuming a Hall factor of unity) was plotted v[er]sus resistivity for a series of p-type GaAs films grown in [the] same MOCVD reactor. For each solar cell used in the pr[es]ent study, the resistivity of the p-layer was measured using [an] adjacent test resistor. The hole concentration p_o was th[en] deduced for each cell from the measured resistivity, us[ing] the previously constructed plot. The results are displayed [in] Table I. Next, Schottky barrier capacitors were formed [by] depositing aluminum on the p-layer of each cell, and [the] quantity $(N_A - N_D)$ was deduced from reverse-biased [ca]pacitance-voltage (C-V) profiling measurements. The [re]sults of the C-V measurements are displayed in Table I. F[in]ally, secondary ion mass spectroscopy (SIMS) confirm[ed] that the p-layer of each sample was uniformly doped. SI[MS] analysis measured the Zn concentration, N_{Zn}. (Howe[ver,] the absolute accuracy of SIMS analysis was deemed to [be] only a factor of 2.)

Results of the measurements for cells with five differ[ent] p-layer dopings are summarized in Table I. The quan[tity] (n_oD_n) was obtained from the slope of J_{01e} versus etch t[ime] according to (4). The temperature during the experime[nt is] also listed in Table I. Following del Alamo, we have sca[led] all (n_oD_n) products to 300 K by using the known temp[era]ture dependence of n_{io}.[5] The maximum error introduce[d by] this temperature scaling should not exceed 4%.

Figure 2 is a plot of (n_oD_n) at 300 K versus dop[ing] density. To highlight the effects of heavy impurity dop[ing,] we also indicate the (n_oD_n) product computed without [con]sidering heavy doping effects (except for degeneracy o[f the] hole gas). The dashed line was evaluated from

$$n_o = \frac{n_{io}^2}{p_o}\,\frac{\mathscr{F}_{1/2}(\eta_c)}{e^{\eta_c}},$$

using the minority-carrier electron mobilities predicte[d by] Walukiewicz *et al.*[6] for uncompensated p-GaAs, [and] $n_{io} = 2.25\times10^{6}$ cm^{-3}.[5] Since measured minority-ca[rrier] electron mobilities in MOCVD-grown GaAs[7] are less [than] those predicted by Walukiewicz *et al.* for uncompens[ated] material, the dashed line in Fig. 2 should be regarded a[s an] upper limit for (n_oD_n) in the absence of heavy dopin[g ef]fects. Comparison of the dashed line with the experim[ental] results shows that a substantial increase in (n_oD_n) ca[n be] associated with heavy doping effects. The increase is a fa[ctor] of 10 at $p_o \approx 10^{19}$ cm^{-3}, and underscores the importan[ce of] correctly modeling these phenomena in order to accur[...]

TABLE I. Summary of the measurements. The product (n_oD_n) is listed both at the measurement temperature T and at 300 K. C-V measurements co[uld not] be obtained for the highest doped sample, No. 5.

Sample	T (°C)	Resistivity (Ω cm)	p_0 (cm^{-3}) (Hall effect)	$N_A - N_D$ (cm^{-3}) (C-V)	N_{Zn} (cm^{-3}) (SIMS)	(n_oD_n) at T (10^{-4} cm^{-1} s^{-1})	(n_oD_n) at 300 (10^{-4}cm^{-1} s^{-1})
1	24.0	0.062	6.3×10^{17}	6×10^{17}	1.1×10^{18}	5.5	10
2	25.0	0.040	1.0×10^{18}	1×10^{18}	1.7×10^{18}	4.5	6.7
3	22.4	0.018	3.0×10^{18}	3×10^{18}	3.0×10^{18}	1.4	3.5
4	23.4	0.014	4.6×10^{18}	5×10^{18}	5.8×10^{18}	1.1	2.3
5	23.3	0.0079	1.3×10^{19}	⋯	1.2×10^{19}	0.70	1.5

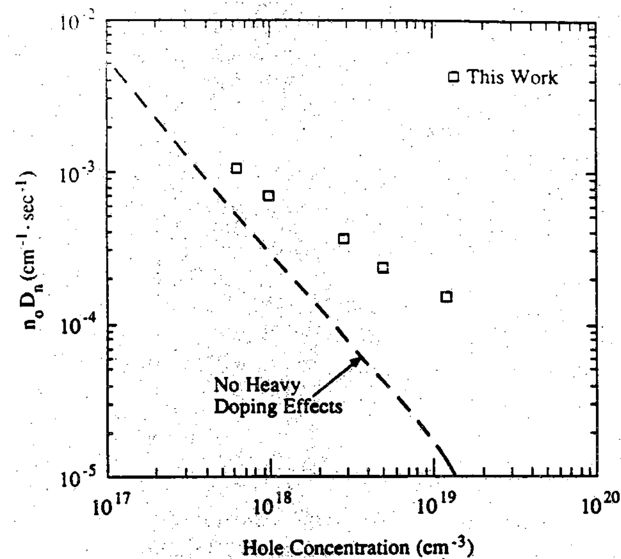

FIG. 2. Measured $(n_o D_n)$ product plotted vs hole concentration p_o at $T = 300$ K. The values of p_o used were those obtained from Hall-effect measurements. The dashed curve was obtained using the theoretical minority electron diffusion coefficient from Ref. 6 with Eq. (5), assuming no compensation.

predict the behavior of GaAs devices that contain heavily doped regions. Note that the behavior of the product $(n_o D_n)$ versus hole concentration is quite similar to that observed in heavily doped silicon (see Fig. 7 of Ref. 1).

A nonphysical, apparent band-gap shrinkage parameter is often introduced for device modeling purposes.[1] The saturation current density for electrons injected across a GaAs p-n junction is modeled by the expression

$$J_{01e}^{\mathrm{mod}} = \frac{q n_{io}^2 D_o}{p_o W_p} \frac{S}{S + (D_n / W_p)} \exp\left(\frac{\Delta E_g^{\mathrm{app}}}{k_B T}\right), \qquad (6)$$

where n_{io} is the intrinsic carrier concentration assumed in the device model, D_o is the assumed electron diffusion coefficient in p-GaAs for a hole concentration p_o, and $\Delta E_g^{\mathrm{app}}$ is the nonphysical apparent band-gap shrinkage. Equating (6) to (2) we find

$$\Delta E_g^{\mathrm{app}} \equiv k_B T \ln[(n_o D_n) p_o / n_{io}^2 D_o], \qquad (7)$$

where $(n_o D_n)$ is the measured product of the equilibrium electron concentration and the electron diffusion coefficient on the p-side. Use of this definition of $\Delta E_g^{\mathrm{app}}$ ensures that the modeled electron injection saturation current density, J_{01e}^{mod}, will be equal to the measured J_{01e}. Equation (7) is the definition of apparent band-gap shrinkage implicitly assumed by Slotboom and DeGraaff[2] in their pioneering studies of heavy doping effects in p^+-Si. We do not quote apparent band-gap shrinkage values, because they depend on D_o, the assumed minority-carrier electron diffusion coefficient, which is not well known at present.

Measurements of electron current in p^+-n GaAs diodes were presented and analyzed. The large magnitude of the measured currents in cells doped greater than 10^{18} cm^{-3} on the p-side was attributed to heavy doping effects in the p^+-GaAs. These effects are analogous to so-called band-gap narrowing effects in silicon and were found to be comparable in magnitude to those observed in p^+-Si. To accurately model GaAs devices such as solar cells and bipolar transistors, heavy doping effects must be treated. Further work is needed to extend the measurements over a wider range of doping densities and dopant types, to separate out the effects of heavy doping on the minority-carrier diffusion coefficient, and to explore heavy doping effects in n-GaAs.

The authors wish to thank Stanley Vernon of Spire Corporation for providing the MOCVD films used for this work. This work was supported by the Solar Energy Research Institute, subcontract XL-5-05018-1. M. E. Klausmeier-Brown was supported by the Eastman–Kodak Corporation.

[1]J. A. del Alamo and R. M. Swanson, Solid-State Electron. 30, 1127 (1987).
[2]J. W. Slotboom and H. C. DeGraaff, Solid-State Electron. 19, 857 (1976).
[3]M. E. Klausmeier-Brown, C. S. Kyono, P. D. DeMoulin, S. P. Tobin, M. S. Lundstrom, and M. R. Melloch, IEEE Trans. Electron Devices (in press).
[4]S. P. Tobin, S. M. Vernon, C. Bajgar, L. M. Geoffroy, C. J. Keavney, M. M. Sanfacon, and V. E. Haven, Solar Cells (in press).
[5]J. S. Blakemore, J. Appl. Phys. 53, R123 (1982).
[6]W. Walukiewicz, J. Lagowski, L. Jastrzebski, and H. C. Gatos, J. Appl. Phys. 50, 5040 (1979).
[7]R. K. Ahrenkiel, D. L. Dunlavy, D. Greenberg, J. Schlupmann, H. C. Hamaker, and H. F. MacMillan, Appl. Phys. Lett. 51, 776 (1987).

Effects of Na_2S and $(NH_4)_2S$ edge passivation treatments on the dark current-voltage characteristics of GaAs *pn* diodes

M. S. Carpenter, M. R. Melloch, and M. S. Lundstrom
Purdue University, School of Electrical Engineering, West Lafayette, Indiana 47907

S. P. Tobin
Spire Corporation, Patriots Park, Bedford, Massachusetts 01730

(Received 12 February 1988; accepted for publication 22 April 1988)

We have investigated the dark current-voltage characteristics of GaAs *pn* homojunctions whose surfaces have been passivated with Na_2S and $(NH_4)_2S$ chemical treatments. Reductions in $2kT$ perimeter recombination currents by a factor of 3.2 were obtained for the two treatments. A shunt leakage, observed at low forward bias for the Na_2S treated devices, is virtually eliminated with the $(NH_4)_2S$ treatment. It is also shown that even the high quality, large area ($0.25\ cm^2$) *pn* diodes used in this study are dominated by $2kT$ edge currents before passivation.

Due to a large density of surface states the performance of GaAs devices, such as solar cells and heterojunction bipolar transistors (HBT's), can be dominated by recombination at exposed mesa edges. This recombination at the exposed perimeter gives rise to an additional component of forward biased current for a GaAs *pn* diode. The total current in a forward-biased GaAs *pn* junction can be represented as

$$I = J_{01}A\,[e^{qv/kT} - 1] + (J_{02B}A + J_{02P}P)\,[e^{qv/2kT} - 1]. \quad (1)$$

The saturation current densities J_{01} and J_{02B} are associated with carrier recombination in the quasi-neutral and bulk space-charge regions, respectively, and A is the area of the *pn* junction. The current density J_{02P} is associated with recombination at the exposed mesa edge and P is the perimeter of the *pn* junction. Even for the large square ($A = 0.25\text{cm}^2$) GaAs diodes reported in this letter, the total perimeter recombination current is much larger than the bulk space-charge recombination current.[1]

The elimination or lowering of surface recombination can therefore significantly reduce the $2kT$ current of a GaAs diode. This reduction in $2kT$ current would result in an increase in gain at a given collector current for a HBT. Lowering of the dark current due to reduction in $2kT$ current of a solar cell will increase the one-sun fill factor and hence increase the efficiency of the cell.[1] The lowering of the $2kT$ perimeter recombination current in *pn* GaAs diodes also allows one to observe the $2kT$ bulk recombination current; thereby studies could be performed to correlate bulk $2kT$ recombination current with defects and impurities, and the possibility of further reduction in $2kT$ current. A reduction in perimeter surface states may also reduce edge generation and increase the storage time of dynamic GaAs memories.[2,3]

Recently, photochemical[4] and chemical[5–8] treatments have been shown to be effective in lowering the surface state density of III-V semiconductors. This reduction of the surface state density unpins the Fermi level at the surface and also reduces the nonradiative recombination at the surface.[6] However, these treatments are far from ideal. They last for only a short time in room air (anywhere from 20 min for the photochemical treatment to 18–48 h for a Na_2S chemical treatment). Another problem with the Na_2S chemical treatment is the introduction of a surface conduction. For a GaAs solar cell or emitter base junction of a HBT, the surface conduction is manifested as a shunt leakage at low forward bias.

While the nature of the semiconductor surface after treatment is not known, it appears that the common link between various chemical treatments is sulfur-containing compounds. The most widely reported compound is Na_2S. It is not known if the other elements of the various sulfide compounds contribute to the nature of the interface or just provide a vehicle to present sulfur to the surface of the semiconductor. Nottenburg *et al.*[8] have investigated the effects of the Na_2S treatment on the dark current-voltage (*I-V*) characteristics of AlGaAs/GaAs *pn* heterojunctions. In this letter we report the effects of Na_2S and $(NH_4)_2S$ treatments on the dark *I-V* characteristics of GaAs *pn* homojunctions.

The diodes used in this study were grown by metalorganic chemical vapor deposition (MOCVD) in a commercial five-wafer reactor. The same reactor and growth procedure has recently produced *p/n* heteroface solar cells which have the highest reported AM1.5 efficiency, indicating very high film quality.[9] The device structure and relevant device parameters are shown in Fig. 1. After film growth, metal

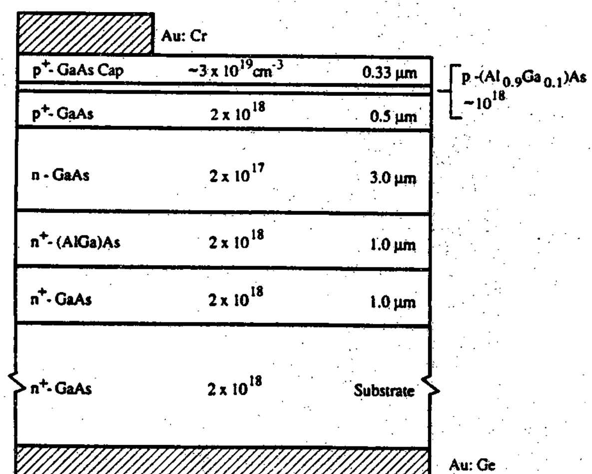

FIG. 1. Cross section of the GaAs diodes used in this study.

 0003-6951/88/252157-03$01.00 © 1988 American Institute of Physics

patterns were defined using image reversal photolithography and lift-off. Then conventional photolithography and wet chemical etching were used to define mesas. Two size devices were fabricated, one a 0.5 cm on a side square and the second a 0.5 cm by 310 μm rectangle.

The chemical treatments started by etching the devices for 10 s in 1:1:500 H_2SO_4:H_2O_2:H_2O, followed by a rinse in de-ionized water. The Na_2S treatment then consisted of soaking the wafer in a 1 M solution of the sulfide. The device was allowed to soak for up to 10 min to allow for chemical reaction. The devices were then spun dry at 5000 rpm for 60 s, which left a thin polycrystalline film of $Na_2S \cdot 9H_2O$ over the surface of the wafer. If insufficient time (approximately 7 min or less) was allowed for the chemical to react, no surface passivation took place and no reduction of edge currents was observed. Such devices, however, exhibited a hysteresis in their *I-V* characteristics indicating a charge trapping at the improperly treated surface.

The $(NH_4)_2S$ treatment consisted of making a saturated solution of $(NH_4)_2S$ from H_2S and electronic grade NH_4OH. After etching the sample for 10 s in the 1:1:500 H_2SO_4:H_2O_2:H_2O solution, the wafer was rinsed in de-ionized water and soaked in the $(NH_4)_2S$ solution for up to 5 min. The wafer was then rinsed with de-ionized water and blown dry with N_2. This treatment left no visible film on the wafer.

Displayed in Fig. 2 is a typical diode *I-V* characteristic before treatment and after the above described Na_2S and $(NH_4)_2S$ chemical treatments. The Na_2S treatment was removed by rinsing in de-ionized water[5] before performing the $(NH_4)_2S$ chemical treatment. [*I-V* characteristics similar to those shown in Fig. 2 were obtained when the order of the Na_2S and $(NH_4)_2S$ chemical treatments was reversed. The $(NH_4)_2S$ treatment can be removed by spinning on AZ1350J photoresist and then rinsing off the photoresist with acetone.] As is readily visible, the device initially exhibited no kT diffusion current but only a $2kT$ recombination current (series resistance effects are observed at high bias). After the Na_2S treatment, the device exhibits lower $2kT$ recombination current and a shunt leakage at low forward bias. As also seen in Fig. 2, after the $(NH_4)_2S$ treatment the device exhibited a slightly better reduction in the $2kT$ recombination current than after the Na_2S treatment. In addition, after the $(NH_4)_2S$ treatment the device has one order of magnitude less shunt leakage at low forward bias than after the Na_2S treatment.

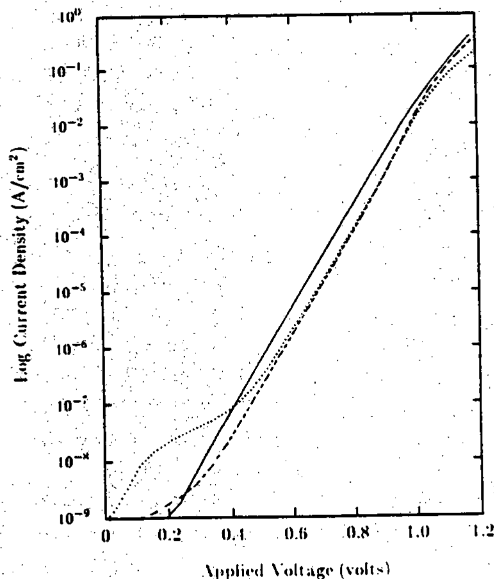

FIG. 2. Typical current-voltage characteristics for 1.55×10^{-2} cm² devices. The solid line is the initial untreated device, the dotted line is after Na_2S treatments, and the dashed line is after removal of the Na_2S and subsequent $(NH_4)_2S$ treatment. The *I-V* curves were all measured at 22.2 °C.

We have also observed a much slower aging of our $(NH_4)_2S$ treated devices than our Na_2S treated devices. The cause of the aging of the Na_2S treatment is probably the humidity of the room air since the Na_2S treatment can be removed by rinsing with de-ionized water.[5] Since the $(NH_4)_2S$ passivation persists after the de-ionized water rinse, it is not surprising that the $(NH_4)_2S$ treatment is less reactive with room air.

The expression for the pre-exponential factor for the recombination current is

$$I_{02} = AJ_{02B} + PJ_{02P}, \qquad (2)$$

where A and P are the area and perimeter of the device, respectively. Since I_{02} is the measured current, it will contain a bulk component and perimeter component. To quantify the reduction in the surface component, the bulk component must be known. However, to investigate extreme cases where surface or bulk currents are dominating, one needs only to examine the scaling of the current. If the devices are bulk dominated, the ratio of currents for two different size devices will be equal to the ratio of their areas. If the devices are surface dominated, then the ratio of their currents will be equal to the ratio of their perimeters.

The average observed initial I_{02} for our large area devices was 1.76 pA and for our small area devices was 0.93 pA. The ratio of these currents is 1.89. A comparison of thi to the ratio of the perimeters (1.88) and areas (16) indicate that the devices are perimeter dominated. Since the initia $2kT$ current is all perimeter current, the perimeter recom bination current density is $J_{02P} = 8.80\times10^{-13}$ A/cm. Fo the treated devices, the average values of I_{02} were 1.02 an 0.325 pA for the large and small area devices, respectively This gives a ratio of 3.14 for the currents, indicating that th devices are neither perimeter nor bulk dominated. Howeve the surface component has been reduced to a value compa able with the bulk component. We have used Eq. (2) t estimate the $2kT$ recombination current densities after th chemical treatments obtaining $J_{02B} = 1.85\times10^{-12}$ A/cm and $J_{02P} = 2.79\times10^{-13}$ A/cm. The treatments therefo produced a reduction by a factor of 3.2 in perimeter curren

In conclusion, we have investigated the effects of Na_2 and $(NH_4)_2S$ chemical passivation on the dark *I-V* chara teristics of GaAs *pn* homojunction diodes. Comparable r duction in $2kT$ edge recombination current by a factor of 3. was observed for Na_2S and $(NH_4)_2S$ chemically passivate diodes. The shunt leakage observed at low forward biases f Na_2S treated diodes was virtually eliminated with t $(NH_4)_2S$ surface passivation. We have also demonstrat that even for large area *pn* GaAs homojunction diod

($A = 0.25$ cm^2), the recombination current is due to edge effects in high quality material.

The authors wish to thank Dr. Eli Yablonovitch for discussions concerning the Na_2S passivation technique and S. M. Vernon for MOCVD growth of the films used in this study. This work was supported by the Solar Energy Research Institute under subcontract XL-5-05018-1 and the Office of Naval Research under grant N00014-86-K0350.

[1]S. P. Tobin, S. M. Vernon, C. Bajgar, L. M. Geoffroy, C. J. Keavney, M. M. Sanfacon, and V. E. Haven, Solar Cells (in press).
[2]T. E. Dungan, J. A. Cooper, Jr., and M. R. Melloch, IEEE Electron Device Lett. EDL-8, 243 (1987).
[3]T. E. Dungan, J. A. Cooper, Jr., and M. R. Melloch, 1987 International Electron Devices Meeting Technical Digest, p. 348.
[4]S. D. Offsey, J. M. Woodall, A. C. Warren, P. D. Kirchner, T. I. Chappell, and G. D. Pettit, Appl. Phys. Lett. 48, 475 (1986).
[5]C. J. Sandroff, R. N. Nottenburg, J. C. Bischoff, and R. Bhat, Appl. Phys. Lett. 51, 33 (1987).
[6]E. Yablonovitch, C. J. Sandroff, R. Bhat, and T. J. Gmitter, Appl. Phys. Lett. 51, 493 (1987).
[7]B. J. Skromme, C. J. Sandroff, E. Yablonovitch, and T. J. Gmitter, Appl. Phys. Lett. 51, 2022 (1987).
[8]R. N. Nottenburg, C. J. Sandroff, D. A. Humphrey, T. H. Hollenbeck, and R. Bhat, Appl. Phys. Lett 52, 218 (1988).
[9]S. P. Tobin, C. Bajgar, S. M. Vernon, L. M. Geoffroy, C. J. Keavney, M. M. Spitzer, and K. A. Emery, *Conference Record, 19th IEEE Photovoltaic Specialists Conference* (IEEE, New York, 1987), p. 1492.